Ultracold matter systems and atomtronics instrumentation.

by

Evan Ali Salim

B.A., Ithaca College, 2003

A thesis submitted to the
Faculty of the Graduate School of the
University of Colorado in partial fulfillment
of the requirements for the degree of
Doctor of Philosophy
Department of Physics
2011

This thesis entitled:
Ultracold matter systems and atomtronics instrumentation.
written by Evan Ali Salim
has been approved for the Department of Physics

Dana Anderson

James Thompson

Date ____________________

The final copy of this thesis has been examined by the signatories, and we find that both the content and the form meet acceptable presentation standards of scholarly work in the above mentioned discipline.

Salim, Evan Ali (Ph.D., Physics)

Ultracold matter systems and atomtronics instrumentation.

Thesis directed by Professor Dana Anderson

Ultracold matter has tremendous potential for applications in the fields of quantum computing, atomic clocks, precision magnetometery, and inertial navigation. In order for these applications to be successfully realized it is necessary to develop both a high level understanding of the underlying physics and instrumentation to enable the execution of the devices. The instrumentation aspect falls into two categories: the physical apparatus and the tools and techniques for implementing the devices.

This dissertation describes the technical and scientific development of instrumentation for ultracold atoms. We first present our work on compact apparatus for atom-chip based BEC production with particular emphasis on vacuum chambers and opto-mechanical systems for portable applications. We present the development of atom chip technology, both generally and specifically pertaining to the emerging field of atomtronics. Finally we present the implementation and preliminary experiments of an apparatus made for experiments with the ultimate goal of demonstrating an atom transistor.

Dedication

To my parents, Gay and Mohammad Salim, who never told me “no.”

Acknowledgements

The completion of this thesis would not have been possible without the help from a lot of people along the way.

My thesis advisor, Dana Anderson has been a wonderful mentor. I cannot thank Dana enough for all of the wisdom, guidance, opportunities, and trust he has given me in my years at JILA. I am deeply grateful to have worked with so many talented and wonderful people all of these years in the trenches. Their accomplishments are far too great and too many to mention here, but without them I'm sure I would never have gotten all of this work done. Thanks to the graduate students I have worked with: Stephen Segal, Matthew Squires, Kai Hudek, Daniel Farkas, Seth Caliga, Jonathan Pfeiffer, Rick Chaung, Simon Braun, Tommi Hakala, Allison Churnside, Paul Kunz, Ricardo Jiminez, Benjamin Luey, Brian McCarthy, and Shengwag Du. And thanks to the undergraduates: Markia Meertins, Farhad Madjetemouri, William Holmgren, Andrew Holmgren, and Carl Wiedeman. Leslie Czaia has helped me more than I can say, but through her I have learned the value of people with good hands. Thanks to Alex Zozulya for all of his help with theory over the years.

I have relied heavily on the talents of the members of the JILA machine and electronics shops. I have been to as the electronics shop for help with painfully simple problems more times than I care to admit. Thank you to Carl Sauer, Paul Beckingham, Terry Brown, James Fung-A-Fat, and David Tegart, and Michael Whitmore. The members of the machine shop, Blaine Horner, Kim Hagen, Ariel Paul, Todd Asnicar, Tom Foote, David Alchenberger, Tracy Keep and Hans Green have been instrumental to the apparatus development in this thesis, and I admire all of them for

their consistently high quality work and creative solutions to hard fabrication problems. I owe special thanks to Tracy Keep for machining the physics package; and extra thanks and apologies to Todd Asnicar, who has tirelessly fabricated the strange and horrible glass parts that I designed with seemingly utter disregard to his mental health.

Thanks to all of our collaborators: Sterling McBride, Joey Michalchuk, and Stephen Lipp at Sarnoff corporation, who taught me about anodic bonding and helped us to make channel cells; Robert Mihaliovoch and Jeffery DeNatale at Teledyne Scientific and Imaging who made our atom chips.

I am also extremely grateful to all of the people who helped be on my way to the graduate program. Thanks to the faculty at Ithaca College: Bruce Thompson, John Schwartz, Beth Ellen Joseph Clark, Daniel Briotta, Charles Spenser and Peter Seligman for giving me such a solid foundation in physics. Thanks to all the people who taught me how to machine and who taught me the value of good craftsmanship: Bill Hollander and the team at HPD, and Tracy Buxkemper and Charles Bowen in the CU physics shop. Thanks to Dr. John Sweetenham and the oncology team at University of Colorado Health Sciences Center, without whom I would not have made it this long.

Finally, and most importantly, thanks to my family and all of my friends who have tolerated and even supported me over the last seven years.

Contents

Chapter

Figures

Figure

Chapter 1

Introduction

Since the first demonstrations of Bose-Einstein condensation in 1995 [1, 2, 3] ultra cold matter has become a fertile and lively field of study. Recent years have shown a growing interest in the use of ultra-cold atoms in venues that reach far beyond basic atomic physics. Neutral atoms in periodic potentials have been used to mimic condensed matter systems and achieve previously unobtainable regimes such as Mott insulator states [4], which in turn allows for unrivaled tests of the Bose-Hubbard Hamiltonian. Significant work has also been done towards using cold and ultra-cold atoms for quantum computers [5, 6, 7], more accurate atomic clocks[8, 9, 10], and precision magnetometery [11, 12]. One application of particular interest to our group is that of inertial sensing for gyroscopy, accelerometry, and gravity gradiometry. The current state of the art instruments in the field of inertial sensing are optical interferometers that employ the Sagnac effect to measure rotation. While these devices are extremely well developed technology even the very best devices are inadequate for purely inertial navigation [13]. Atoms are an attractive alternative to optical devices, because they can offer a dramatic improvement in gyroscope sensitivity. Two identical gyroscopes, one using atoms and the other using light, would have a phase shift sensitivity difference of

$$\frac{\Delta\phi_{atoms}}{\Delta\phi_{light}} = \frac{\lambda M c}{h} \sim 10^{10}. \tag{1.1}$$

Quite the motivation for such a device!

In order for these applications to be successfully realized it is necessary to develop both a high level understanding of the underlying physics and instrumentation to enable the execution of the devices. The instrumentation aspect falls into two categories: the physical apparatus and the tools and techniques for implementing devices.

The need for apparatus development is clear. The world's most precise gyroscope is not useful if it occupies an entire room, draws many kilowatts of power, takes several minutes to produce a single data point, and requires two full time graduate students to operate. In order for cold and ultracold atoms to be competitive with other technologies for applications in and out of the laboratory they must be practical to use. The systems must be compact, low power, and reliable. Also, as all existing methods of producing ultracold atomic samples are pulsed in operation, the systems must have high duty cycle.

Equally important to instrumentation development is building a repertoire of techniques for working with atoms. Ultimately we need a tool box of methods that can drawn from to build devices. One commonly mentioned approach to building this toolbox is "atom optics", where the tools of optics such as mirrors, beam splitters, lenses and waveguides may be used as the building blocks of more complex instruments. An alternate paradigm is a system where where the basic elements of the atomic circuitry may be analogous to electronic components such as resistors, diodes, and transistors. This emerging field has been dubbed "atomtronics."

1.1 Ultracold matter systems

With the notable exceptions of the tremendous work done by the group of Mark Kasevitch at Stanford University to demonstrate portable cold atom gyroscopes and gravity gradiometers [14, 15], and a large European collaboration that has developed a compact atom chip based BEC system used to produce BEC in a drop tower to simulate the effects of BEC in zero gravity [16], there has been relatively little effort towards integration and miniaturization of cold atom systems. The machines that produce samples of cold and ultracold matter are carefully tuned orchestrations of vacuum, lasers, optics, electronics and computers. Most experiments are large, complicated, delicate, and unreliable by any reasonable industrial standard. A central focus of our work in the past few years has been development of these subsystems, with particular emphasis on opto-mechanics, vacuum systems and atom chips.

Atom chips [17, 18, 19, 20, 21] are the key component of our BEC systems. They enable magnetic trapping and manipulation of atoms with only a few Amperes of current. This is in dramatic contrast to conventional machines where the magnetic trapping fields are generated with macroscopic conductors that carry hundreds of Amperes. Lowering the power requirements can dramatically decrease the overall size and complexity of the apparatus, and because of the proximity of the atoms to the current carrying conductors atom chips make it possible to generate very high field gradients. This high level of control of the magnetic field allows for very fast evaporative cooling [22, 23], and enables the production of very fine featured potentials. In addition to improving the system bandwidth the fast evaporation relaxes the requirements of the vacuum system, making it possible for the chambers to be substantially more compact.

To that end we have developed vacuum chambers with integrated atom chips. The principle goal of the system design was to streamline the BEC production process and to allow the focus of the system to be experiments on the atom chip. The compact size would make it possible to integrate the cell into a system that was compact and portable, and would also allow for greater flexibility of the systems. A good analogy of what we wanted to accomplish is the electronic vacuum tube: the form factor of the chamber remains the same making chambers interchangeable. To perform new and different experiments atom chips are exchanged by switching out the entire vacuum chamber. One of the chambers we have developed is shown in Fig. 1.1.

The cells are prepared off-line and when they are needed go into a receiver. The receiver is analogous to the socket for the vacuum tube, and is the remainder of the BEC apparatus. Each receiver is built to satisfy the needs of the intended experiments, but the basic architecture, shown in Fig. 1.2, remans the same. The vacuum cell is mounted in an optics package, which is connected to a laser and electrical systems, which are controlled by a computer. The system outputs data back to the computer, typically in the form of an image.

We have built three systems based on this model: one for gyroscope experiments, which is described in Stephen Segal's doctoral thesis [24], one for a portable BEC system, and one for

Figure 1.1: (Color). The standard atom chip BEC cell developed in our lab.

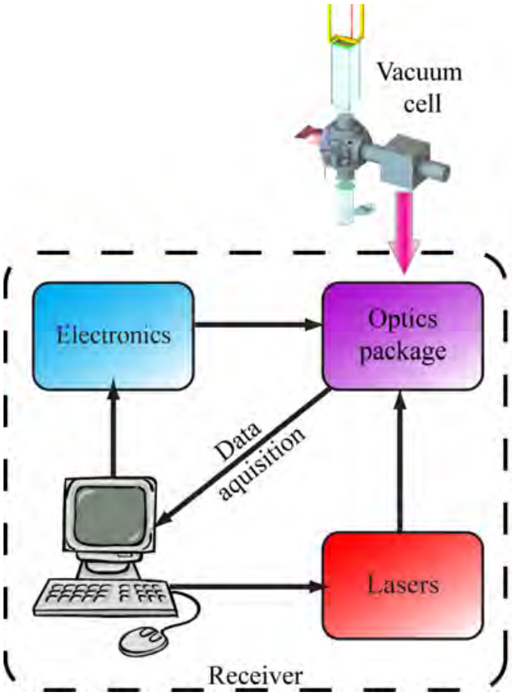

Figure 1.2: (Color). BEC receiver block diagram showing the main components of the BEC system.

experiments on atomtronics. The latter two will be discussed in this thesis.

1.2 Atomtronics

A fair amount of theoretical work has already been done to describe atomtronic devices. The group of Murray Holland at JILA has studied atomtronic systems in the context of optical lattice potentials, both in the case of systems that simulate semiconductor devices directly[25], and in systems meant to mimic the behavior of solid state devices such as diodes or transistors[26]. Peter Zoller's group has proposed a single atom transistor that would act as a gate in optical lattices[27]. The group of Alex Zozulya at Worchester Polytechnic Institute has studied a transistor that consists of a simple three well system[28]. We are pursuing the three well transistor, as we feel that it is the most straightforward to implement experimentally. To the best of our knowledge we are the only experimental group working to realize atomtronic devices.

The function of the transistor is conceptually quite simple: a strong flux of particles is controlled with a weak flux of the same particle. In the case of electronic transistors the particle in question is electrons, but the particle could be neutral atoms. The approach described by [28] is as follows: A cloud of coherent (BEC) atoms are loaded in a triple well potential, such as the potential drawn in figure 1.3. Keeping with the analogy of the transistor, the wells will be referred to as the source, gate and drain. Those wells serve the roles of the like-named parts of a field effect transistor (FET), which is arguably the closest electronic counterpart. The potential is designed so that when the number of atoms in the source is large, and the drain is empty, that the two wells have equal chemical potentials ($\mu_{source} = \mu_{drain}$). The gate well, which separates the source and drain, is made so that when empty ($N_{gate} = 0$) its chemical potential is mismatched to that of the source and drain ($\mu_{gate} < \mu_{source/drain}$). This is shown in figure 1.3a, where the blue lines represent the chemical potentials. This energy mismatch will inhibit tunneling, causing the device to do nothing. By making the gate well very tight, its chemical potential becomes very sensitive to small changes in N_{gate}. By adding a relatively small number of atoms the chemical potential is quickly increased, and when $\mu_{source} \approx \mu_{gate} \approx \mu_{drain}$, atoms will be able to tunnel from the source to the drain through the gate, achieving transistor-like behavior. Differential gain is achieved in this system because the number of atoms that flow from the source to the drain can be substantially more than the change of atom number in the gate needed to enable tunneling. The details of the three well transistor will be discussed in greater depth in chapter 2.

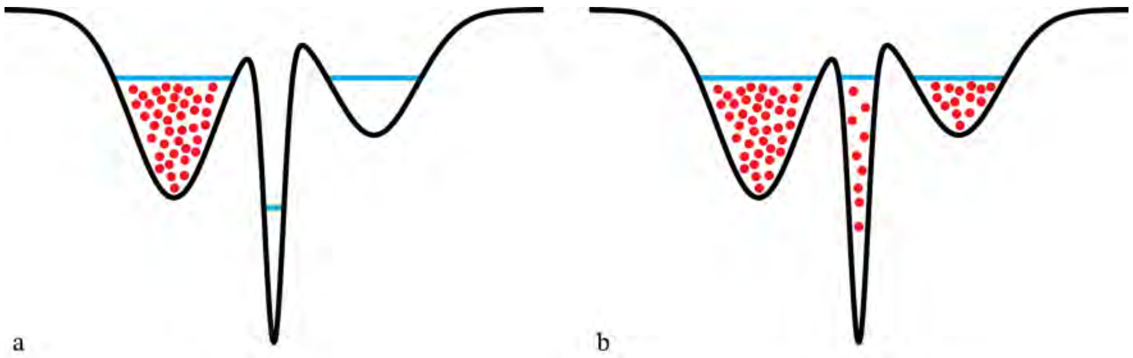

Figure 1.3: (Color). Schematic of the atom transistor described by [28]. (a) The transistor in the "off" state. Here atoms are energetically allowed to tunnel to the far right well, but do not because the middle well blocks tunneling. (b) The transistor in the "on" state. Adding atoms to the middle well brings the chemical potential of the three wells into resonance, allowing atoms to tunnel across from the first to the third well.

One could claim that the distinction between atomtronics and atom optics is merely a semantic one, but there is a fundamental difference between the two. All of the atom optical components to date are based on the interaction of the atoms with externally applied fields: Atom mirrors are made by reflecting clouds of atoms with, for example, pulses of light [29] or magnetic fields[30, 31]. Beamsplitters are made mechanically [32], optically [33], or by spatially separating the atoms with a changing trapping potential [34, 35, 36]. Atomtronic devices, on the other hand, rely on the interaction of the atoms with other atoms to function. In addition to being a building block for more complicated atomic systems, atomtronic devices may be interesting from a perspective of fundamental physics. Unlike the electronic system, phase coherence between the particle fluxes is required for a cold atom transistor to function, which could pave the way to study coherent circuits.

1.3 Dissertation outline

This dissertation will outline the development of compact systems for BEC production in our lab and the application of those system to research on atomtronics. The thesis will proceed as follows: Chapter 2 reviews some of the theory needed to understand ultracold atoms, atom chips, quantum tunneling and the atom transistor. Chapter 3 describes the development of compact vacuum chambers for on-chip BEC and our work to build a portable BEC system. Chapters 4 and 5 are detailed discussions of the atom chip development that has been done in our lab over the past seven years. Chapter 4 focuses on basic atom chip design and fabrication, while chapter 5 focuses on the development of atom chips specifically for atomtronics. Chapter 6 outlines the design and construction of the tabletop apparatus for the atom transistor. Chapter 7 describes the experiments performed with the apparatus described in chapter 6 and presents the results of our first steps towards the experimental realization of an atom transistor.

Chapter 2

Background Theory

This chapter will outline the fundamental theory needed to understand the work described in this thesis. We will start with trapping techniques for neutral atoms and general discussion of Bose-Einstein Condensates. After that we will discuss tunneling in atomic systems, and review some of the relevant work in the field. Finally, we will present the theory of the three well atom transistor. This chapter is not intended to be a thorough discussion of the vast subjects presented, but rather an overview of the theoretical background needed to understand the instruments we have developed. There are many resources for the interested reader to further explore all of the topics discussed here, and reference to those will be noted where appropriate.

2.1 Trapping of neutral atoms

The theoretical background and experimental techniques needed to understand the process in producing BEC are described in detail in many theses and review articles [37, 38, 39, 40]. For the work in this thesis, however, it will be helpful to review the specifics of magnetic and optical trapping of neutral atoms.

2.1.1 Magnetic trapping

In all of the chip based experiments we have performed in our lab the primary method of trapping atoms is with magnetic fields. Magnetic traps exploit the Zeeman shift in atoms with finite magnetic dipole moments to confine atoms in conservative potentials. Suppose that an atom is placed in a magnetic field **B**. Provided that the atom has a non-zero magnetic dipole moment the atom will have an energy shift due to the Zeeman effect given by

$$U = -\mu \cdot \mathbf{B} = -g_f m_f \mu_B \mathbf{B}, \tag{2.1}$$

where m_f is the z component of the total atomic angular momentum for the sate the atom is in, g_f is the Landé-g factor for that state, and μ_B is the Bohr magneton. If the atom is in a weak field seeking state ($g_f m_f > 0$) it can be trapped at the minimum of the magnetic field. To hold atoms the trap must be tight enough to overcome gravity, namely

$$\mu B' > mg, \tag{2.2}$$

and the trap must be deep enough for the hot atoms to not pour out over the top. To confine laser cooled atoms magnetic traps are generally designed to have a minimum field gradient of $30G/cm$ in the direction opposing gravity and depths of $\sim 0.1 - 1mK$.

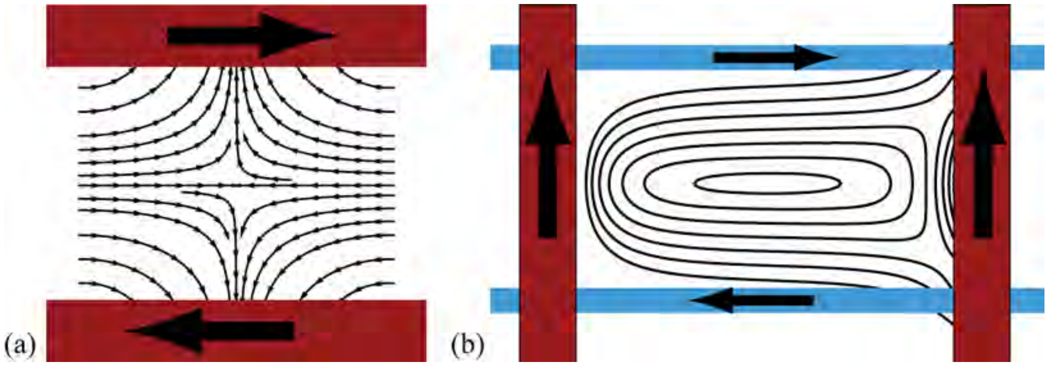

Figure 2.1: (Color). Conventional magnetic traps for neutral atoms. (a) The coil configuration and magnetic for a linear quadrupole trap. Coils, shown in red, are a side views of a square or circular coil carrying current in the directions indicated. This configuration is typically referred to as anti-helmholtz. (b). Configuration of a Ioffe-Pritchard, or harmonic, trap. The blue currents represent the edge of four Ioffe bars used to generate a two dimensional quadrupole trap, and the red currents generate a bias field that adds constructively in such a way that there is a non-zero minimum of the magnetic field in the center of the assembly.

Fields for trapping atoms are generated with either permanent magnets or with currents flowing through wires. The simplest trap one can make is a linear quadrupole trap, which can be formed with either two opposing permanent magnets or by a pair of coils in an anti-Helmholtz configuration, as shown in figure 2.1(a). In BEC experiments, however, one must employ a trap which is at least harmonic in nature, as cold atoms crossing through a field zero are subject to Majorana spin flip transitions and will fall out of the trap. A harmonic magnetic trap is commonly referred to as a Ioffe-Pritchard (IP) trap. A possible coil configuration for such a trap is shown in fig. 2.1(b), where the horizontal blue bars represent two of four currents that generate a two dimensional quadrupole field, and the red bars represent a pair of coils in an elongated Helmholtz configuration. Harmonic traps are characterized by their trap frequencies, which are given in general as

$$\omega = \sqrt{\frac{\mu B''}{m}}, \tag{2.3}$$

where B'' is the second spatial derivative of the magnetic field along the trap axis of interest and m is the mass of a particle in the trap.

For the production of Bose-Einstein Condensates it is desirable to confine the atoms very tightly to enable evaporative cooling. In conventional systems this is done by running large currents ($\sim 100\,\mathrm{A}$) through coils near the atoms [37, 38], and one can typically expect to achieve trap frequencies of about 100 Hz. In optical traps and chip based systems it is straightforward to achieve trap frequencies of several kHz [41, 18]. The specifics of chip traps will be discussed in detail in chapter 4.

2.1.2 Optical trapping

An alternative method for trapping laser cooled atoms is to use an optical dipole trap. This technique is commonly used for producing and trapping cold atoms in situations where magnetic traps are unsuitable, such as experiments with spinor condensates [41] or Feshbach resonances [42], or when the optical field can offer novel trap geometries, such as optical lattices [4, 6]. Optical traps are presented here because they are instrumental to our intended implementation of an atomic transistor.

A laser beam close to the resonance of an atomic transition will apply a non-conservative force on the atoms by scattering photons. However, in an off-resonant optical field the atoms will experience an energy shift due to the AC Stark effect. This Stark shift may be calculated to lowest order as

$$U_{dip}(\mathbf{r}) = -\frac{1}{2}\left\langle \mathbf{d} \cdot \mathbf{E} \right\rangle. \tag{2.4}$$

The electric dipole moment induced by the electric field is given by

$$\mathbf{d} = \alpha_{pol}(\omega)\mathbf{E}, \tag{2.5}$$

where $\alpha_{pol}(\omega)$ is the electric polarizability of the atom. The potential the atom experiences is therefore

$$U_{ac}(\mathbf{r}) = \frac{1}{2\epsilon_0 c} Re(\alpha_{pol}(\omega)) I(\mathbf{r}). \tag{2.6}$$

Using the Lorentz model of a classically damped oscillator [43], one finds the optical dipole potential to be

$$U_{dip}(\mathbf{r}) = \frac{3\pi c^2}{2\omega_0}\frac{\Gamma}{\Delta} I(\mathbf{r}), \tag{2.7}$$

where we are again using $\Delta = \omega_l - \omega_0$. In the case of red detuning ($\Delta < 0$) the potential will be attractive and the atoms will be pulled to the maximum of optical field. In the case of blue detuning ($\Delta > 0$) the potential will be repulsive and the atoms will be pushed away from maximum of the optical field. The atoms will still have some finite probability of scattering photons in an off-resonant trap. The scattering rate is given by

$$\Gamma_{sc}(\mathbf{r}) = -\frac{Im(\alpha_{pol}(\omega))}{\hbar\omega} I(\mathbf{r}) = \frac{3\pi c^2}{2\omega_0^2}\left(\frac{\Gamma}{\Delta}\right)^2 I(\mathbf{r}). \tag{2.8}$$

It is easy to see from equations 2.7 and 2.8 that it is preferable to trap atoms at as large a detuning as possible, since that will minimize the spontaneous scattering. Typically how far from resonance one traps atoms is dictated by the available laser power.

Red detuned dipole traps are very common because of their simplicity. One can trap atoms by simply focusing a laser beam down to a tight waist and the atoms will be attracted to the focus. The trap can be made tight in all directions by overlapping two focused laser beams that are perpendicular to one another. Blue detuned traps tend to be a bit more complicated, as one must create a dark region in the optical field surrounded by light. This can be done by crossing Laguerre-Gauusian mode beams[44], or by generating a "bottle" beam trap [45] to create a three dimensional hole in the beam. Blue detuned traps are also used in conjunction with magnetic fields to generate hybrid traps [46]. Although they are more complicated, blue detuned traps have the distinct advantage over red traps that the atoms tend to sit at the minimum of the optical field, which greatly decreases the scattering rate of two similar traps.

2.2 Bose-Einstein condensation

The work in this thesis is focused on production and applications of Bose-Einstein Condensates. Applications of cold atoms can be greatly enhanced by the coherence properties of BEC, and the atom transistor requires condensed atoms with a significant mean field interaction. In this section we present the very basic origins of BEC, and in the next section we will introduce the effects of interactions between atoms in the condensate.

Consider a non-interacting gas of bosons at temperature T. The distribution of particles through the available energy states k with energy ϵ_k respectively will be given by

$$\langle n_k \rangle = \frac{1}{e^{\frac{\epsilon_k - \mu}{k_B T}} - 1}, \tag{2.9}$$

where μ is the chemical potential and k_B is the Boltzman constant. The total number of particles in the system is given by

$$N = \sum_k \langle n_k \rangle . \tag{2.10}$$

The number of particles in excited states is given by

$$N - N_0 = \int_0^\infty \frac{\rho(\epsilon)}{e^{\frac{\epsilon^k - \epsilon_0}{k_b T}} - 1} d\epsilon. \tag{2.11}$$

where $\rho(\epsilon)$ is the density of states. As the temperature of the system is decreased towards zero the number of particles in the ground state increases to the point where it becomes a large fraction of the total atom number. Effectively, the atoms are forced to gather into the lowest energy state because there is no where else to go. This phenomena is called Bose-Einstein condensation, and it is a quantum mechanical phase transition of bosons into a single quantum state. This transition will always occur when the phase space density of the bosons is

$$n\lambda_{dB}^3 = n\frac{h^3}{(2\pi m k_B T)^{3/2}} \approx 2.61. \tag{2.12}$$

or, equivalently, when the gas is cold enough and dense enough that the inter-particle spacing is of the order of the thermal deBroglie wavelength, λ_{dB}.

2.3 Mean field approximation: Many body physics and the Gross-Pitaevskii equation

In the limit of no interactions between bosons the BEC may be treated as a collection of individual particles with a wave function equal to the single particle ground state. In a real condensate of alkali atoms this is not generally the case, and interactions between particles must be considered. It is possible to write down the exact Schrödinger equation for a BEC of N interacting particles with a hamiltonian of

$$\hat{H} = \sum_i \frac{\hbar^2}{2m}\nabla^2 + U(\mathbf{r}_i) + \sum_{i<j} V(\mathbf{r}_i - \mathbf{r}_j). \tag{2.13}$$

Directly solving this many-body equation is a rather cumbersome and impractical approach to addressing problems in BEC physics, as solutions to the equation are usually impossible to obtain. However, in an ultracold gas of bosons one may treat the problem using a “mean field” approach. The interested reader will find an excellent description of mean field theory in the text “Bose-Einstein Condensation” by Pitaevskii and Stringari [47]. At very low temperatures, where the inter-atomic spacing is on the order of the DeBroglie wavelength of the atoms the interactions between atoms may be treated as hard sphere elastic scattering. One can therefore assume an effective potential of the form

$$V(\mathbf{r}) = V_{ext}(\mathbf{r}) + U_0\delta(\mathbf{r}_i - \mathbf{r}_j). \tag{2.14}$$

The interaction potential U_0 can be described, in the Born approximation, as

$$U_0 = \frac{4\pi\hbar^2 a}{m}. \tag{2.15}$$

where a is the s-wave scattering length, and m is the mass of the particle. In the case of a Bose-Einstein Condensate it is appropriate to treat the interactions as a collective change to the energy of the system. This is referred to as the mean field approximation, and is described by the Gross-Pitaevskii Equation (GPE):

$$i\hbar\frac{\partial\psi(\mathbf{r},t)}{\partial t} = \left(-\frac{\hbar^2}{2m} + V_{ext} + U_0|\psi(\mathbf{r})|^2\right)\psi(\mathbf{r},t). \tag{2.16}$$

In the case of a stationary solution the many body wave function may be written as

$$\psi(\mathbf{r},t) = \psi_0(\mathbf{r})e^{-\frac{i\mu t}{\hbar}} \tag{2.17}$$

and the GPE becomes

$$\mu\psi_0(\mathbf{r}) = \left(-\frac{\hbar^2}{2m} + V_{ext} + U_0|\psi_0(\mathbf{r})|^2\right)\psi_0(\mathbf{r}) \tag{2.18}$$

The GPE makes it possible to calculate the parameters of the condensed state, as well as the condensate dynamics. In the case of a large number of atoms in the condensate we may ignore the kinetic energy term in equation 2.18. This is the so-called Thomas-Fermi approximation, which further simplifies the calculation of the parameters of the condensate. In this approximation, the number density can be calculated as

$$n(\mathbf{r}) = |\psi_0(\mathbf{r})|^2 = \frac{\mu - V_{ext}(\mathbf{r})}{U_0}. \tag{2.19}$$

We require that the wavefunction be normalized such that

$$\int d\mathbf{r}|\psi(\mathbf{r})|^2 = N. \tag{2.20}$$

where N the total number of atoms. It is simple to calculate the chemical potential of the condensate for a give potential. For the case of a harmonic trap with

$$V_{ext} = \frac{1}{2}m\left(\omega_x^2x^2 + \omega_y^2y^2 + \omega_z^2z^2\right) \tag{2.21}$$

we find

$$\mu = \frac{15^{2/5}}{2}\left(\frac{Na}{\bar{a}}\right)^{2/5}\hbar\bar{\omega} \tag{2.22}$$

where $\bar{\omega} = (\omega_x \omega_y \omega_z)^{1/3}$ is the geometric mean of the trap frequencies and $\bar{a} = \sqrt{\hbar/m\bar{\omega}}$ is the characteristic trap size [48]. Additionally the size of the cloud along a given eigen axis can be calculated as

$$R_i = \frac{2\mu}{m\omega_i} = \left(\frac{15Na}{\bar{a}}\right)^{2/5} \frac{\hbar\bar{\omega}}{m\omega_i}. \tag{2.23}$$

2.4 Tunneling

Tunneling is a process unique to quantum mechanical systems that relies on the wave-like nature of matter. As was established in Chapter 1 the atom transistor is a device that relies on tunneling of atoms between potential wells, so it is critical to have a good understanding of the conditions under which it will be possible to observe tunneling events.

2.4.1 WKB approximation

WKB is the semi-classical approximation of quantum mechanics that is valid in regions where the potential changes slowly compared to the wavelength of the particle. In the context of a BEC tunneling in a double or triple well potential this is not necessarily a good approximation, given that the wavelength is of the order of the size of the trap. However, in most cases WKB will yield results which are physically meaningful and will be adequate for estimations of tunneling rates for experimental design. Consider a single particle incident on the potential shown in figure 2.2. The energy of the particle is indicated by the squiggly line. Regions I and III are the classically allowed or “transparency” regions, region II is the classically forbidden or “non-transparency” region. We wish to find solutions to the 1 dimensional time independent Schrödinger equation:

$$\psi(x)'' + \frac{2m}{\hbar^2}(E - V(x))\psi(x) = 0 \tag{2.24}$$

in all three regions. First define the two wave numbers

$$\begin{aligned} \kappa &= \frac{\sqrt{2m(E - V(x))}}{\hbar} \\ \eta &= \frac{\sqrt{2m(V(x) - E)}}{\hbar} \end{aligned} \tag{2.25}$$

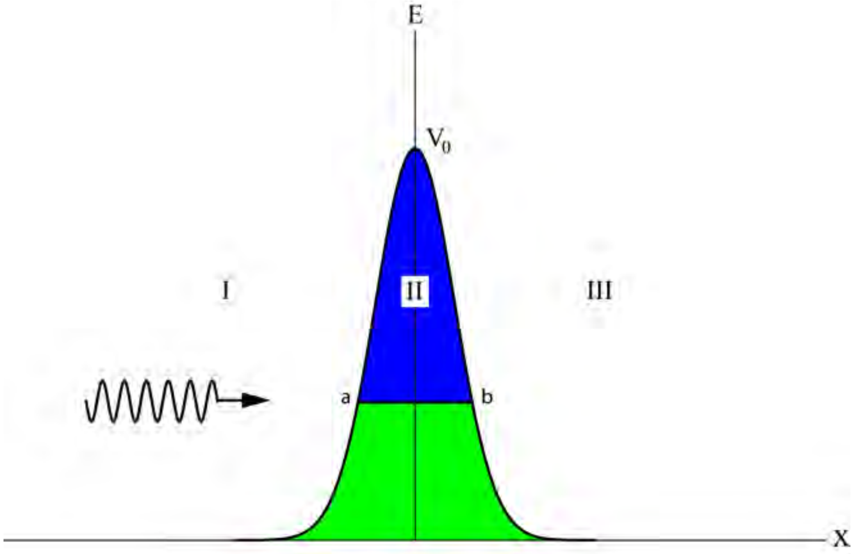

Figure 2.2: (Color). A simple tunneling barrier. The area under the barrier (II) is the classically forbidden, or non-transparency region. The energy of the particle is indicated by the squiggly line on the left, and a and b represent the classical turning points.

and we may write equation 2.24 as

$$\begin{aligned} \psi(x)'' + \kappa^2\psi(x) &= 0 \qquad \text{in the transparency regions} \\ \psi'' + \eta^2\psi &= 0 \qquad \text{in the non-transparency regions} \end{aligned} \tag{2.26}$$

The solutions to equations 2.26 are found in the WKB approximation to be

$$\begin{aligned} \psi_{WKB}(x) &= \frac{A}{\sqrt{\kappa}} e^{\pm i \int_{x_0}^{x} \kappa(x')dx'} \qquad \text{in the transparency regions} \\ \psi_{WKB}(x) &= \frac{A}{\sqrt{\eta}} e^{\pm \int_{x_0}^{x} \eta(x')dx'} \qquad \text{in the non-transparency regions} \end{aligned} \tag{2.27}$$

WKB is not valid at the classical turning points. However, we may make a second approximation by assuming that the potential near the turning points is linear. Making that assumption it is possible join the wave functions at the turning points using the aptly named connection formulae. For a more detailed look at how the connection formulae are derived please see, for example [49]. Going from the transparency region into the non-transparency region we may write eq. 2.27 as

$$\begin{aligned} \psi_{trans} &= \frac{A_1}{\sqrt{k}} \text{Exp}\left(i \int_x^a k(x')\,dx'\right) + \frac{B_1}{\sqrt{k}} \text{Exp}\left(-i \int_x^a k(x')\,dx'\right) \\ \psi_{non-trans} &= \frac{A_2}{\sqrt{\eta}} \text{Exp}\left(\int_a^x \eta(x')\,dx'\right) + \frac{B_2}{\sqrt{\eta}} \text{Exp}\left(-\int_a^x \eta(x')\,dx'\right) \end{aligned} \tag{2.28}$$

The connection formulae tell us that we must satisfy

$$\begin{aligned} A_2 &= e^{-i\frac{\pi}{4}}\left(A_1 + \frac{i}{2}B_1\right) \\ B_2 &= e^{i\frac{\pi}{4}}\left(A_1 - \frac{i}{2}B_1\right) \end{aligned} \tag{2.29}$$

Similarly, going from the non-transparency region to the transparency region we have

$$\begin{aligned} \psi_{non-trans} &= \frac{A_2}{\sqrt{\eta}} \text{Exp}\left(\int_x^b \eta(x')\,dx'\right) + \frac{B_2}{\sqrt{\eta}} \text{Exp}\left(-\int_x^b \eta(x')\,dx'\right) \\ \psi_{trans} &= \frac{A_3}{\sqrt{k}} \text{Exp}\left(i \int_b^x k(x')\,dx'\right) + \frac{B_3}{\sqrt{k}} \text{Exp}\left(-i \int_b^x k(x')\,dx'\right) \end{aligned} \tag{2.30}$$

and again we get the connection conditions

$$\begin{aligned} A_3 &= e^{-i\frac{\pi}{4}}\left(A_2 + \frac{i}{2}B_2\right) \\ B_3 &= e^{i\frac{\pi}{4}}\left(A_2 - \frac{i}{2}B_2\right) \end{aligned} \tag{2.31}$$

Joining equations 2.29 and 2.31 we find the matrix equation

$$\begin{pmatrix} A_1 \\ B_1 \end{pmatrix} = \frac{1}{2} \begin{pmatrix} 2e^{\sigma} + \frac{1}{2}e^{-\sigma} & i\left(2e^{\sigma} - \frac{1}{2}e^{-\sigma}\right) \\ -i\left(2e^{\sigma} - \frac{1}{2}e^{-\sigma}\right) & 2e^{\sigma} + \frac{1}{2}e^{-\sigma} \end{pmatrix} \begin{pmatrix} A_3 \\ B_3 \end{pmatrix} \tag{2.32}$$

Where we have defined the parameter σ as

$$\sigma = \int_a^b \frac{\sqrt{2m(V(x)-E)}}{\hbar} dx \tag{2.33}$$

Solving equation 2.32 we find the transmission coefficient to be

$$T = \left|\frac{A_3}{A1}\right| = \frac{e^{-2\sigma}}{\left(1 - \frac{1}{4}e^{-2\sigma}\right)^2} \tag{2.34}$$

Typically we are interested in cases where the tunneling rate is small, and $e^{-2\sigma} \ll 1$. Therefore,

$$T \approx e^{-2\sigma} \tag{2.35}$$

It is useful to consider how the tunneling strength is modified if the particle starts in a trap rather than free space. In the simpelest case of a two well system, such as the one shown in Fig. 2.3, the system may be thought of as a coupled two well system with coupling strength, in frequency units, of

$$\Gamma_{WKB} = \omega e^{-2\sigma}, \tag{2.36}$$

where ω is the trap frequency of the initial well along the tunneling axis.

2.4.2 Design rules for tunneling experiments

Assuming that the barrier between two adjacent wells is somewhat well behaved we can use the WKB model to develop some design rules for tunneling experiments. Consider a two well potential of the form

$$V(x) = V_0(x + \frac{b}{2})^2(x - \frac{b}{2})^2, \tag{2.37}$$

with a single particle with energy $V_0/2$ in one of the wells. To achieve realistic tunneling rates between the two wells we must insure that σ is of order unity or smaller. If b is very large than V_0 must be very small to compensate. If b is small than V_0 need not be so small. This is intuitively obvious from eq. 2.35: the area under the barrier to be tunneled through is what dictates the tunneling rate, so that area must be small. However, consider how that parameter scales. For the potential given in equation 2.37 we find that

$$\sigma \propto a^4 V_0. \tag{2.38}$$

Clearly the tunneling rate will increase much faster by decreasing the separation between the wells than by lowering the barrier. Also, if one considers the effects of technical noise on the potential it is easy to see that a barrier height that is just barely higher than the energy of one of the wells will be very difficult to control, compared to the height of a tall, thin barrier. Therefore the potential should be designed with b is as small as practical. It is straightforward to show that in order to get tunneling rates on the order of 10-100 Hz with Rubidium atoms that b must be on the order of 1 μm.

2.4.3 Bosonic josephson junction: The two well problem

The atom transistor relies on both mean field interaction of the atoms in the trapping potentials and on the phase coherence of the atoms in the wells. A stronger understanding of the transistor dynamics can be obtained by studying a two well system. The problem of BEC in a double well potential has been studied extensively both theoretically [50, 51, 52] and experimentally [53, 54, 55, 56, 57]. A particularly elegant demonstration of tunneling in Bose-Einstein condensates is the recent experiments performed by the group of Markus Oberthaller at Heidelberg University. We will review the essential details of the theory for that experiment here. The interested reader will find a more complete discussion of this system in [56] and [58].

Atoms are loaded into a two well potential with varying population imbalances between the two wells. The wells are close enough and the barrier is low enough that the tunnel coupling between the two wells is significant. Naively one would expect that the tunneling rate of atoms from one well to the other would simply be larger for the well containing more atoms, and that population of atoms would oscillate between the two wells. This does occur, provided that the population imbalance is relatively small. However, as the population difference is increased by loading significantly more atoms into one well than the other the tunneling rate falls to zero and the atoms are frozen into their respective wells. This phenomena was dubbed macroscopic quantum self-trapping by Raghavan et al [51].

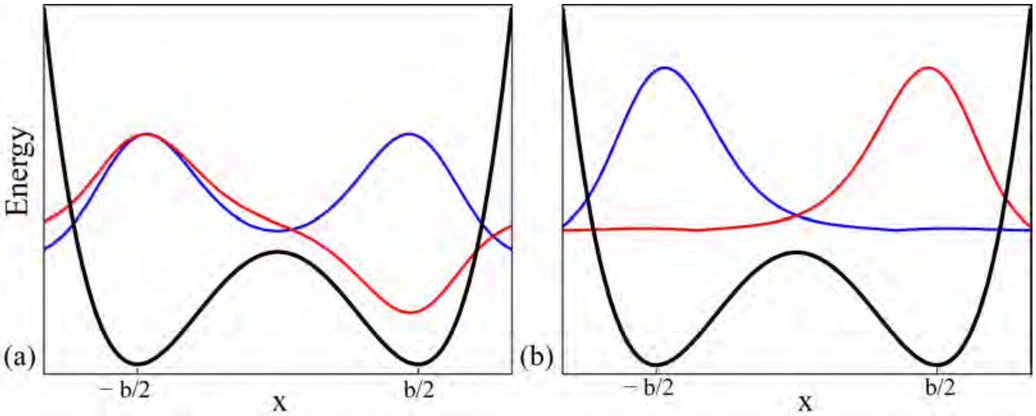

Figure 2.3: (Color). Two well system. (a) The potential for a two well system and the first two eigenmodes Φ_s (blue) and Φ_{as} (red). (b) Spatial modes Φ_L (blue) and Φ_R (red) for the particles in the left or right wells respectively.

To better understand this consider the two well system shown in fig. 2.3. The lowest order eigenstates, Ψ_s and Ψ_{as} of the potential are shown in fig. 2.3(a). The spatial wavefunction for a particle in the left or right well may be written as

$$\begin{aligned}\Phi_L(\mathbf{r}) &= \frac{\Phi_s(\mathbf{r}) + \Phi_{as}(\mathbf{r})}{\sqrt{2}} \\ \Phi_R(\mathbf{r}) &= \frac{\Phi_s(\mathbf{r}) - \Phi_{as}(\mathbf{r})}{\sqrt{2}}\end{aligned} \tag{2.39}$$

and are shown in 2.3(b). The total time dependant wavefunction for the system may be written as

$$\Psi(\mathbf{r}, t) = \Psi_L(t)\Phi_L(\mathbf{r}) + \Psi_R(t)\Phi_R(\mathbf{r}) \tag{2.40}$$

where $\Psi_{L,R}(t) = \sqrt{N_{L,R}} e^{i\phi_{L,R}t}$ and $\phi_{L,R}$ is the phase in the left or right well.

By plugging 2.40 into eq. 2.18 and integrating over spatial coordinates it can be shown [51, 58] that the fractional population imbalance of the two clouds

$$z = \frac{N_L - N_R}{N_{Tot}} \tag{2.41}$$

and the relative phase of the two clouds

$$\phi(t) = \phi_L - \phi_R \tag{2.42}$$

will obey the coupled differential equations

$$\begin{aligned} \dot{z}(t) &= -\sqrt{1 - z(t)}\sin\phi(t) \\ \dot{\phi(t)} &= \Delta E \Lambda z(t) + \frac{z(t)}{\sqrt{1 - z(t)}}\cos\phi(t) \end{aligned} \tag{2.43}$$

where

$$\begin{aligned} \Delta E &= \frac{E_L - E_R}{2K} + \frac{U_L - U_R}{4k} N_{Tot} \\ \Lambda &= \frac{U_L + U_R}{4k} N_{Tot} \end{aligned} \tag{2.44}$$

and we have defined the constants $E_{L,R}$ as the zero point energy of a single particle in the left or right well, $U_{L,R}$ as the on-site interaction energies, and K is the tunneling amplitude between the two wells. $E_{L,R}$, $U_{L,R}$ and K are defined explicitly in [58]. Equations 2.44 are the equations of motion for a non-rigid pendulum of length $l = \sqrt{1 - z^2}$. Numerically integrating equations 2.44 one finds that for initial conditions of small z that tunneling will be enabled, and atoms will oscillate between the left and right wells. For larger values of z, however tunneling will be inhibited as the tunneling rate is no longer fast enough to compensate for the differential phase evolution of the two clouds due to the difference in chemical potentials.

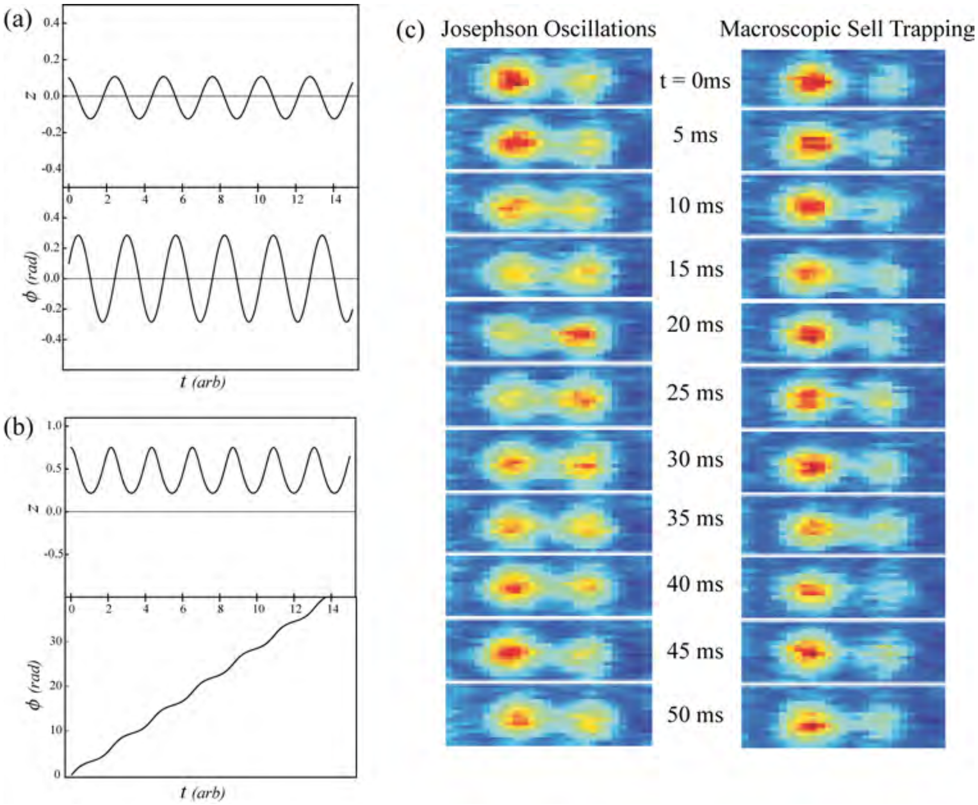

Figure 2.4: (Color). Josephson oscillations in a two well system. (a) Oscillations in the case of small initial population imbalance (small z). Note that ϕ and z both oscillate with the same frequency. (b) In the case of large initial z the atoms get trapped and the relative phase simply grows. This is analogous to the non-rigid pendulum rotating about its axis. (c) Results of experiments performed in Markus Oberthaler's group. The left column shows Josephson oscillations and the right column shows macroscopic quantum self trapping.

The behavior is easy to understand with the mechanical analogy of a non-rigid pendulum: In the limit of small particle number imbalance (small z at $t = 0$) the pendulum oscillates both in angle (phase) and in pendulum length (atom number). As z is increased closer to 1 the pendulum swings to larger and larger angles until the pendulum starts rotating about its pivot point, which keeps the pendulum length from oscillating. Numerical solutions to eqs. 2.44 are shown in fig. 2.4. (a) shows the case of $z \ll 1$ and (b) shows the macroscopic quantum self-trapping limit of $z \sim 1$. Experimental results from [59] are shown in fig. 2.4(c).

The important lesson to take away from this discussion is that the difference in chemical potential not only creates an energetic mismatch between the adjacent wells, but causes the relative phase of the two clouds to evolve at different rates.

2.5 Atom transistor theory

With a solid understanding of both basic tunneling dynamics and the effects of mean-field interactions on tunneling we can now examine the workings of the three well atom transistor. The authors of [28] have studied this atom transistor at some length in the context of both the Gross-Pitaevskii mean field theory, and in the full second quantization formalism. In a similar fashion to the discussion of the two well system described above, one may write the local modes of each of the three wells in the system as a linear combination of the three lowest order eigenmodes of the potential. It is assumed that the number of atoms in the left, or source, well is large so that when atoms tunnel across the barrier the change of chemical potential in that well is small. The dynamics of a given potential may then be studied by only examining the evolution of the local modes of the middle (gate), and right (drain) wells. The system is prepared with a varying number of atoms in the middle well and then allowed to evolve for a set amount of time, after which the number of atoms in the right well is measured.

A detailed description of this analysis is beyond the scope of this thesis, but it is worth repeating the results. Fig. 2.5(a) shows the number of atoms in the drain as a function of atom number in the gate. The solid line in fig. (a) is for the calculation with the source and gate wells having the same phase, and the dotted line shows the same simulation for a retaliative phase difference of $\Delta\phi = \pi/2$. Fig. 2.5(b) shows the atom number in the drain well for a fixed atom number in the gate but for varying phase difference between the source and the gate. Clearly it is important that the system be prepared in such a way that the source and gate have a well defined relative phase, or the device will only work half the time.

The above discussions of tunneling and the two well system are very useful because they inform the system requirements and allow us to start developing design rules. The tunneling rates

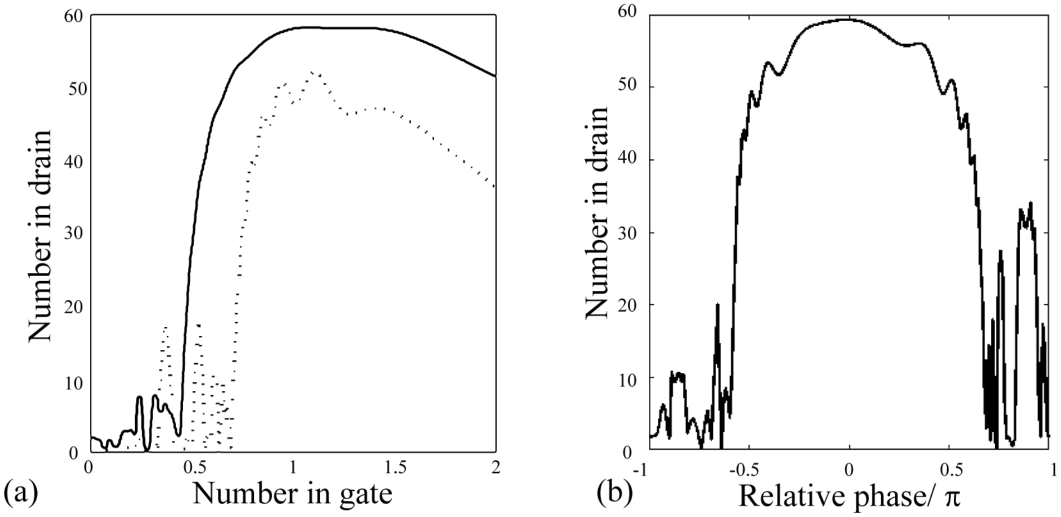

Figure 2.5: Numerical results of mean field calculations of an atom transistor from [28] (a) Gain curve for the atom transistor for $\Delta\phi = 0$ (solid line) and $\Delta\phi = \pi/2$ (dotted line). (b) Atom number in drain as a function of the relative phase of atoms in the source and the gate wells.

must be fast compared to the lifetime of the trapped cloud, which imposes a natural size scale of about 1 μm on potential barriers. It must be possible to load a large number of atoms into the source well compared to the number of atoms that participate in the transistor. To do that it is necessary to make the source well relatively loose, and the gate well extremely tight. A particularly daunting challenge for future atom transistor experiments will be proper preparation of the initial state: the experiment must be designed in such a way that the number of atoms in the gate well is an experimentally controllable and measurable parameter. Finally the relative phase of atoms in the source and gate wells must be well controlled as part of the state preparation.

There are two classes of approaches to implementation of the three well transistor: A trapped-atom transistor, where the atoms are confined in stationary potentials and the system is allowed to evolve for some fixed amount of time; or a waveguide transistor, where the three wells of fig. 1.3 are three guides that run parallel to one another for some finite length L. In many respects a waveguide transistor would be preferable because it is a closer analog to an electronic device, but it is much harder to implement. We have focused our experimental efforts on developing a trapped atom transistor. The primary experimental challenge in that effort is generating a potential appropriate for the task. The details of the approaches we are pursuing are outlined in chapter 5.

Chapter 3

Compact ultracold matter systems

A large part of my work at JILA has been focused on the technological aspects of Bose-Einstein Condensation apparatus. If cold and ultracold atoms are to be useful for practical applications, it is necessary for the systems be compact, robust and easy to use. One would like a device which is small, low power, and requires a minimal amount of maintenance from highly trained technical personnel. This chapter will discuss the development of compact vacuum chambers for BEC, opto-mechanical systems for those chambers and the miniaturization and integration of a BEC system.

3.1 Ultra-high vacuum for Bose-Einstein condensation

At the heart of all cold matter experiments is a vacuum chamber. In the case of BEC systems the vacuum requirements are particularly stringent. Background gasses will collide with the cold trapped atoms and knock them out of the trap. The better the vacuum, the longer atoms may be held and used for experiments. Pressures of less than 10^{-10} Torr are required in large systems, where evaporation cycles typically will take more than a minute [38], and less than 10^{-9} Torr in optical traps [41] and chip based systems [17] where the evaporative cooling process can be much faster, on the order of a few seconds or less. These pressures are readily achievable with modern ultra-high vacuum (UHV) technology, however cold matter systems also require that a contaminant be released into the chamber, namely the particle to be trapped. Typically one captures atoms into a MOT in a high vapor pressure region or from a bright source of atoms before evaporative cooling in an ultra-high vacuum (UHV) chamber. Figure 3.1 shows a block diagram of how nearly every BEC vacuum system is constructed. In many cases a single chamber may serve the purposes of multiple blocks. For instance, both the evaporative cooling region and the experiment are often performed in the same region. The vacuum generally improves from left to right in the diagram.

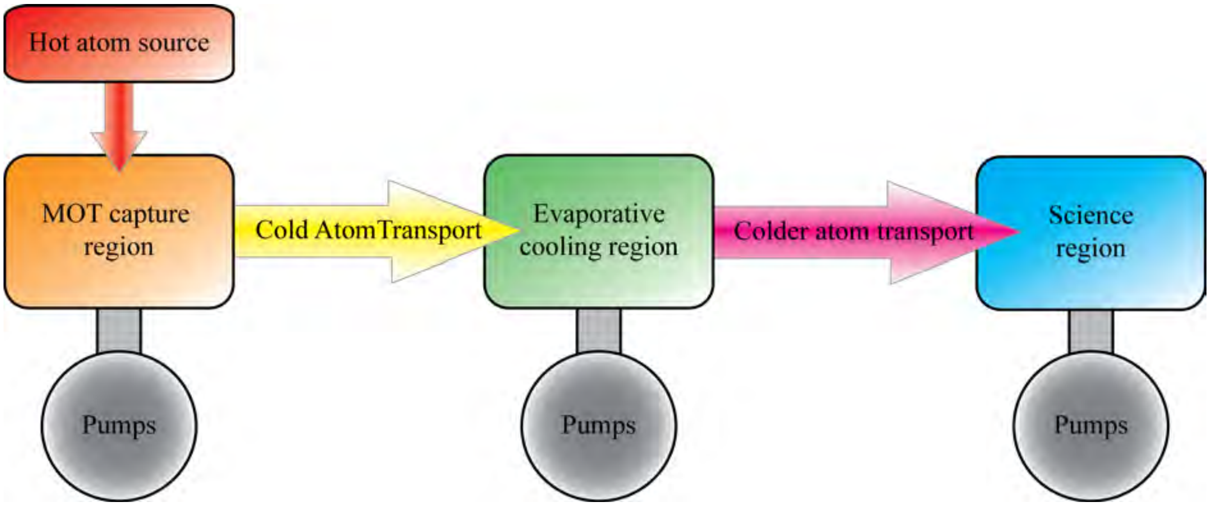

Figure 3.1: (Color). Schematic of an ultra high vacuum system for BEC production.

The atom source is typically a macroscopic quantity of the atom of interest, generally in the form of an ampule of pure metal or an alloy that releases the atom in gaseous form when heated. The atom source is a contaminant to the vacuum, as the atoms introduced to the chamber that are not captured for experiments will contribute to the background gases in the chamber. A successful ultracold matter vacuum system must strike a balance between adequate vacuum quality for the experiment and high enough pressure of atoms to capture a large particle number in the MOT. This is often achieved by building a high vapor pressure region to capture the MOT and a low vapor pressure region for evaporative cooling and experiments. This is shown as being spatially separated in fig. 3.1, but it should be noted that this goal can be achieved in a single chamber by modulating the vacuum pressure temporally rather than spatially. Many successful on chip BEC experiments employ light induced atomic desorption, or LIAD [60], to increase the partial pressure of the gas in the chamber to load the MOT [17, 19, 20].

Ultimately the vacuum quality of interest will be the final pressure in the evaporative cooling and science regions. All vacuum systems will have a rate at which particles enter the vacuum and an effective pumping speed. The ultimate pressure of the system is achieved when the total change of particle number in the chamber per unit time is zero. Particles may enter the system by outgassing from surfaces, diffusion through the chamber walls, leaks through small holes, or other contamination sources such as an intentional atom source. Particles are removed by either active or passive pumps, such as ion pumps and getter pumps. Leaks can be avoided by high quality chamber construction, outgassing rate is minimized by careful choices of chamber materials, and the systems are always baked at as high a temperature as possible to eliminate contaminates.

Maintaining a pressure gradient between the MOT capture region of the system and the UHV parts of the system is often done with a long thin tube. At very low pressures the mean free path between collisions of atoms is large compared to the size of the vacuum chamber, so for a particle in the vacuum to traverse the distance between the two regions it must be traveling directly down the length of the tube. This quality is described by the conductance of a component, which for a long tube of radius a and length l is given by [61]

$$C = \frac{2}{3}\frac{\pi\bar{v}a^3}{l}, \tag{3.1}$$

where $\bar{v}$ is the average velocity of a particle in the chamber. In the limit of $l \leq a$ equation 3.1 is given by

$$C = \frac{\bar{v}\pi a^2}{4}. \tag{3.2}$$

This fast scaling of the conductance with the tube's diameter makes it desirable to separate the two regions with as long and as thin a tube as possible. There are two constrains on this: first the tube must be large enough that it is practical to transport the atoms between chambers. Second it must be possible to achieve high quality vacuum in the tube. If the tube is too thin or too long the pressure in the tube could be higher than the pressure of either the capture region or the evaporative cooling region.

Consider the two chamber system shown schematically in fig. 3.2. The left chamber is

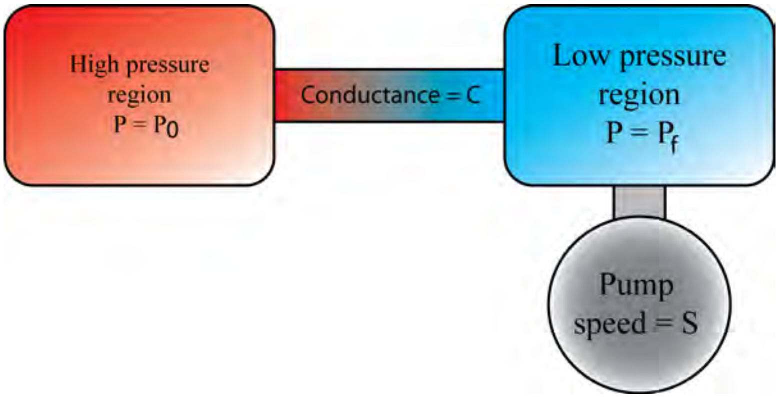

Figure 3.2: (Color). Schematic diagram of a two chamber system with differential pumping between the two chambers. This is a common configuration for many BEC systems.

maintained at a constant pressure P_0, and the right chamber is pumped out by some collection of active and passive pumps with total pumping speed S_{eff}. The two chambers are isolated through a connection that has a conductance C. The pressure in the second chamber will be given by

$$P_f = \frac{C}{C + S_{eff}} P_0. \tag{3.3}$$

If C is small compared to S_{eff} that it will be possible to maintain a substantial pressure difference between the two chambers.

3.2 Compact vacuum chambers

The two subsystems that are the most problematic for miniaturization are the optical system and the vacuum chamber. The rest of the apparatus, such as the power supplies and the computer control, present technical challenges for miniaturization, but all of those issues are well addressed by the incredible work done in the electronics industry. We will discuss optical system miniaturization in detail later in this chapter.

While there are of course technical challenges involved with fabricating miniature vacuum chambers, there are some more fundamental issues that ultimately limit the size of the apparatus. The first is that the atoms will scatter photons at a finite rate, which imposes a restriction on the overall size of the region where laser cooling is performed. This can be understood quite simply by examining a rather trivial laser cooling example. Consider a rubidium atom at temperature T. The atom will travel with average velocity

$$V_{Rb} = \sqrt{\frac{3k_BT}{m_{Rb}}}. \tag{3.4}$$

The largest force a laser can exert on the atom will be when the laser intensity is well above saturation, and the atom will scatter approximately Γ photons per second. In that case the atom will feel a maximum force from the laser of

$$F = \frac{\hbar k\Gamma}{2}. \tag{3.5}$$

To bring the atom to rest it must interact with the laser beam for a minimum length of

$$\Delta x = \frac{3k_bT}{2\hbar k\Gamma}, \tag{3.6}$$

For atoms at T = 30K this length is still nearly 2 cm. This simple derivation teaches two lessons: For a reasonable size chamber it is only possible to capture the coldest of the atoms from a vapor cell, and that to trap a significant atom number the chamber must accommodate cooling beams that are ~1 cm in diameter. The notable exception to the first lesson is the Zeeman slower, where a large fraction of the thermal distribution is cooled from a hot beam of atoms. Zeeman slowers, however, do not lend themselves to miniaturization, as they are typically ~1m in length [38].

The second miniaturization issue pertains to maintaining low vacuum pressure in small chambers. Consider a spherical chamber of radius r with no active pumps. The chamber walls will have some finite outgassing rate, Q and some pumping speed S. The pressure will be directly proportional to both the pumping speed and the outgassing rate, and inversely proportional to the volume. The pumping speed and outgassing will scale directly with the surface area, which means that the ultimate pressure achievable in the chamber will be proportional to $1/r$. This is difficult to quantify, as it is strongly dependant on the chamber geometry and the materials used, but the heart of the problem is clear: to achieve ultra high vacuum conditions in a small chamber one must increase the pumping speed per unit volume faster than the chamber size is decreased. With cold matter systems the problem is enhanced, as it is necessary to introduce a roughly constant flux of the atomic species to be trapped into the system. Additionally, the available atoms sources are not particularly clean. In the case of Rubidium, ^{85}Rb is the most abundant isotope, comprising about 66% of Rubidium metal. The majority of Rubidium BEC experiments use ^{87}Rb, which makes up the other 33%. The result is that whenever Rubidium is released into the chamber, two thirds of the gas is an unnecessary contaminant to the vacuum. Also, we have measured that the salt based sources, such as the ones from SAES, release a substantial amount of hydrogen into the system. It is possible to get isotopically pure Rubidium, but it is prohibitively expensive, and it is difficult to integrate in a small system.

3.2.1 Single chamber BEC cells

The early efforts in our lab to develop compact chip-based BEC chambers[19] were based largely on work done in the group of Theodore Hansch [17]. Using the single chamber BEC production process developed by that group, we fabricated a series of vacuum systems, such as the one shown in Fig 3.3. The notable advancements of this chamber over the work done by [17] is the compact size, and the fact that the atom chip comprises one wall of the vacuum chamber. The details of the atom chips used in this and the following systems will be discussed in greater detail in chapter 4.

We were successful in producing BEC with this design, but there was a lot of room for improvement. Because the chamber was assembled with epoxy the bakeout temperature was limited to less that 150 °C, which made it difficult to achieve good vacuum in the small system. This epoxy base approach also led to difficulties with leaks in the chamber developing during bakeout, and would limit the lifetime of the chamber [62]. Also, because of the difficulty with vacuum processing the yield of cell production was low.

To mitigate the problems with the epoxy limiting the bakeout temperature and the vacuum quality we began investigating alternative approaches to assembling vacuum chambers. Through a collaboration with the Sarnoff Corporation we learned that silicon has the useful property of being a material which can be anodically bonded to Pyrex glass[63]. Anodic bonding is a process

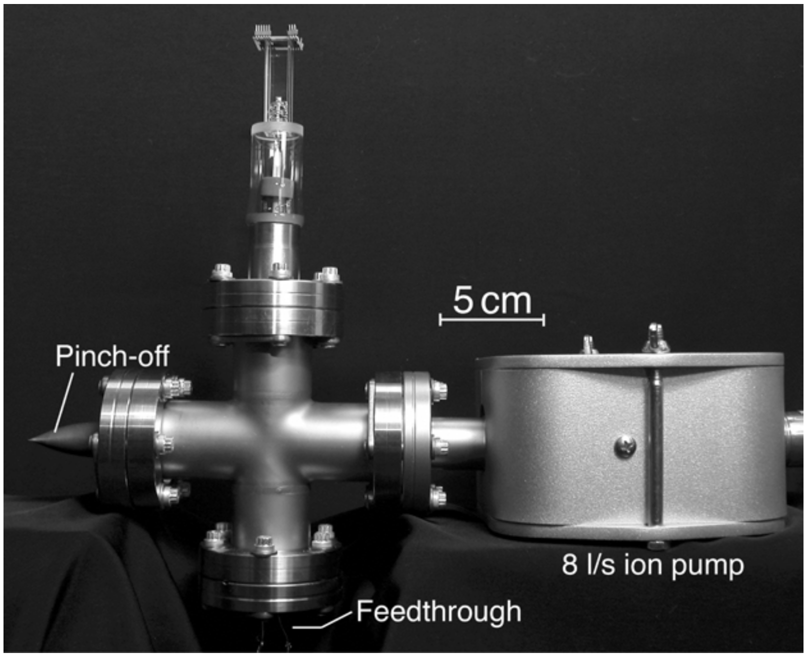

Figure 3.3: First generation single chamber vacuum system for BEC production

by which two dissimilar materials are joined through the application of heat and an electric field. The most common material choices for this process are silicon and borosilicate glass, specifically Corning 7740 Pyrex or Shott Borofloat 33. The only particularly challenging part of the anodic bonding process is that both surfaces must be polished flat and very clean. If the surfaces are properly prepared it is a very robust process. A schematic bonding setup is shown in figure 3.4a. As will be seen throughout this thesis, we have employed this anodic bonding process extensively for producing hermetic joints in vacuum systems. The bond joint is completely hermetic, requires no epoxies or additional sealing, and is robust at temperatures $> 400°C$.

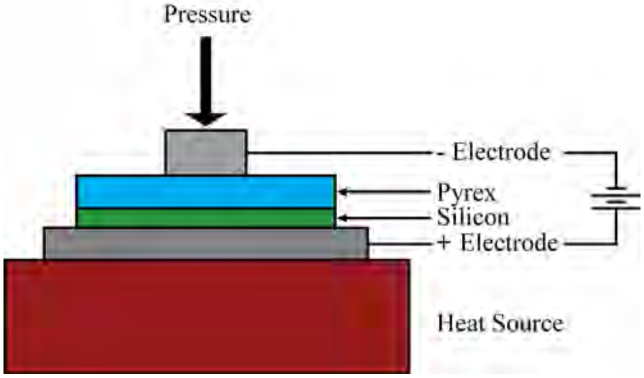

Figure 3.4: (Color). Setup for anodic bonding.

Incorporating anodic bonding into the vacuum fabrication process generated some other challenges with the atom chips which will be covered in chapter 4, but the elimination of polymer based epoxies allowed the chambers to be processed at temperatures as high as 300°C, which dramatically improved the vacuum quality. However, the single chamber system used LIAD to modulate the vacuum pressure, which proved to be incompatible with the high temperature bakeout. We believe that the LIAD process is dependant on contaminants in the chamber. Empirically we found that as the cells were baked at higher temperatures the chambers got cleaner and cleaner, and the LIAD simply stopped working. This was not a lesson that came cheap. Fig. 3.5 shows a small sample of the chambers that were made during the development process.

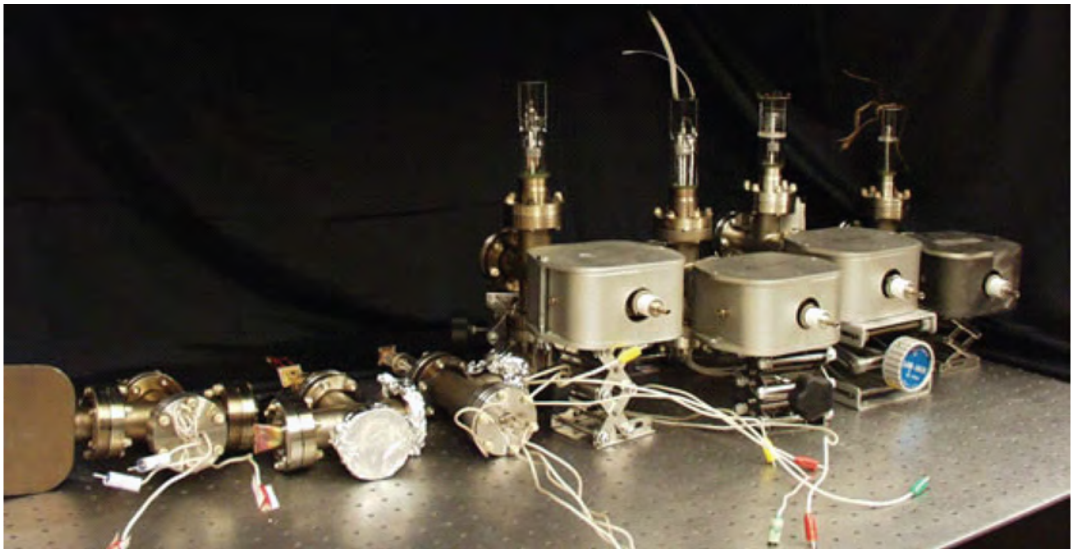

Figure 3.5: (Color). Graveyard of early generation design iterations.

3.2.2 All-glass double MOT cell

Single chamber system are not ideally suited to practical BEC applications. LIAD pressure modulation is unreliable, and the time needed to pump down the chamber after increasing the pressure makes it impossible to achieve a high production rate. After careful examination of the alternatives we began pursuing a cell design where a 2D MOT [64] would load a six beam 3D MOT. This approach was chosen for several reasons. The 2D MOT does not hold any atoms, rather it cools them and drives them out of the high pressure chamber. This is in contrast to a Low Velocity Intense Source (LVIS)[65] or a cold beam from a pyramid MOT[66], where the atoms are trapped in a MOT before they are ejected in the cold beam. These sources require reasonably good vacuum, or the atoms will be knocked out of the trap by collisions with background gases. The 2D MOT, on the other hand, is extremely dilute, so the cooled atoms are unlikely to collide with a background atom on the way out of the MOT. Schoser et al [67] have shown good performance from a 2D MOT with pressures as high as 2×10^{-6} Torr, which is substantially higher than what is typically desirable for a 3D MOT. The result is that the pressure in the 2D MOT chamber does not need to be well maintained to achieve a high flux of atoms, so the chamber may be built without any active pumps connected directly to it. The first double MOT chamber built in our lab is shown in fig. 3.6. This all-glass double MOT cell was a significant milestone in the development of compact vacuum systems because with it we successfully demonstrated a working 2D MOT loading a 3D MOT with no active pumps in the 2D MOT chamber, which was evacuated through a 1mm pinhole.

With this all glass cell we were able to demonstrate fluxes as high as a few 10^8 atoms/second and saw 6 beam MOTs as large as 4×10^8 atoms. This was a dramatic improvement over the atom numbers in the single chamber system, where a typical MOT would be $\sim 2 \times 10^7$ atoms.

3.2.3 The double MOT BEC cell

The success of the all-glass double MOT led to the development of a compact two chamber cell for producing BEC on an atom chip. Although the glass blown approach is rather elegant,

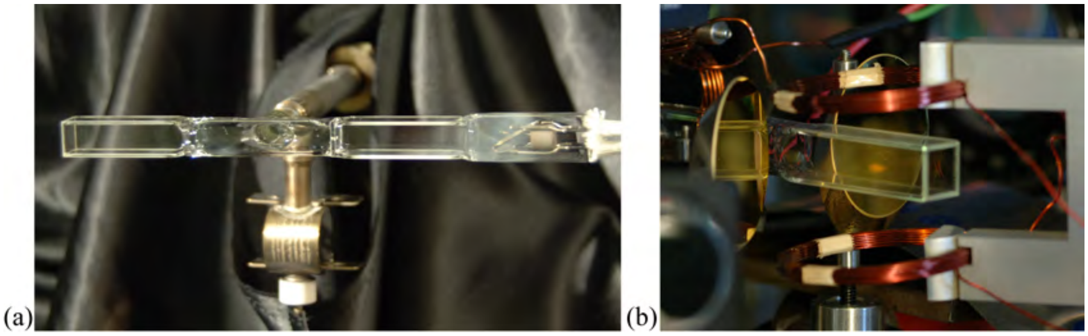

Figure 3.6: (Color). (a) All glass double MOT cell before pinchoff. Rubidium source and non-evaporable getter are shown on the far right and are directly attached to the 2D MOT cell. The 2D MOT cell is connected through a 1mm pinhole in a glass wall to the 3D MOT cell and the ion pump. (b) A 6-beam MOT of about 10^8 atoms captured in the 3D MOT chamber.

it requires a significant amount of skilled labor to make and the entire chamber has to be made at one time. To make the systems more modular the double MOT BEC chamber was designed using a hybrid of conventional vacuum assembly techniques, such as conflat flanges, and some more advanced assembly techniques, namely anodic bonding. The details of this design is already discussed in detail the PhD theses of Matthew Squires and Stephen Segal [23, 24], but since this chamber is central to most of the experiments described in this thesis it is worth reviewing. The chamber is shown in fig. 3.7.

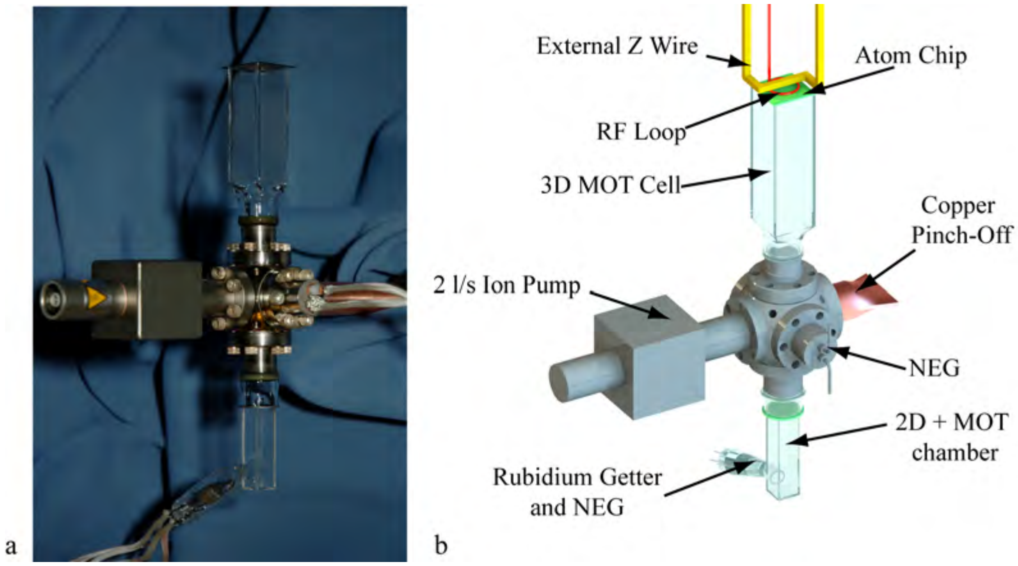

Figure 3.7: (Color). (a)Standard two chamber double MOT BEC cell. (b) Parts of the double MOT BEC cell.

There have been two generations of the 2D MOT cell for this chamber. The original design, shown in fig. 3.7, the left side of fig. 3.8 and described in [23], was a simple modification of the 2D MOT source used in the all-glass double MOT cell. The chamber is made from a 1cm pyrex fluorimeter cell that is polished on the open end and has a tail attached containing a rubidium dispenser (SAES p/n 5G0125)) and a non-evaporable getter (NEG) (SAES p/n HI/7-6). The NEG in place to pump hydrogen released by the rubidium dispenser. The dispenser and getter are electrically connected to ambient using a tungsten pin seal through the glass. The open end of the cell is anodically bonded to a 1mm thick silicon disk with a 750 μm pinhole through the center.

The silicon disk is anodically bonded on the other side to a glass-to-metal transition on a 1.33" CF flange. The pinhole has a conductance of 0.1 ℓ/s, which maintains a two order of magnitude pressure difference between the 2D and 3D MOT chambers. This original design was very effective, but the tail was fragile and prone to breaking off. To address this we developed the design shown on the right side of fig. 3.8. The new cell eliminated the tail by moving the pin seals to a glass flare attached directly to the glass to metal seal. In addition to being more robust, the design incorporates a 2cm fluorimeter cell, which significantly improves optical access to the 2D MOT and allows for higher fluxes at lower pressures.

Figure 3.8: (Color). 2D MOT source tubes. The first generation source tube is shown on the left, and the second generation cell is shown on the right.

At the center of the cell is a 6 way CF spherical cube (Kimbal Physics p/n MCF133-SC6) which connects the 2D MOT, the 3D MOT cell, a second non-evaporable getter, the 2 ℓ/s ion pump (Varian p/n 9190520), and the copper pinch-off tube. The chamber is evacuated and brought to UHV conditions through the pinch-off tube, which connects to a pumping station. After pinch-off the pressure is maintained by the ion pump and the non-evaporable getters at less than 10^{-9} Torr. The 3D MOT cell is glass blown to a 1.33" CF flange and polished on the opposite end where it is bonded to an atom chip. The 3D MOT cell is custom fabricated from reasonably high quality Pyrex glass, and is 2cm square internal dimensions with a 1.5mm wall thickness. It is desirable to have AR coatings on the cell walls to maximize transmission of the MOT beams and to minimize interference between reflections on the surfaces, which can lead to problems with absorption imaging. Because of the way the chamber is made it is not possible to coat the glass before the cell is assembled. We have worked with an external vendor to develop a coating process using low pressure chemical vapor deposition (LPCVD) to coat the inside and outside of the cells after they have been assembled. An example of the BEC cell before and after AR coating is shown in fig. 3.9.

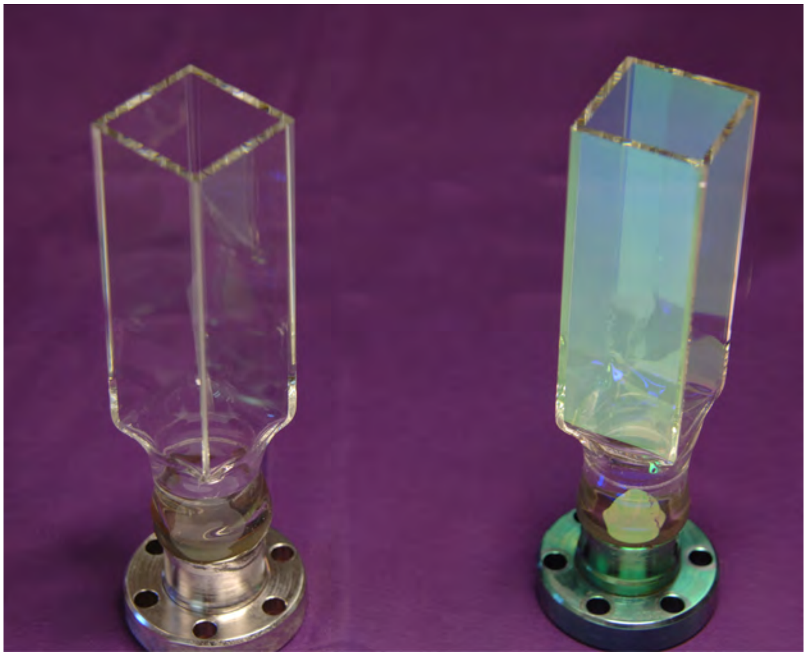

Figure 3.9: (Color). 3D MOT cells shown before (left) and after (right) LPCVD coating process.

The functionality of the system is dictated by the atom chip, which is completely independent from all of the other components of the system. This enables an experimental operation of simply switching vacuum chambers when the time comes to replace the atom chip for a new experiment. This makes the BEC cell much like a vacuum tube, which is connected to a standard socket and swapped with different tubes for different functionality. The socket for our vacuum cells will be discussed later in this chapter and in chapter 6.

3.2.4 Channel cell technology

The double MOT BEC cell described above is an excellent piece of equipment, but it has a few distinct limitations. The design is not particularly manufacturable on a large scale. CF flanges, while effective and useful in the laboratory, are not a good design choice for a mass produced system: They are expensive to make and labor intensive to assemble. The large amount of stainless steel in the system is not ideal for maintaining vacuum for extended periods, as stainless tends to outgas hydrogen unless baked out at temperatures higher than the glass can withstand [68]. Finally, the design is particularly limited in its geometry; specifically, it is extremely cumbersome to add chambers to the system.

This last point is very important for applications of cold atoms. As mentioned in chapter 1 a useful ultracold mater device must have a repetition rate that is sufficiently high for the needed measurement to be taken. A gyroscope that only provides one data point every minute, or even every few seconds, is not a particularly useful tool. This is an interesting challenge for ultra cold atoms, since, as of the writing of this thesis, all of the sources of BECs are pulsed in operation and take at least 3 seconds to produce a single condensate [23]. One possible solution to this problem is to spatially separate the steps of the sample preparation in addition to temporally separating them. This is shown as a block diagram in fig. 3.10. In this conception of an ultracold matter device the atoms are pre-cooled optically before being transported to a dark region where a cloud could undergo RF evaporation while another sample is being cooled in the first chamber. Once BEC is achieved the atoms can be shipped to an experiment chamber while the second set is moved into the evaporation region and the process continues. Using this “string of pearls” approach one could produce a quasi continuous supply of BEC atoms to the instrument.

A multi-chamber system of this nature is very difficult to build in a compact way using conventional vacuum components. Each additional chamber requires additional glass to metal seals, pumps and pumping pathways, vacuum and/or optical isolation, and all of the associated hardware. To address these problems we have developed some alternative approaches to miniature vacuum

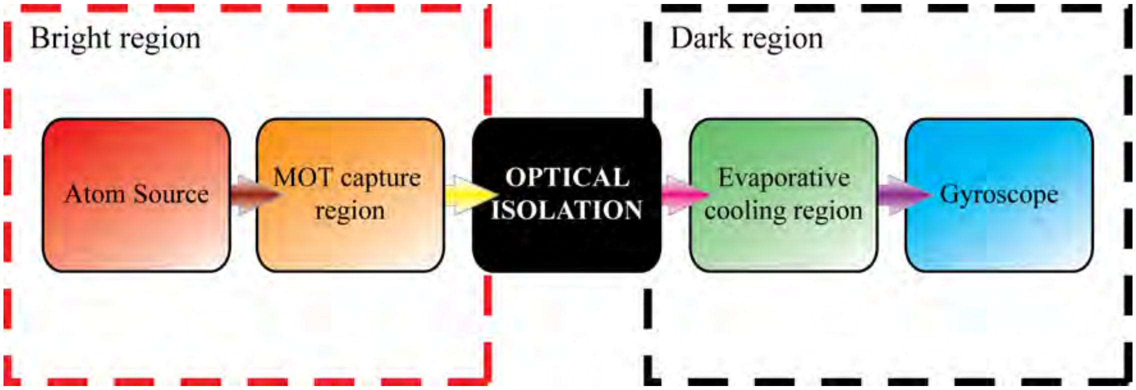

Figure 3.10: (Color). Schematic of a multiple chamber ultracold matter system to enable a string of pearls production approach. In principle one could operate all of the parts of the chamber simultaneously with a different cloud of atoms in each.

system fabrication. Taking a cue from work done making microfluidic systems with micromachining techniques and anodic bonding [69, 70], the chamber is made by replacing the stainless steel cube with a monolithic piece of silicon machined with carefully chosen holes and trenches. The silicon surfaces are then sealed with pyrex cells and windows that are anodically bonded to the polished faces of the silicon. Fig. 3.11(a) shows a simple example of this technology, where two chambers are connected through a silicon frame. Fig 3.11(b) shows how this concept can be used to replicate the double MOT chambers described in the previous sections.

This approach to vacuum cell construction is potentially a very powerful tool. Fig. 3.11 shows how the channel cell approach can be used to build two chamber systems, but it is straightforward to extend this by simply adding chambers to the silicon backbone. Also, as mentioned above, optical isolation in a continuously operating BEC system will be critical. The channel cell technology makes it possible to integrate optical isolation into the chamber without adding any real complexity. One possible approach to optical isolation is shown in fig. 3.12. The silicon structure is fabricated so there is no direct path between the light and dark regions of the vacuum system. Along the trajectory of the atoms, shown as a red dashed line, the light has many paths by which it is forced out of the system.

The cartoons in figs. 3.11 and 3.12 are fairly simple, but the implementation of a functional channel cell turns out to be quite challenging. The silicon frame is difficult to fabricate, as silicon requires abrasive or chemical processes to machine. All of the optical surfaces must be flat and clean before they can be bonded. A typical flatness specification for anodic bonding is a peak to valley deviation of less than $\lambda/2$, which can be quite challenging to achieve on large parts. All of the anodic bonds must be done sequentially, making the assembly process very time consuming. Finally the chamber must be connected to a vacuum system for pump down and bake out, which requires some sort of interface to conventional vacuum components.

Despite these hurdles we have fabricated some prototype versions of the channel cell technology. The first generation cell is shown in fig. 3.13. This channel cell incorporates a three chamber design: Rubidium atoms are supplied to a 2D MOT chamber through a manifold connection to a

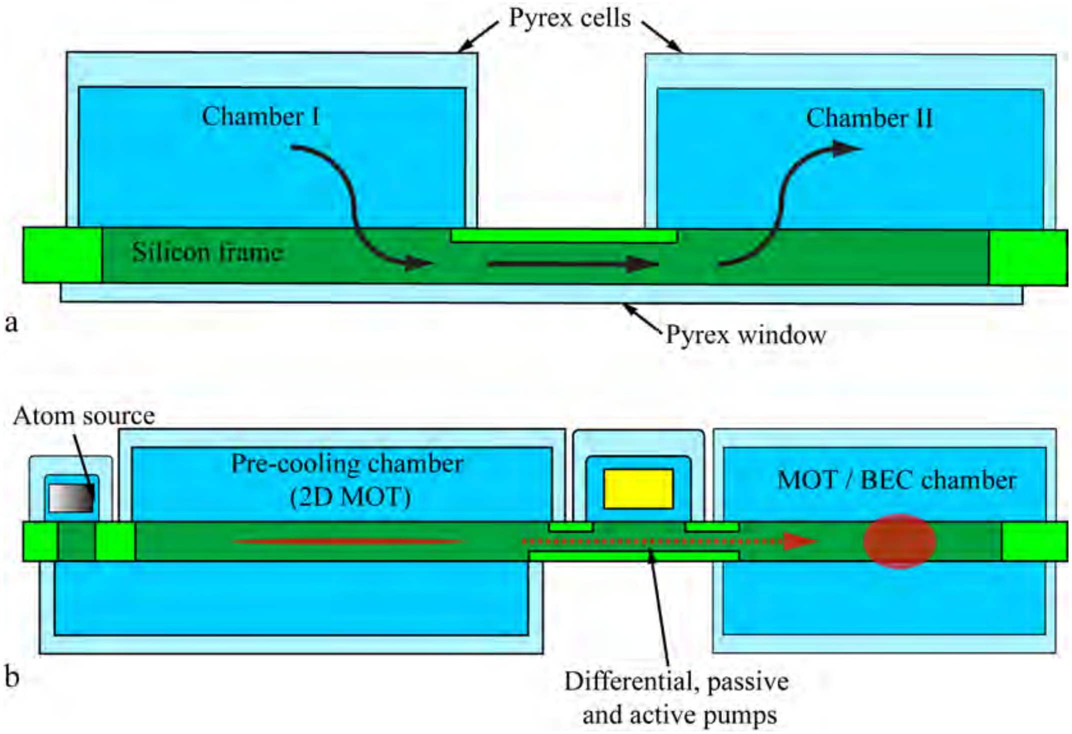

Figure 3.11: (Color). Cross section view of the channel cell approach to vacuum systems. (a) A simple two chamber system where the two chambers are connected through a pathway made in the silicon. Light green/blue show the surface of the cross section and dark green/blue represent real surfaces in the chamber. (b) A more evolved version of the chamber in (a), showing a system that could replace the double MOT BEC cell described in the previous section.

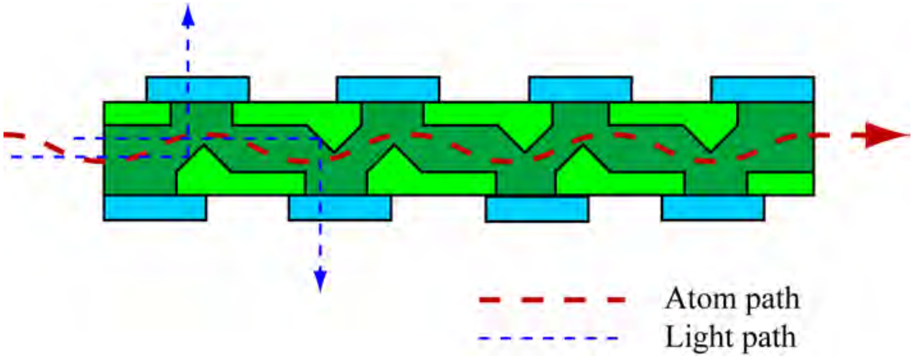

Figure 3.12: (Color). A proposed approach for building a chamber which optically isolates two chambers inside a channel cell. The atoms take a meandering path (red dashed line) through the isolation region while the light is reflected off surfaces that direct that light out of the vacuum system.

conventional electrical feedthrough. The atoms from the 2D MOT are sent through a series of apertures designed for differential pumping into a second chamber for re-capture in a 3D MOT. As can be seen in the picture, the 3D MOT cell is a flat chamber with a 4 mm internal width. This is done to decrease the overall volume of the system and to make it possible to get magnetic coils extremely close to the atoms for magnetic trapping and transport a third chamber for BEC production. The BEC chamber is directly connected to the 3D MOT region with a high conductance aperture, and one wall of that chamber is made of an atom chip. The usual method of absorption imaging of a BEC by shining a probe beam parallel to the atom chip is not available in this chamber because of the silicon frame. To address this the atom chip is made with a window anodically bonded to the chip surface to allow for through-chip imaging. The subject of windows on atom chips will be discussed in much greater length in chapter 5.

The vacuum connections in this design are made through a large glass manifold across the entire back side of the silicon frame. Through this manifold there are connections made to two copper pinch off tubes used to pump down the cell, a 0.4 ℓ/s ion pump and to four electrical feedthroughs that connect to non-evaporable getters and the rubidium dispenser.

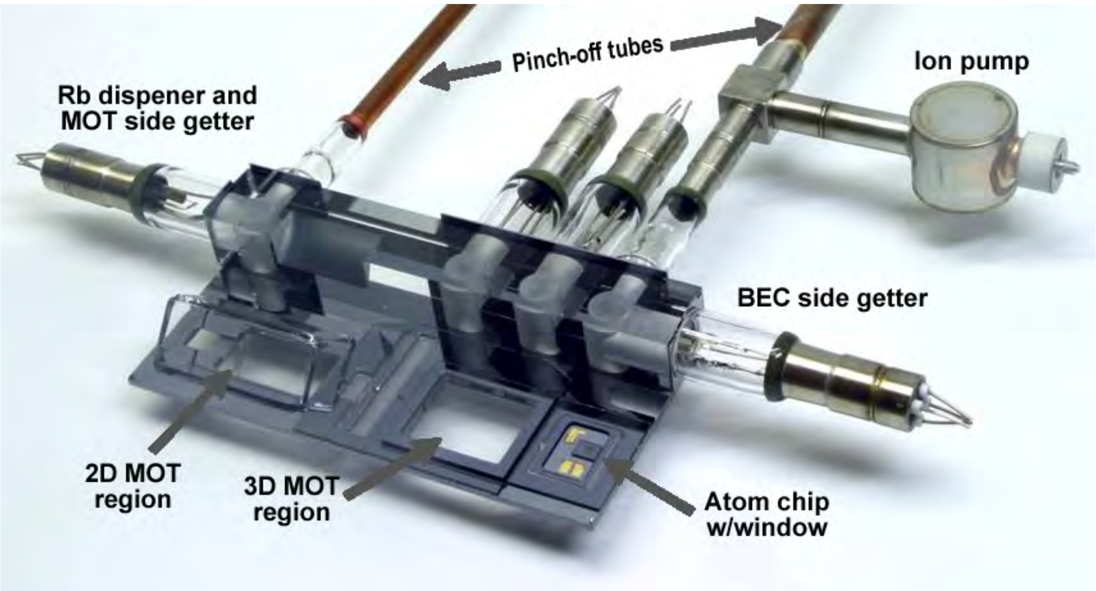

Figure 3.13: (Color). Version 1 Channel Cell

With this design we successfully demonstrated loading of atoms from a 2D MOT to a 3D MOT, but were never able to get enough atoms with good enough vacuum quality to attempt to make BEC in the cell. The main issues were inefficient coupling of atoms from the 2D MOT to the 3D MOT and the complex manifold makes it difficult to achieve good vacuum. To address these problems a second generation of the channel cell was designed and fabricated. The chamber is shown in fig. 3.14. This cell incorporates larger volume MOT chambers to improve the capture volumes of both the 2D and 3D MOTs. The 2D MOT cell includes in-vacuum optical surfaces that allow for 2D(+) MOT operation of that chamber which will improve the capturable output flux from that chamber by about one order of magnitude. Also, this cell eliminates most of the glass manifold from the version 1 design, which subsequently eliminates many of the tortured paths that obstruct pump out. As of the writing of this thesis this design has not been used for any experiments.

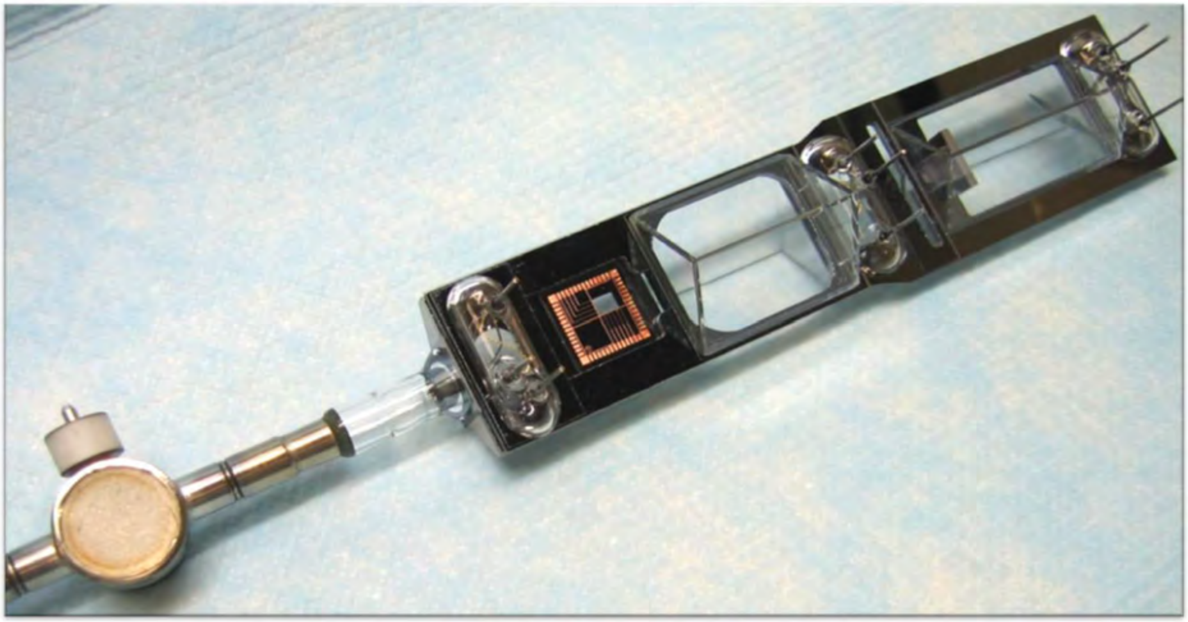

Figure 3.14: (Color). Version 2 Channel Cell

The channel cell is a very elegant proof of principle demonstration of a monolithic approach to vacuum chamber fabrication. The approach offers a way to make complex chambers that would not be possible to make in a compact manner with off the shelf components. Also, the techniques used to make the cell lend themselves to mass production. Much like CMOS components, channel cells are devices which are tremendously expensive to make in small quantities, but could be very cheap to produce on a much larger scale.

3.3 Opto-mechanics

Laser cooling and trapping of atoms requires a substantial optical system surrounding the vacuum chamber. In the case of the above described double MOT cell, it is necessary to have 5 beams shining through the 2D MOT region, four for radial cooling and 1 for the push beam; and at least 8 through the 3D MOT chamber, 6 for cooling, 1 for optical pumping and 1 for probing. If the MOT beams are retro-reflected the setup can be simplified, reducing the number of separate beam paths to 3 for the 2D MOT and 3 for the 3D MOT. To correctly align the beams each must have 2 kinematically mounted mirrors, and each beam must have at least a quarter wave plate retarder to achieve the correct polarization for laser cooling. If all of the beams for each MOT are generated from a single beam then the system will also need 4 beam splitters. The 2D MOT will perform best with elongated beams, which requires additional components, such as a cylindrical telescope, to generate.

Conventional systems are typically built with off the shelf components, and are built around the vacuum chamber, making any changes to the chamber very difficult. An example of such a system is shown in fig. 3.15. Such setups are practical for research, but they do not lend themselves to applications where the entire apparatus must be compact. In this section we will present two examples of more integrated optical systems for cold and ultracold atoms.

3.3.1 Compact optical setups I: The channel cell

For a demonstration of the channel cell technology we built an integrated optics package for the cell shown in fig. 3.13. This package, shown in fig. 3.16, was designed to be as compact as was practical. The package is built in two halves: The left consists of three plates and holds the

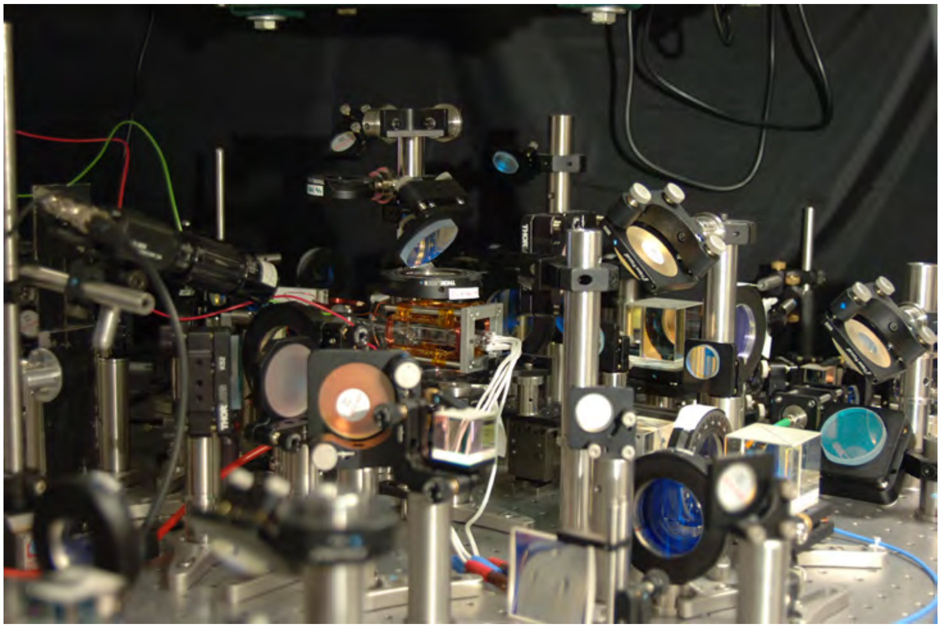

Figure 3.15: (Color). Optical setup for the all glass double MOT cell

optics for the 2D MOT. The light for the 2D MOT is brought in on two optical fibers that are each collimated with a pair of cylindrical lenses to generate beams that are $7mm \times 20mm$ $1/e$ diameter. Each beam is reflected off a single mirror before it passes through the cell and is retro-reflected back off a combined quarter wave plate and mirror. The right half of the package is another three plates that hold the optics for the 6 beam MOT. Again, each beam is launched from a fiber and colimated with a spherical lens to give a $7mm$ beam, and each beam is reflected off a single mirror before passing through the cell. Using a fiber for each beam eliminates the need for beam splitting optics and substantially reduces the size of the package. Using only one mirror per beam is a less than ideal, as it is not possible to align the beams through the cell precisely, but it reduces the number of optics and is an acceptable compromise for the demonstration of a MOT. The magnetic field for the 2D and 3D MOTs is generated with sets of permanent magnets, which eliminates two power supplies from the system. The volume of the entire package is about 5 liters.

This package was built and demonstrated through our collaboration with Sarnoff. The channel cell was built at Sarnoff, then sent to JILA for vacuum processing and testing. The optics package was built and aligned in our lab at JILA, shipped to New Jersey where it was combined with a compact laser system developed at Sarnoff. The entire system was taken to Washington D.C., where we demonstrated cold atoms on the desk of the director of DARPA.

3.3.2 Compact optical setups II: The double MOT cell

The optics package for the double MOT BEC cell was designed with the intention of being more flexible than the channel cell package at the cost of being slightly less compact. The double MOT cell is substantially more mature than the channel cell, and the functionality of a compact optics package is designed to allow for work beyond demonstration of ultracold matter. This optics package is the heart of our portable BEC system which will be described later in this chapter.

The package construction is shown in fig 3.17. The assembly consists of four independent stages coupled by a set of four rails. The lower two stages, shown in fig. 3.17(a) are the atom source stages. The bottom stage is a baseplate that supports the rest of the assembly and the optics for

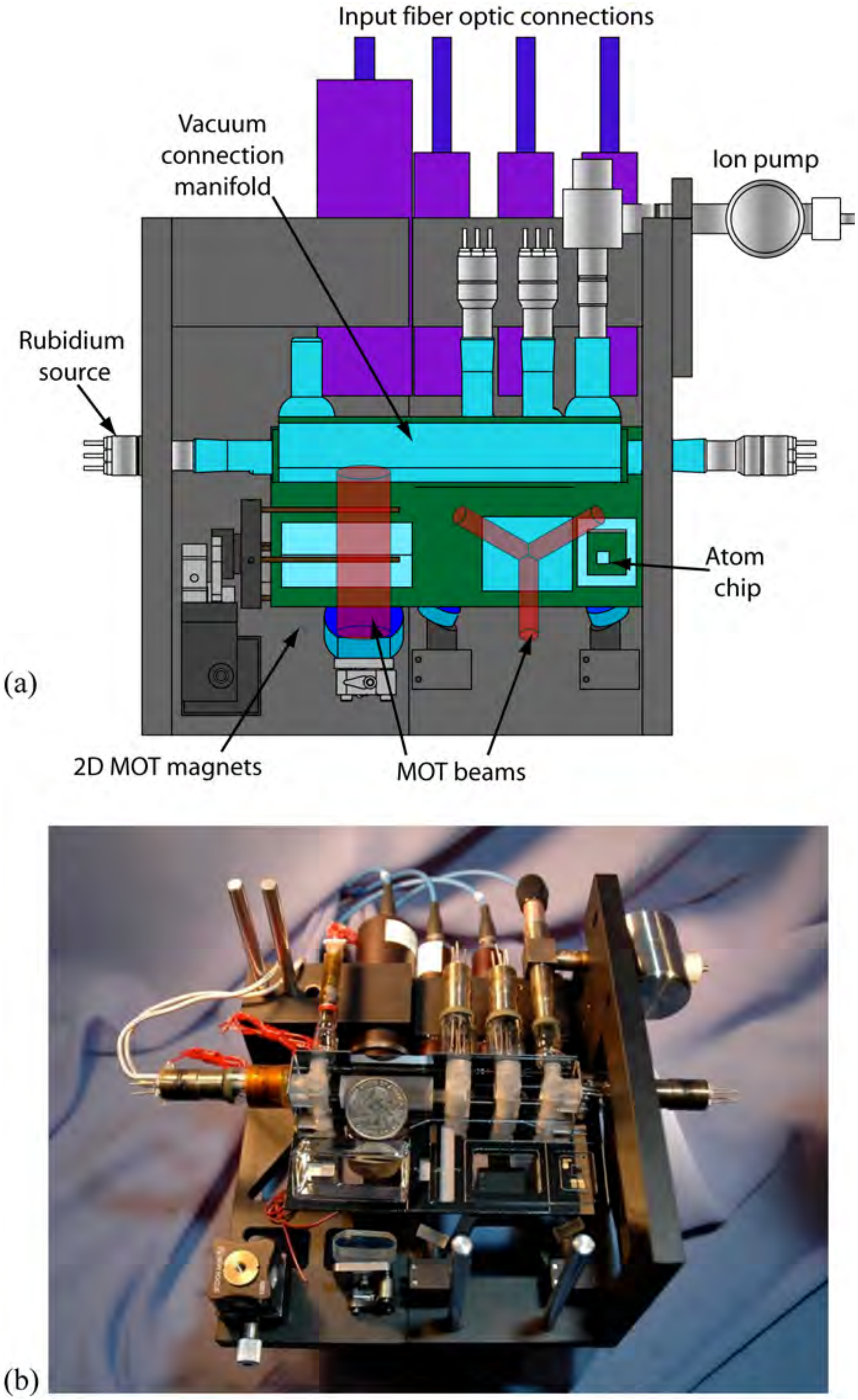

Figure 3.16: (Color). (a) Schematic drawing of the optics package for the channel cell. (b) Photograph of the channel cell optics package. The top optics have been removed to show the cell in place. Note the quarter in place for scale.

the 2D(+) MOT push beam. The second stage supports the optics for the 2D MOT. Light for the 2D MOT is brought in on a single fiber which is collimated to a 7 mm beam diameter. A small amount of light is siphoned off for the push beam, and the rest passes through a cylindrical telescope which expands the beam to a 20 mm waist in the vertical direction. The light is split with a plate beam splitter and then each beam is passed through a quarter wave plate and the cell. The beams are retro-reflected with a quarter wave plate laminated to a mirror. The third stage, shown with the double MOT cell in fig. 3.17(b), holds the vacuum chamber and the optics for the optical pumping beam. The top stage, shown in fig. 3.17(c) holds the optics for the 6 beam MOT and the imaging beam, as well as holding the imaging camera. The majority of the 6 beam MOT optics are held beneath the stage, leaving the top stage mostly open for additional optics to be added to the experiment. Light is brought into the 6 beam MOT stage with a fiber and then colimated to a 15 mm beam waist. The light is split into three paths before being steered into the MOT. The horizontal beam has only one steering mirror, which constrains the alignment of the MOT to a fixed distance above the stage. It is still possible to perfectly align the beams, as the other two beams have two mirror and can be aligned to overlap with the horizontal beam.

The purpose of the rail system is twofold: Having the optics on separate stages decouples the different parts of the optical system, making the two MOTs completely independent. It would be possible to switch the operation of the system to a mirror MOT, for example, by replacing only the top stage with a new design. Second, the freedom to adjust the beam height makes it very easy to quickly compensate for slight variations in the cell geometry which occur due to the glass blowing and polishing processes in the cell fabrication. This significantly decreases the amount of time needed to change cells. We have loaded atoms into a chip trap in a few as four hours after putting a new cell into the package. A photograph of the full assembly is shown in fig. 3.18.

3.4 Laser systems

As with the opto-mechanics surrounding the chamber, most laser systems for atomic physics experiments are built from commercially available components mounted to a standard optics plat-

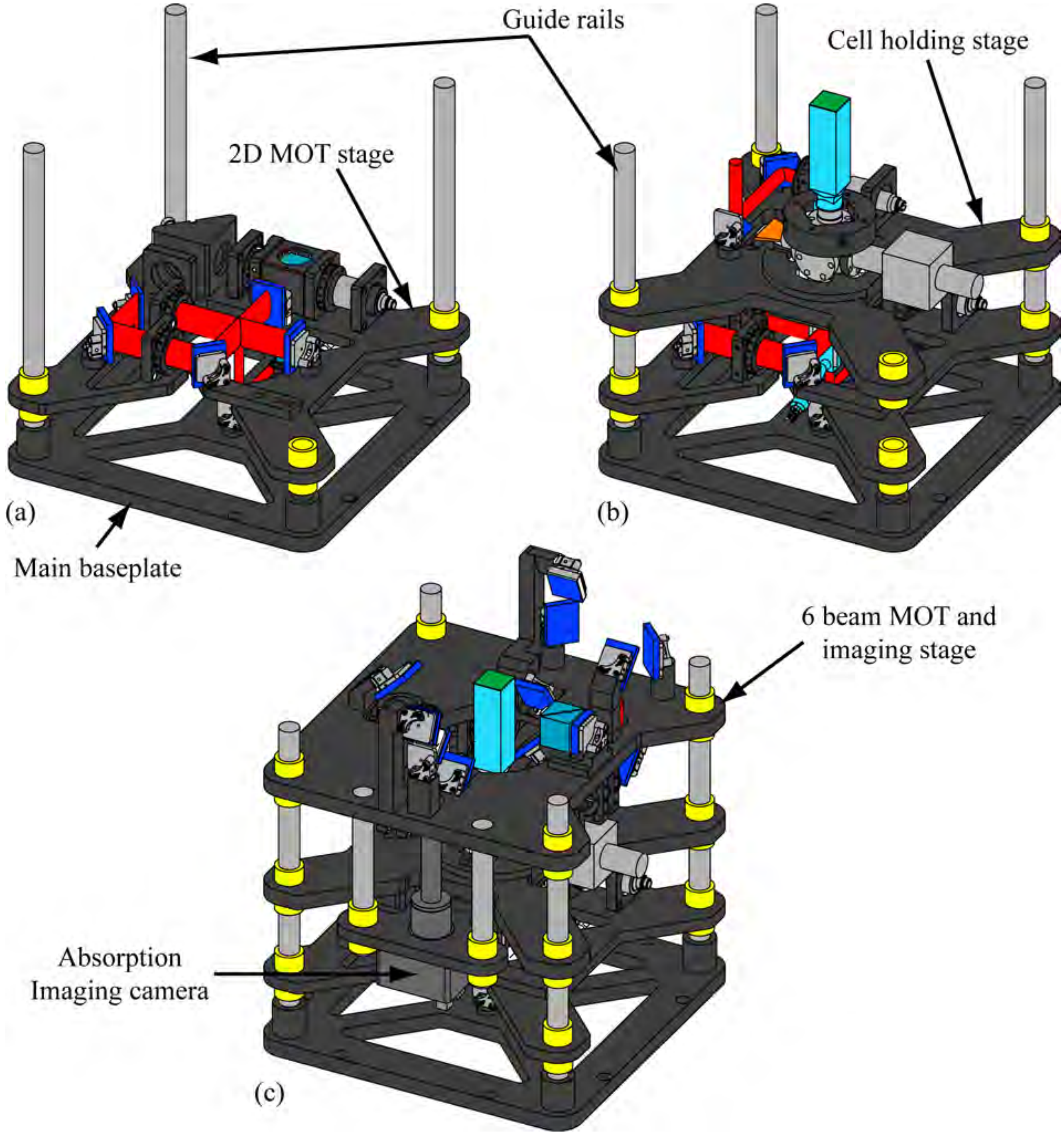

Figure 3.17: (Color). Schematic picture of physics package showing (a) the 2D MOT optics, (b) the cell holding stage, and (c) the full assembly.

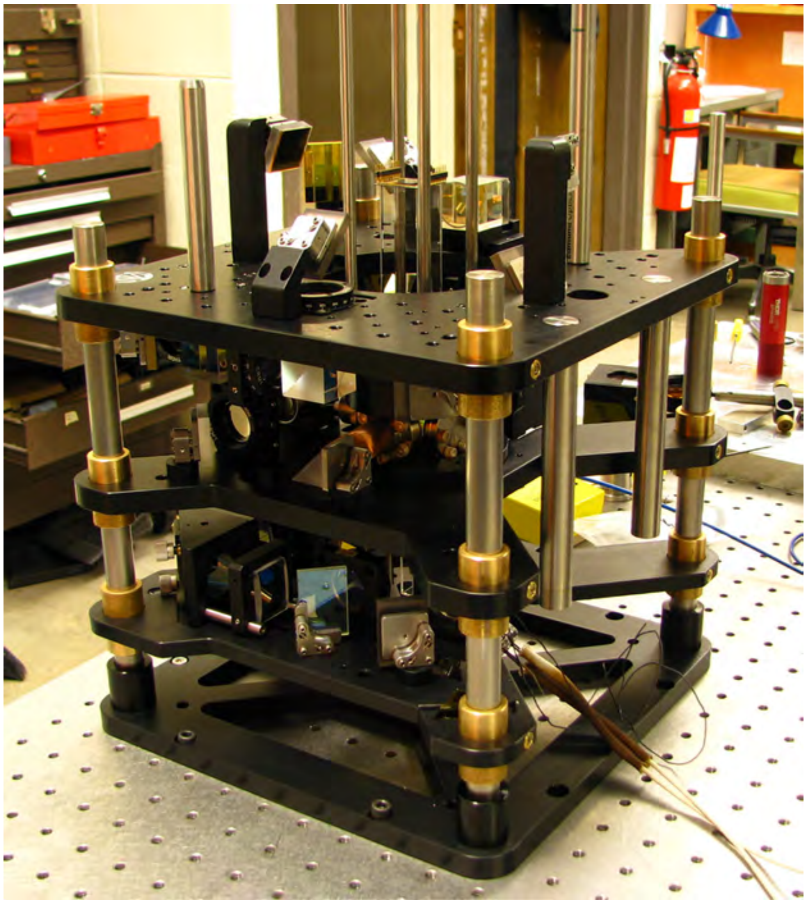

Figure 3.18: (Color). Picture of physics package

form. An example of such a system is shown in fig. 3.19. The only goal of the laser system is to supply the experiment with the correct amount of laser light of the correct frequency at the correct time. To that end all of the components necessary for integration remain the same: the system needs laser sources, optical isolation for the sources, frequency stabilization of the laser light to an absolute reference, shuttering of the beams, and a way to deliver the light to the experiment.

Figure 3.19: (Color). Typical Laser system

We have built an integrated laser system to replace the conventional approach for the portable system. A block diagram of the system is shown in fig. 3.20. The portable system consists of five distributed-feedback laser diodes at 780 nm which are used for cooling, repumping, optical pumping, and imaging. Two of the lasers are locked to spectral lines in Rb vapor cells, and serve as masters for the cooling and repump transitions. Cooling and repump slave lasers are offset-locked from their respective master lasers by stabilizing the RF heterodyne beat between each master and slave. Voltage-controlled oscillators set the offset frequencies. A combined 7mW of light from the cooling and repump slave lasers (85% cooling, 15% repump) is coupled into a tapered amplifier (Sacher TEC-400). This output is split into two, yielding 70mW and 50mW of light for the 2D+ MOT and 3D MOT, respectively. The fifth laser is offset-locked to the cooling master and used for optical pumping and absorption imaging. All of the optical connections are made through fiberoptic cables connected through custom made evanescent wave fiber couplers (supplied by Canadian Instrumentation & Research Ltd.) The pump/probe laser requires fast shuttering with good optical isolation, which is acheived by splitting the into two fibers using a fiber-based electro-optic switch and passing each beam through a mechanical fiber MEMS shutter, developed in collaboration with Teledyne Scientific and Imaging, LLC. The portable laser system is shown in the upper left corner of fig. 3.21.

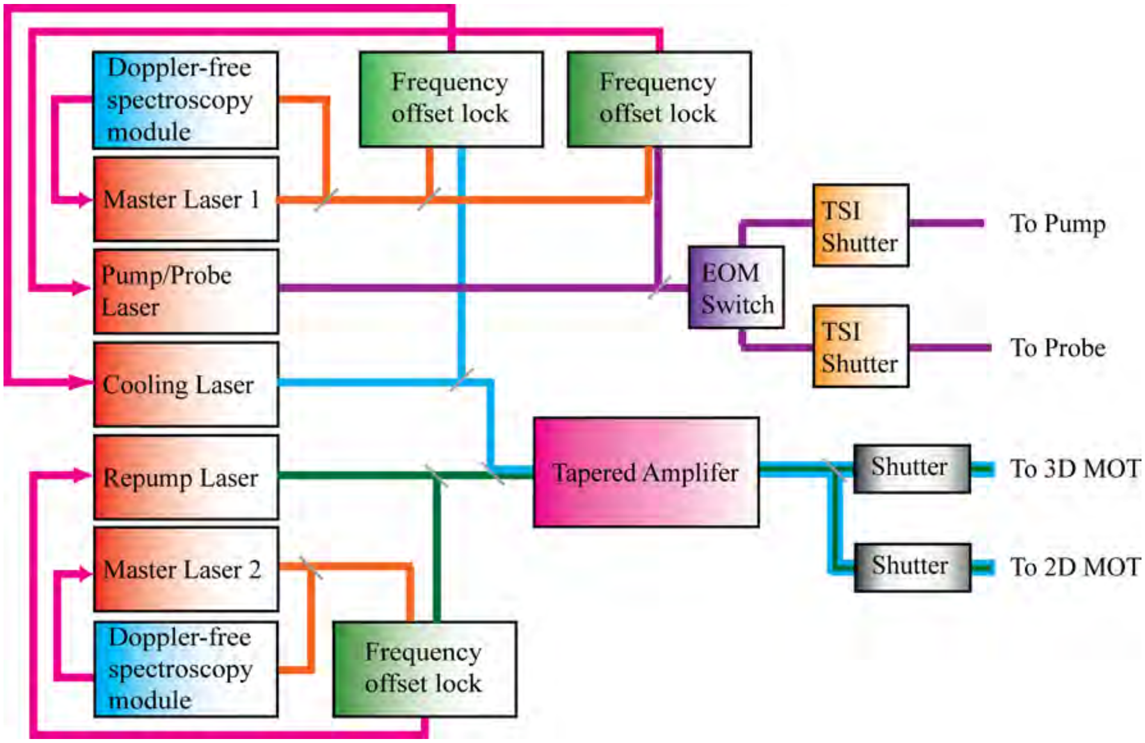

Figure 3.20: (Color). Schematic layout of laser system use for the portable BEC machine.

3.5 A portable BEC system

The double MOT optics package and the portable laser system have been integrated with a host of custom built electronics for computer control, power and feedback control for the lasers, and current servos for magnetic coils and the atom chip. These subsystems comprise a compact, movable, microchip-based BEC production system that occupies a volume of 0.4 m^3, and can produce BEC at a repetition rate as high as 0.3 Hz [71].

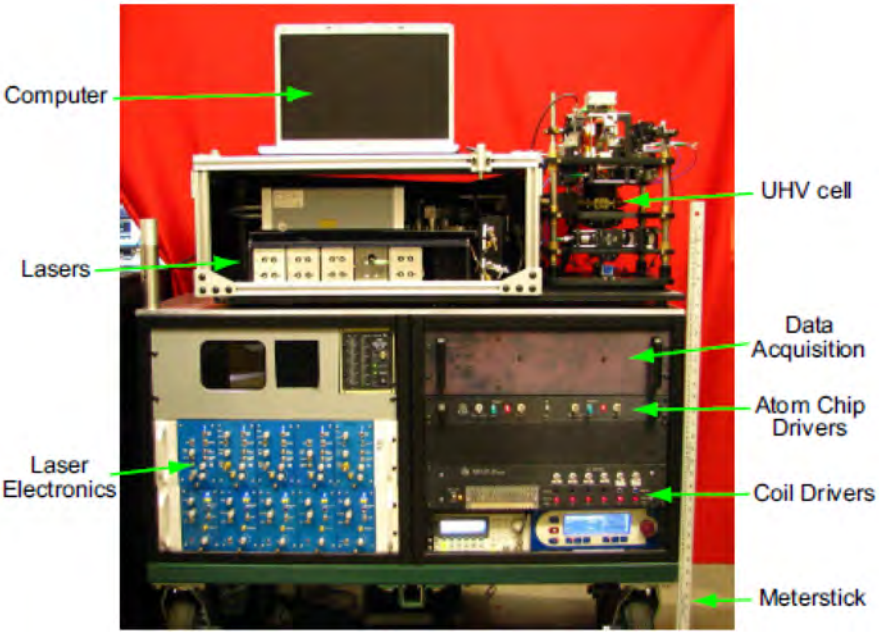

Figure 3.21: (Color). Picture of a compact, transportable system that produces and images BECs.

The BEC production procedure is as follows: The 3D MOT is filled with atoms from the 2D(+) MOT for 1 to 2 s to a total MOT number of 5×10^8 atoms. The atomic cloud is then spatially compressed by increasing the cooling slave laser detuning from -2.5Γ to -3.5Γ (where $\Gamma = 6.0$MHz is the natural linewidth of the cooling transition), blue-detuning the repump slave laser by 200 MHz, and increasing the magnetic field gradient from 10 G/cm to 30 G/cm. The atoms are further cooled with 4 to 7 ms of sub-Doppler polarization gradient cooling to temperatures below 20 μK. Circularly polarized light optically pumps the atoms into the $|F = 2, m_F = 2\rangle$ ground state.

The atoms are then transported vertically and loaded into the chip trap using an external Z-coil placed directly above the atom chip as described in [23, 24]. The coil's windings form a "Z" configuration in the same sense as the "Z" pattern on the atom chip. In conjunction with external bias fields, the Z-coil creates a Ioffe-Pritchard trap that is well mode-matched to the chip-Z trap, permitting efficient, adiabatic transfer of the atoms from the Z wire to the atom chip trap. The atoms are trapped in a dimple trap, which will be described in chapter 4, centered 115 μm below the chip surface, with calculated trap frequencies of 6.7kHz×6.7kHz×610Hz. The dimple trap typically contains about 3×10^7 atoms, with a magnetic trap lifetime of 6.5 seconds.

Several stages of RF evaporative cooling reduce the cloud temperature below the transition point for BEC formation. The RF frequency is swept linearly in five stages, totaling 1.3 to 2.5 s in duration, with each stage cutting halfway into the remaining trap. To avoid excessive three-body losses, the trap is reduced after the first stage by adiabatically decreasing the magnetic bias fields; the reduced trap has calculated frequencies of 2.4kHz×2.3kHz×340Hz and the trap center is shifted to 170 μm below the chip surface.

After evaporation, the atomic cloud is prepared for imaging by again reducing the trap. This final trap has calculated frequencies of 1.2kHz×1.2kHz×200Hz and is centered 260 μm below the chip surface. The cloud is then dropped by turning off all magnetic fields. After a variable time-of-flight, a picture of the cloud is obtained via absorption imaging on a CCD camera (Basler A102f). The onset of condensation can be seen in the OD distributions of Fig. 3.22. In (a), the RF evaporative sweep stops at 90 kHz above the trap bottom, resulting in a cloud of 6.9×10^4 non-condensed atoms at a temperature of 1.92(6) μK. The beginning of condensation is shown in (b), where the RF sweep stops at 60 kHz above the trap bottom. The cloud of 5×10^4 atoms has a temperature of 1.58(8) μK, slightly above the calculated transition temperature of 1.1 μK. Here, the condensate is evident by the higher peak OD and smaller Gaussian wings. In (c), where the RF sweep stops at 30 kHz above the trap bottom, the lack of Gaussian wings indicates a nearly pure condensate of 1.9×10^4 atoms.

The portable system is meant to serve as a standardized platform for a variety of experiments that utilize ultracold matter. As a demonstration of the system's portability the cart was taken to Portland, Oregon where it was used to produce BEC at the 2010 March Meeting of the American Physical Society. To the best of our knowledge this is the first public demonstration of a Bose-Einstein Condensate, and the first Bose-Einstein condensate produced outside of a laboratory environment.

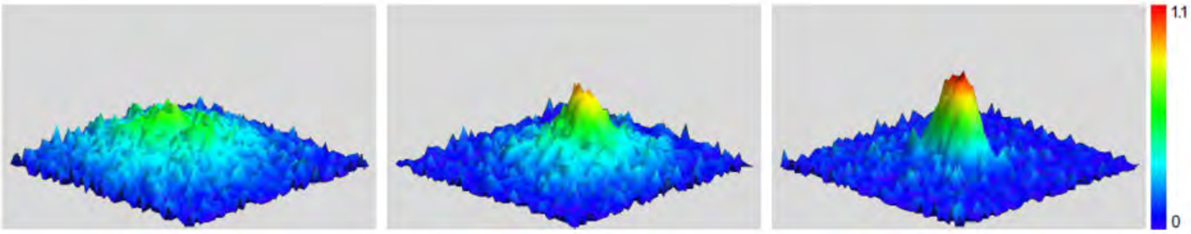

Figure 3.22: (Color). OD distributions demonstrating the onset of condensation: (a) a cloud of 6.9×10^4 non-condensed atoms at a temperature of 1.92(6) μK; (b) a partially condensed cloud of 5×10^4 atoms at 1.58(8) μK; (c) a nearly pure condensate of 1.9×10^4 atoms. Images were taken after 5 ms of free expansion.

Chapter 4

Atom chips

As discussed in chapter 2, cold atoms with a non-zero magnetic dipole moment can be captured magnetically at a field minimum. Conventional large scale BEC systems typically employ large coils or permanent magnets to generate magnetic fields for trapping atoms [37, 38]. These larger systems usually require hundreds of amperes to be run through the coils to generate field gradients that are large enough for evaporative cooling. If one wishes to make the system compact and portable it would be preferable to avoid such large currents, but it is still necessary to make a trap tight enough for evaporation. Atom chips are one approach to making tight traps with very low currents. Consider the magnetic field at a distance r from a single wire, carrying a current I:

$$B = \frac{\mu_0 I}{2\pi r} \propto \frac{I}{r}, \tag{4.1}$$

The gradient of the field from the wire is

$$B' = -\frac{\mu_0 I}{\pi r^2} \propto \frac{I}{r^2}, \tag{4.2}$$

If the goal is to achieve a large magnetic field gradient, then the current in the wire can be increased, or the distance to the wire can be decreased. Clearly, because of the $1/r^2$ term, the gradient increases much faster by decreasing r than by increasing I. Therefore all magnetic field generating sources should be moved as close to the atoms as possible. In the case of conventional macroscopic traps the distance from the coils to the atoms will be on the order of a few centimeters. Since magnetic coils are usually out of the vacuum that distance is generally limited by the size of the chamber. Larger field gradients can be achieved with lower currents by getting atoms very close to wires in vacuum [72, 73]. The logical extreme of this is to move the atoms as close as possible to a very small wire carrying a small amount of current. Now it is possible to take advantage of the tremendous amount of infrastructure that exists in the semiconductor community to fabricate tiny wires, and those tiny wires can be conveniently supported by a flat substrate, in the same way current carrying members on microchips are made. Not surprisingly, these chips used to trap atoms are called atom chips.

This chapter reviews some theory behind atom chips, followed by a discussion of the atom chip technologies we have developed in our group, including UHV vias.

4.1 Atom chip basics

In this section we will review the basics of atom chip traps, and take a close look at a few special cases that are important to the work in this thesis. Much of what follows in this section is covered very nicely in other places [74, 18, 23, 24].

4.1.1 The side guide

The simplest type trap that can be made with an atom chip is the side guide. Consider an infinite wire with current I flowing in the $\hat{x}$ direction in the presence of a uniform magnetic field $B_{ext} = (0, B_y, B_z)$, as show in fig. 4.1(a). The total field may be written as:

$$\vec{B} = \begin{pmatrix} 0 \\ B_y \\ B_z \end{pmatrix} + \frac{\mu_0 I}{2\pi} \begin{pmatrix} 0 \\ -\frac{z}{y^2+z^2} \\ \frac{y}{y^2+z^2} \end{pmatrix} \tag{4.3}$$

This configuration will result in a line of magnetic field zero parallel to the wire, shown as a red spot in fig. 4.1(b). This is not a good trap for experiments, as it is simply a waveguide, and a cold gas would expand to fill the length of the guide. However, it is useful to study because it can help to develop some intuition for the behavior of chip traps. To begin, let us consider the case where

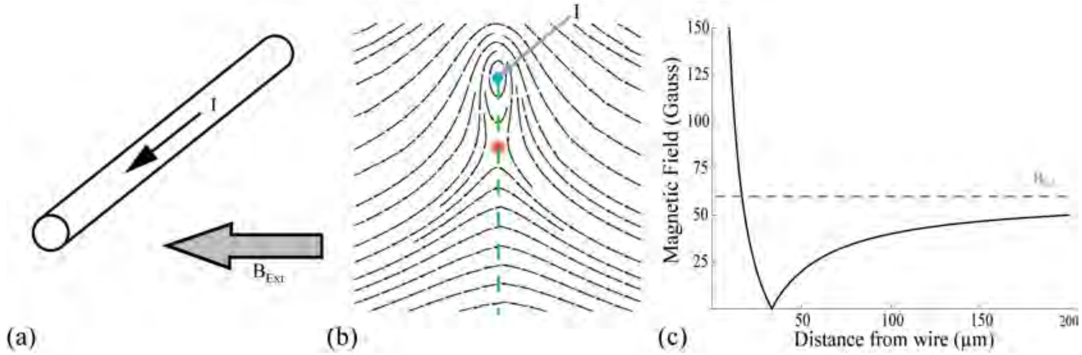

Figure 4.1: (Color). Magnetic field from a side guide. (a) The configuration of a current in the presence of an external bias field. (b) The magnetic field of the configuration shown in (a). The position of the field minimum, and therefore the position of the trap is shown in red. (c) Magnitude of the magnetic field along the green line in (b). The magnitude of the external bias field, B_{ext} is shown as a dashed line.

$B_z = 0$. Equation (4.3) then becomes

$$\vec{B} = \begin{pmatrix} 0 \\ B_y \\ 0 \end{pmatrix} + \frac{\mu_0 I}{2\pi} \begin{pmatrix} 0 \\ -\frac{1}{z^2} \\ \frac{y}{y^2+z^2} \end{pmatrix} \tag{4.4}$$

This bias field will cancel the field from the wire directly below the wire at a distance of

$$z_0 = \frac{\mu_0 I}{2\pi B_y} \tag{4.5}$$

This magnetic field will create a waveguide with a zero crossing, and the field will be roughly linear near the zero. While this guide will confine thermal atoms, it is not a good trap for a Bose-Einstein Condensate, as the cold atoms will fall out of the trap due to Majorana spin flips. One can plug the hole in the trap by applying a bias field along the axis of the guide. Including a bias field in the $\hat{x}$ direction, taking the field magnitude and expanding about $z = z_0$ will give

$$B = B_x + \frac{B_y^2}{2B_x z_0^2}\left(y^2 + (z - z_0)^2\right) = B_x + \frac{B_y^2}{2B_x z_0^2}\rho^2, \tag{4.6}$$

where we have defined the radial coordinate $\rho = \sqrt{y^2 + (z - z_0)^2}$. Plugging the hole makes the trap harmonic near the bottom, which means it can hold a Bose-Einstein Condensate in two dimensions. The harmonic trap can be characterized by a trap frequency ω, where

$$\omega = \sqrt{\frac{\mu B''}{m}}. \tag{4.7}$$

In this case the radial trap frequency is

$$\omega_\rho = \sqrt{\frac{\mu}{m B_x}}\frac{2\pi B_y^2}{\mu_0 I} \propto \frac{B_y^2}{\sqrt{B_x} I} \tag{4.8}$$

Note that adding in the x bias did not effect the trap position, as that component of the field was perpendicular to the field from the wire.

It is easy to see that the position of the trap can be rotated around the wire by including B_z term from equation (4.3). This is crucial for the window chip experiments that will be discussed in later chapters of this thesis. The addition of the z bias field moves the minimum position of the trap to

$$\begin{pmatrix} y_0 \\ z_0 \end{pmatrix} = \frac{\mu_0 I}{2\pi} \begin{pmatrix} \frac{-B_z}{B_y^2+B_z^2} \\ \frac{B_y}{B_y^2+B_z^2} \end{pmatrix}, \tag{4.9}$$

and the angle that the trap is moved from the z axis is

$$\theta = \arctan\left(\frac{B_z}{B_y}\right), \tag{4.10}$$

4.2 Chip traps

The side guide is not a three dimensional trap as is required for Bose-Einstein Condensation. Just as there must be at least a one dimensional current to create a two dimensional potential, there must be at least two dimensions of current flow for a three dimensional trap. There are many ways to achieve a three dimensional harmonic trap on an atom chip. In this section we will take a close look at four of the most common. Generally it is not practical to calculate trap attributes using analytic solutions, however it is very useful to understand how the trap parameters scale as a function of experimentally controlled parameters. The four most common chip traps are shown in fig. 4.2.

4.2.1 Z-wire traps

The simplest geometry for making a three dimensional trap is a z shaped wire, such as the one shown in figure 4.2a. The guide is capped on the ends by two half lengths of wire. As with the side guide, the bottom of the trap can be plugged by applying a bias field along the $\hat{x}$ direction, although the direction of the field must be chosen to add with the field from the legs of the Z. In many ways the Z wire is a very desirable trap for cold atoms experiments. The wire pattern for the trap is very simple, and it only takes a single current source for the atom chip. The trap is, however, highly anisotropic. The trap shape along the x-axis is mostly dependant on the length of the middle leg of the z. In some situations this may be desirable, but it can be detrimental to evaporative cooling. Additionally, there is a slight twist to the trap off the chip axis, as is visible in

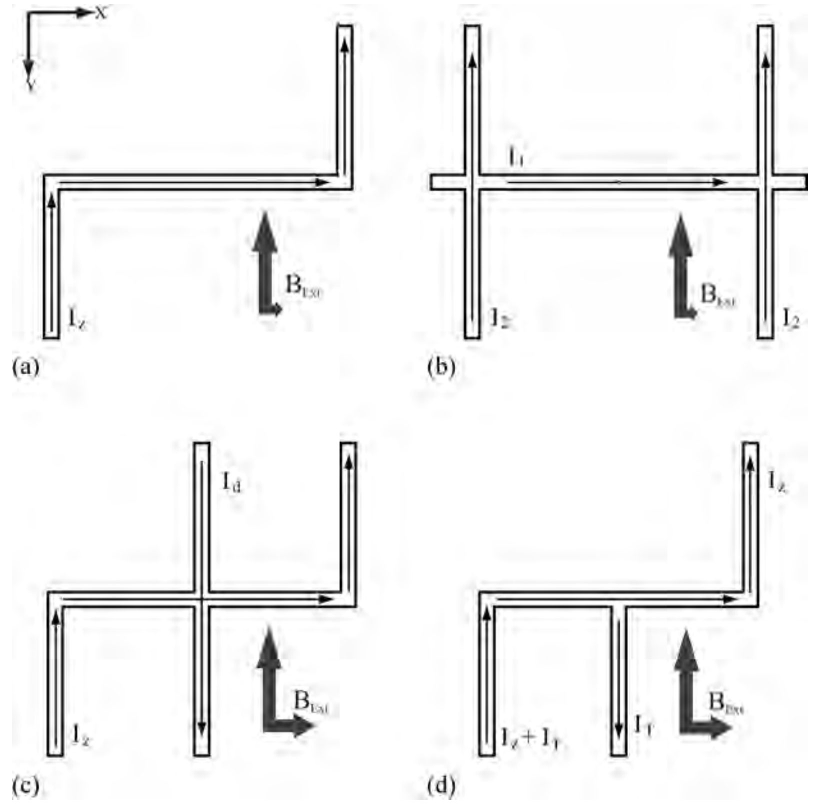

Figure 4.2: Four general types of chip traps used for BEC experiments (a) Z-wire trap. (b) H-wire trap. (c) Dimple trap. (d) T-wire trap.

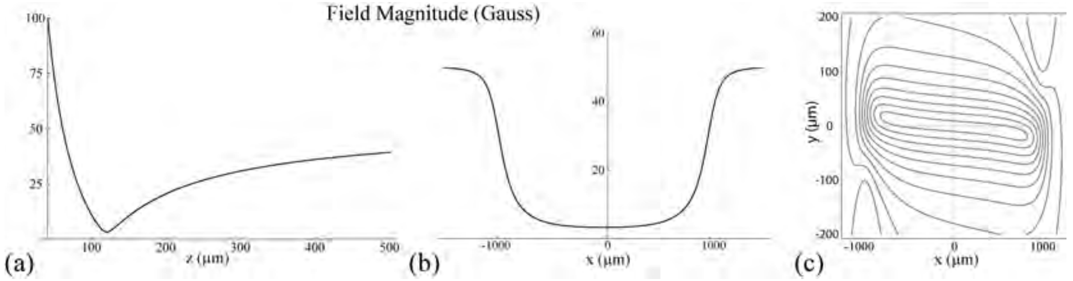

Figure 4.3: Magnetic field from a Z-wire trap with $L = 2mm$. (a) Field magnitude in the direction away from the chip. (b) Field magnitude along the direction of the middle leg of the Z-wire. (c) Contour plot of the magnetic field in the plane parallel to the chip at the position of the trap minimum.

figure 4.3c. This twist is caused by an asymmetry in the magnetic field from the legs of the Z wire. To understand this, consider the field from two half-infinite wires parallel to the $\hat{y}$ axis separated by a distance L, one carrying current from $y = -\infty$ to $y = 0$, and the other from $y = 0$ to $y = +\infty$. For simplicity, we will only consider the field at the position of the expected trap, $z = z_0$. The Z component of the magnetic field will be given by

$$\begin{aligned} B_{\hat{z}} &= \frac{\mu_0 I}{4\pi}\left(\frac{L/2+x}{(L/2+x)^2+z_0^2} - \frac{L/2-x}{(L/2-x)^2+z_0^2}\right) \\ &\approx \frac{\mu_0 I}{2\pi}\frac{(L/2)^2-z_0^2}{\left((L/2)^2+z_0^2\right)^2}x \end{aligned} \tag{4.11}$$

for $x \ll L$. Note that the field direction is linear in x giving the magnetic field the aforementioned asymmetry. We can calculate the displacement of the trap from the $y = 0$ line by

$$\begin{aligned} \Delta y &\approx z_0 \frac{B_z}{B_y} \\ &= \frac{\mu_0 I}{2\pi}\frac{(L/2)^2-z_0^2}{\left((L/2)^2+z_0^2\right)^2}\frac{z_0 x}{B_y} \\ &\approx \frac{\mu_0 I}{2\pi}\frac{z_0 x}{(L/2)^2 B_y} \end{aligned} \tag{4.12}$$

This corresponds to a twist angle of the trap from the axis of

$$\begin{aligned} \theta_{trap} &\cong \frac{\Delta y}{x} \\ &\cong \frac{mu_0 I}{2\pi}\frac{z_0}{(L/2)^2 B_y} \end{aligned} \tag{4.13}$$

Plugging in equation (4.5) for B_y we get

$$\theta_{trap} = \left(\frac{2z_0}{L}\right)^2, \tag{4.14}$$

If θ_{trap} is small, (i.e. $z_0 \ll L$) then we can treat the weak axis of the trap as being along the $\hat{x}$ axis. The trap frequencies at the bottom of the trap can be calculated by finding the second derivative of the field along that axis. The field is

$$\begin{aligned} B_{\hat{x}} &= -\frac{\mu_0 I}{4\pi}\left(\frac{z_0}{(L/2+x)^2+z_0^2} + \frac{z_0}{(L/2-x)^2+z_0^2}\right) \\ &\approx B_y \frac{z_0^2}{(L/2)^2+z_0^2} + B_y \frac{3z_0^2}{(L/2)^4}x^2, \end{aligned} \tag{4.15}$$

and the trap frequency will be

$$\omega_x = \sqrt{\frac{6\mu B_y}{m}} \frac{z_0}{(L/2)^2}, \tag{4.16}$$

For reasonable geometries and currents, such as $L \sim 1-2$ mm and $I \sim 2-3$ A, one can expect trap frequencies of the order $(\omega_\rho, \omega_x) \approx 2\pi$(1 kHz,10 Hz).

4.2.2 H-wire traps

A useful variation of the Z-wire trap is an H-wire trap. A picture of the geometry is shown in figure 4.2b. The H trap has some distinct advantages over the Z trap, namely it allows for independent control of the capping wires relative to the main guide. This allows for greater flexibility and control of both θ_{trap} and ω_x. Unfortunately this geometry is significantly more complicated to implement, as it requires at least 2 independently operating current sources, 3 if the wires are electrically connected as will be the case with a single layer chip.

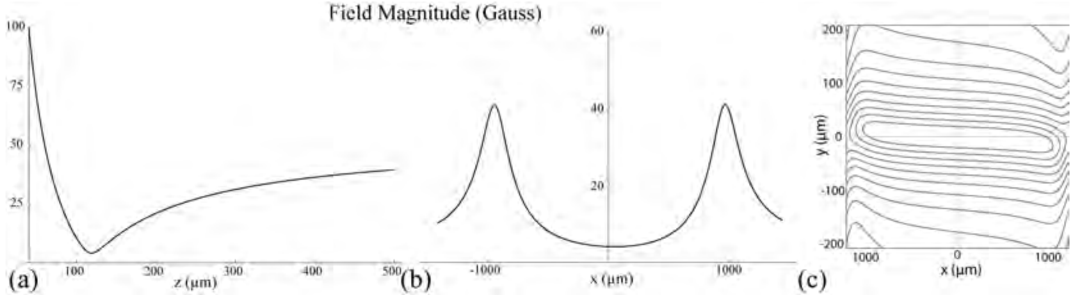

Figure 4.4: Magnetic field from an H-wire trap. Fields are calculated for $I_2 = 0.3I_1$. (a) Field magnitude in the direction away from the chip. (b) Field magnitude along the direction of the middle leg of the Z-wire. (c) Contour plot of the magnetic field in the plane parallel to the chip at the position of the trap minimum.

The twist in the H-trap can be calculated in the same way that the z wire twist was calculated, where the field from the Z legs is replaced with the field from two infinite wires. Assuming that there will be a different current in the H wires than the main guide, we can define a scale factor α such that $I_2 = I_1\alpha$. The twist may then be written as

$$\theta_{trap} = 2\alpha \left(\frac{2z_0}{L}\right)^2. \tag{4.17}$$

Similarly, the trap frequency along the x axis will be given by

$$\omega_x = \sqrt{\frac{12\alpha\mu B_y}{m}}\frac{z_0}{(L/2)^2}, \tag{4.18}$$

For the simple case of $\alpha = 1$, it is clear that the trap is twisted to twice the angle of the Z trap and has a trap frequency $\sqrt{2}$ greater. However, if there is independent control of I_2, the twist in the trap may be reduced at cost of $\sqrt{\alpha}$ to the axial trap frequency.

4.2.3 Dimple traps

While Z-traps and H-traps are useful in many situations, they both come with the disadvantage of being weak along the guide axis. This is due to the fact that those trap frequencies depend strongly on the geometry of the trap wires. This is detrimental to evaporative cooling, since the re-thermalization rate of atoms in the trap is proportional to the average trap frequency $\bar{\omega} = (\omega_1\omega_2\omega_3)^{1/3}$ [40], which is greatly decreased by the loose axial trap. For fast evaporative cooling it is desirable to find a trap that is more isotropic. A very nice solution to this problem is the dimple trap, shown in figure 4.2(c).

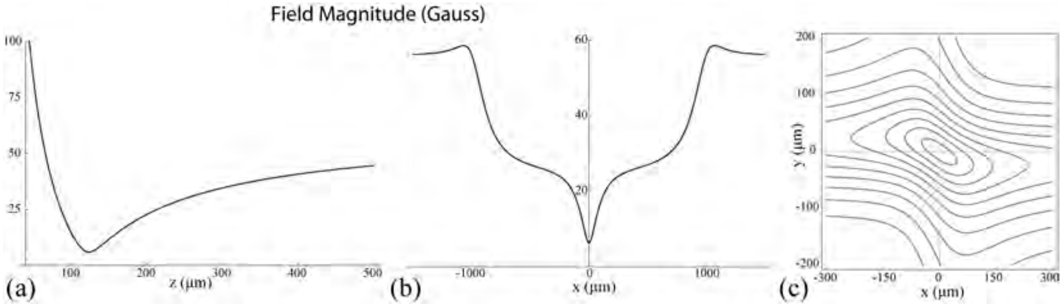

Figure 4.5: Magnetic field from a dimple trap. Fields are calculated for $I_z = 2.6I_d$. (a) Field magnitude in the direction away from the chip. (b) Field magnitude along the direction of the middle leg of the Z-wire. (c) Contour plot of the magnetic field in the plane parallel to the chip at the position of the trap minimum.

The schematic layout of figure 4.2(c) and the calculated fields shown in figure 4.5 include the combined trap of a z-wire and a dimple wire, since this is the trap geometry that we typically use. This choice gives a superposition of a Z-trap and a waveguide, resulting in the double trap shape show in figure 4.5b. In typical geometries a Bose-Einstein Condensate will only sit in the bottom of the dimple, but when hot atoms are loaded into the trap they will spill out of the dimple into the Z-trap. Without the Z confinement the atoms will fall out of the trap without colliding with the atoms in the dimple, and will be lost. We would like to understand the scaling of the dimple part of the trap. For that purpose it is appropriate to ignore the legs of the Z and study the field from two crossing wires carrying current I_z in the $\hat{x}$ direction and I_d in the$-\hat{y}$ direction. To cancel the field at the trap position it is now necessary to include a bias field in the $\hat{x}$ direction, B_x. The total field from the two wires and external bias fields is given by

$$\vec{B} = \begin{pmatrix} B_x \\ B_y \\ 0 \end{pmatrix} + \frac{\mu_0 I_z}{2\pi} \begin{pmatrix} 0 \\ -\frac{z}{y^2+z^2} \\ \frac{y}{y^2+z^2} \end{pmatrix} + \frac{\mu_0 I_d}{2\pi} \begin{pmatrix} \frac{-z}{x^2+z^2} \\ 0 \\ \frac{x}{x^2+z^2} \end{pmatrix} \tag{4.19}$$

In the limit of $I_d \ll I_z$ the radial trap is the same as it was for the Z and H traps. Expanding the x component of the field in a taylor series in x we find that

$$\begin{aligned} B_{\hat{x}} &\approx B_x - \frac{\mu_0 I_d}{2\pi z_0} + \frac{\mu_0 I_d}{2\pi z_0^3} x^2 \\ &= B_x - \frac{I_d}{I_z} B_y + \frac{\mu_0 I_d}{2\pi z_0^3} x^2 \end{aligned} \tag{4.20}$$

The trap frequency along that axis will be

$$\omega_x = \sqrt{\frac{\mu \mu_0 I_d}{2\pi M z_0^3}} \propto \sqrt{\frac{I_d}{z_0^3}}. \tag{4.21}$$

The z component will be minimized along the line

$$x = -\frac{I_z}{I_d} y, \tag{4.22}$$

which will correspond to an angular displacement of

$$\theta_{trap} \approx -\frac{I_z}{I_d}, \tag{4.23}$$

These calculations are only valid for our assumption of $I_d \ll I_z$. In most of our experiments it is more likely that $I_d \approx I_z/2$, in which case it is preferable to calculate trap frequencies and twist angles numerically.

4.2.4 T traps

In some situations, such as the gyroscope chip described in [24] or the window chip described later in this thesis, it is inconvenient to have current running across one side of the chip surface. One solution to this problem is the T wire trap as shown in fig. 4.2d. The T trap allows the experimenter to generate a trap which is still tight in the axial direction while leaving half of the chip surface open for other purposes. The trap behavior is very similar to that of the dimple trap, with the notable exception that the trap will be offset from the middle leg of the T wire, as the half of the main guide wire will be carrying less current. This tightens that half of the trap and pushes the field minimum to the other side of the T wire. Also, as the crossing wire stops halfway across the chip it only has half the contribution to the magnetic field of the dimple wire described in the previous section. The field calculated from the T wire trap is shown in fig. 4.6.

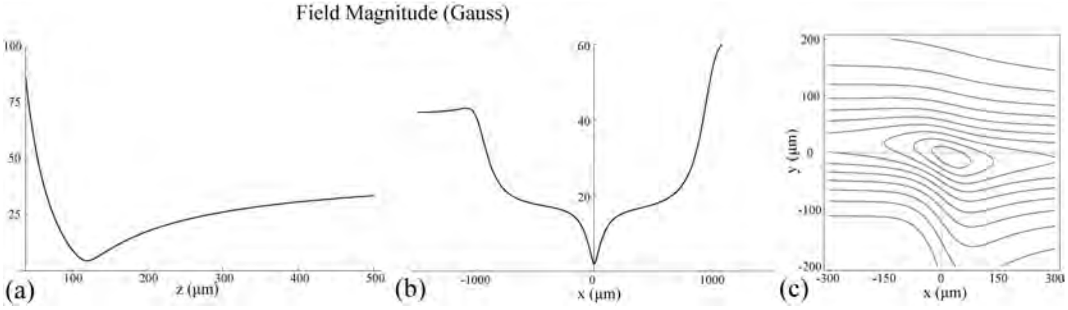

Figure 4.6: Magnetic field from a T-wire trap. Fields are calculated for $I_z = 3I_T$. (a) Field magnitude in the direction away from the chip. (b) Field magnitude along the direction of the middle leg of the Z-wire. (c) Contour plot of the magnetic field in the plane parallel to the chip at the position of the trap minimum.

We have found through numerical simulations that the wire geometry and correspondingly the current density in the T-wire trap has a significant impact on the final trap. Because of this trap parameters are usually calculated numerically where the current densities can be found using a finite element analysis method.

4.3 Atom chip fabrication processes and requirements

Atom chip fabrication relies heavily on the existing knowledge and infrastructure that has been developed by the semiconductor community. By many standards of that community atom chips are quite simple. However, the specific requirements of atom chips often leads to new technical difficulties in the fabrication process. An example microfabrication procedure for a single layer, single side atom chip is shown in figure 4.7. It is not the intent of this thesis to teach the reader how to make atom chips, but it is important to understand what goes into the fabrication process, and what the capabilities and limits of those processes are. To the end user of an atom chip there are a few important characteristics that will make up a good chip. They are outlined in table 4.1

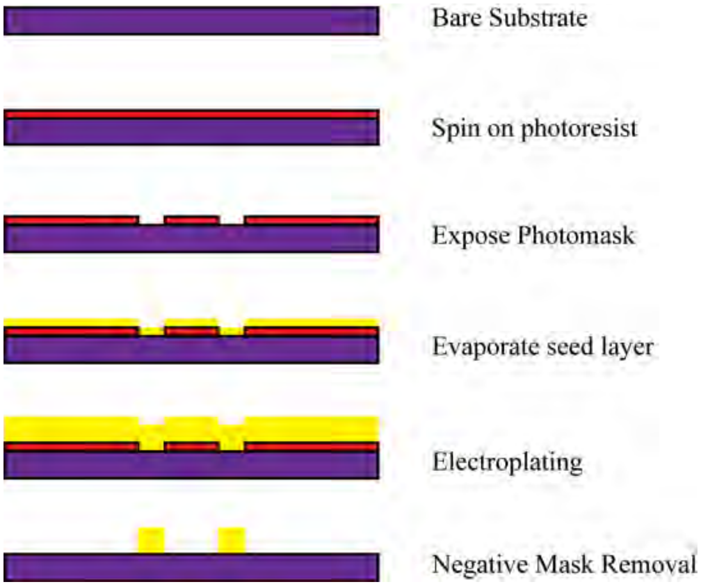

Figure 4.7: (Color). Atom Chip Fabrication flow chart.

We have used many fabrication techniques to achieve high quality atom chips. The choice of process depends on the desired wire geometry. For wire features larger than 25 μm we typically employ conventional lithography, such as the process described in [74]. Thin wires may be achieved by evaporation of thin films. Thicknesses of up to 5 μm have been achieved through direct evaporation [21], but it is expensive to deposit that much material and the thick layer tends to develop a lot of stress. For wire thicknesses of more than a few hundred nm we typically employ

Characteristic	Typical Values	Comments
Feature Size	100nm-1mm	The feature size dictates what the chip may be used for. A chip used for interferometry may have very wide traces, while a chip designed for tunneling will have very small wires.
Wire thickness	100nm - 10 μm	The wire thickness in conjunction with the width will determine the maximum current capacity of the trace. We have found that copper traces 100 μm wide and 10 μm thick can support 12 Amperes of current for short times [75].
Wire material	Copper, Gold, Silver	The metal choice will determine the resistivity of a given chip wire, as well as maximum current density that the trace will support, and thus the chip's maximum current capacity. Additionally, some atoms will interact with the metal on the atom chips. For example, we have observed that gold and rubidium form an alloy which can be detrimental to atom chip traps.
Surface Roughness	RMS $\sim$ 100 nm	Surface roughness, edge roughness and metal uniformity will all effect the path of the current through the wires, which will effect the final trap smoothness
Edge Roughness	10-100nm	See above
Metal Uniformity	??	Grain boundaries in the metal will also effect the current path through the wire. It is difficult to determine how strong an effect this is, or what acceptable limits are, although there has been some excellent work done to study this in Rod Folman's Group at Ben-Gurion University [76]
Substrate Quality	Flatness $< \lambda$, roughness $\sim$ .1-1nm	Substrate quality is not typically an issue for atom chips, as the semiconductor community has gone to great lengths to produce wafers with extremely well controlled surfaces
Temperature Range	120 - 400 °C	The atom chip must be able to survive the temperature cycles of assembly and vacuum processing
Vacuum compatibility		All of the materials used to fabricate the chip structure must be compatible with ultra-high vacuum conditions.

Table 4.1: Atom Chip Requirements

an electro-plating process to build up our features [77]. We have plated chip patterns of up to 20 μm thick, but we have found for most of our applications that 10 μm is sufficient.

Smaller features are achievable, but require more advanced fabrication techniques. For producing features in the range of 1 μm to 25 μm we have been successful using UV lithography [78]. If that resolution is not necessary for a given chip design the techniques are best avoided, as the photo-masks are significantly more expensive and the process is more difficult, resulting in lower yields in the fabrication process. To achieve still smaller features one must use electron-beam lithography [79, 80], which in principle can have a minimum resolution of tens of nm. We have fabricated chip wires that are as small as 200 nm wide and 100 nm thick. That fabrication will be discussed in greater depth in the next chapter.

4.4 Early atom chip efforts

Early efforts of producing BEC chips in our group employed aluminum nitride (AlN) substrates with copper traces. These atom chips were attached to the end of a quartz flourimeter cell with a low vapor pressure epoxy (EpoTek 353-ND), making the atom chip one wall of the vacuum chamber [19]. Using the atom chip to seal the vacuum chamber simplifies the electrical connections to the atom chip, reduces the overall size of the vacuum chamber, and it makes it possible to get external instruments very close to the atomic sample. The benefits of this last feature will become very apparent in the later chapters of this thesis.

While the group was successful in producing BEC with these early atom chips they did have a host of problems. As was discussed in the previous chapter the single chamber design led to problems with striking a good balance of Rubidium pressure with vacuum quality. The epoxy used to seal the atom chip limited the processing temperature, which in turn limited the quality of the vacuum that could be achieved. AlN is also not an ideal substrate choice. The thermal conductivity of the material is quite high, which is advantageous for heat sinking the atom chip and it is an excellent electrical insulator, however, it is difficult to fabricate AlN substrates that are particularly flat or smooth. Typical surface roughnesses are ∼100 nm, which effects the lithography

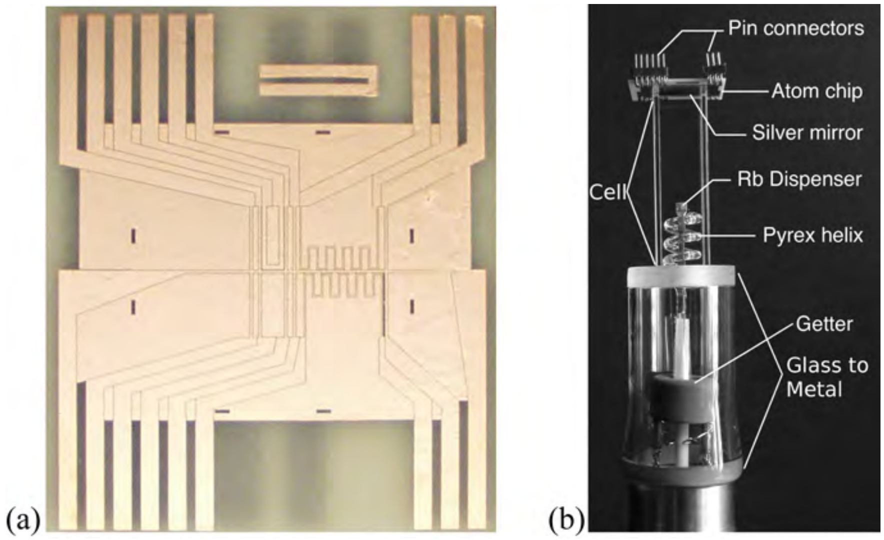

Figure 4.8: (Color). (a) An early generation atom chip with an aluminum nitride substrate. (b) Aluminum nitride atom chip attached to the flourimeter cell.

process and ultimately limits the achievable smoothness of the wire and thus the magnetic potential. Additionally the coefficient of thermal expansion (CTE) of aluminium nitride (4.5 μm/m-k)is poorly matched to quartz glass (0.4 μm/m-K). Quartz was chosen as the material for the glass cell because of its excellent optical quality and high transmission in the ultraviolet, which is desirable for single chamber experiments that wish to use Light Induced Atomic Desporption to modulate the vapor pressure of the alkali gas. Unfortunately the CTE mismatch between the chip and the cell led to problems with the epoxy joint breaking during vacuum processing.

Fortunately, there is not a large number of substrate materials that are appropriate for atom chips. Sapphire is an attractive option because it can be made very flat, and in principle the entire vacuum chamber could be made from sapphire. Also, since sapphire is transparent in the near infrared it would be possible to image through the atom chip. Unfortunately sapphire has a relatively low thermal conductivity, which significantly decreases the potential current capacity of traces on the surface. Diamond in many ways would be ideal as it is transparent, has a tremendous thermal conductivity, has a CTE very close to fused quartz, and the high refractive index could be very advantageous to imaging applications. Diamond wafers, however, are not currently available, and would probably be prohibitively expensive. Silicon is another popular choice. Although it has a lower thermal conductivity than AlN, silicon wafers can be made almost atomically flat, and there is a tremendous amount of infrastructure surrounding using passivated silicon for micro-electronics. Armed with this information we fabricated some silicon atom chips. As was discussed in chapter 3 silicon also has the useful property of being a material which can be anodically bonded to Pyrex glass. In the case of atom chips anodic bonding can be used to fuse the chip to the vacuum chamber. Also, the bond layer has virtually no thickness which makes it possible to shine a laser beam very close to the level of the atom chip.

Although the switch to silicon chips and replacing epoxy with anodic bonding solves a large number of issues associated with the assembly and vacuum processing, it introduces its own problem. It is necessary to get current from the power supply, which is typically outside of the vacuum chamber for practical reasons, to the wire traces on the surface of the atom chip. To solve this problem we had to develop electrical feedthroughs, or “vias” that would carry current through the atom chip.

4.5 UHV vias

All chip based experiments must carry current into the vacuum chamber. In most chip trap experiments this is done with electrical feedthroughs brazed to conflat flanges that are connected to the atom chip inside the vacuum. Using the atom chip as a wall of the vacuum chamber bypasses the bulky conventional feedthroughs, but it does not eliminate the problem. When the chips were being expoxied to the end of the vacuum cell it was possible to use the epoxy to seal the feedthrough joint, but if the atom chip is sealed to the cell by anodic bonding then it is necessary for the current to pass through the atom chip itself. This is shown schematically in fig. 4.9.

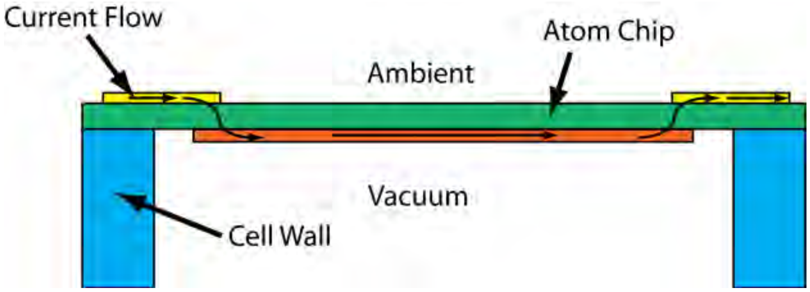

Figure 4.9: (Color). Schematic diagram of the need for UHV compatible electrical vias for atom chips.

Through-wafer interconnect technology has been studied extensively for microelectronics and MEMS applications (see for example [81, 82]), but there are very few processes that have been developed that are compatible with our requirements for current capacity, robustness at high temperatures and UHV hermiticity. Our group has studied three of the available technologies: Potassium Hydroxide KOH etching of silicon combined with an electroplating process, deep reactive ion etching(DRIE) combined with an electroplating process, and compound substrates.

4.5.1 KOH vias

KOH will etch a very clean hole through crystalline silicon along the crystal axis, leaving a pyramidal hole in the wafer with sidewalls at an angle of 54.74° from the vertical. This process was used to fabricate through chip vias in a collaboration with Victor Bright's group by Ho-Chiao Chuang in the mechanical engineering department at the University of Colorado [83].

To fabricate UHV vias with a KOH process we start with a silicon wafer with a low stress silicon nitride (SiN) layer on each side of the wafer. Small holes in the SiN layer are etched in the position of the vias with a reactive ion etcher, and the wafer is etched through to the other side with KOH. The etching process leaves a SiN membrane on the far side of the wafer undamaged. The hole is then electroplated with a layer of copper, and the SiN membrane can be removed, leaving the copper exposed to the back side of the chip. The chip can then be plated with wire traces using normal lithographic processes. The via can be seen in cross section in fig. 4.10.

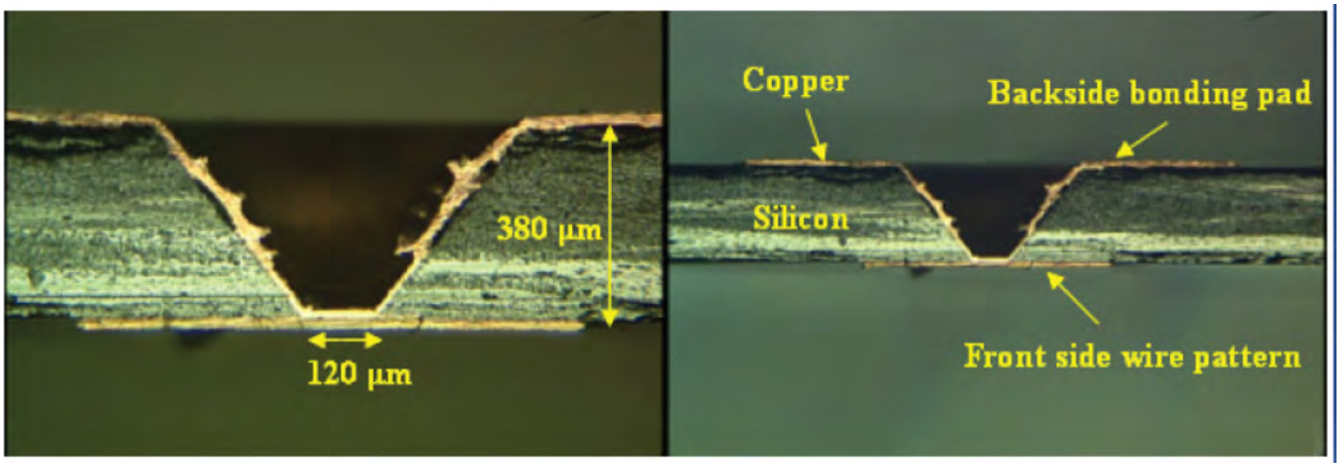

Figure 4.10: (Color). Cross section view of the KOH via fabricated at JILA and the University of Colorado

These vias were quite successful, in that the process had high yield (∼ 97%), and the vias could carry up to 12A. However, the technology is limited in its approach, as the etching angle of the KOH process limits the density of vias that is possible through the atom chip. This is particularly detrimental to atom chips requiring a large number of wires, such as the gyroscope chip described in [24].

4.5.2 DRIE vias

The second via technology we explored, deep reactive ion etching (DRIE) combined with an electroplating process, was pursued through a subcontract to Teledyne Scientific and Imaging (LLC). The details of that process are proprietary, but the approach is similar to that of [84]. The advantage of the DRIE process is that the through holes in the silicon can be made very straight, which allows for greater via density on the wafer. The via is shown schematically in fig. 4.11a, and fig. 4.11b shows an atom chip fabricated with the Teledyne process.

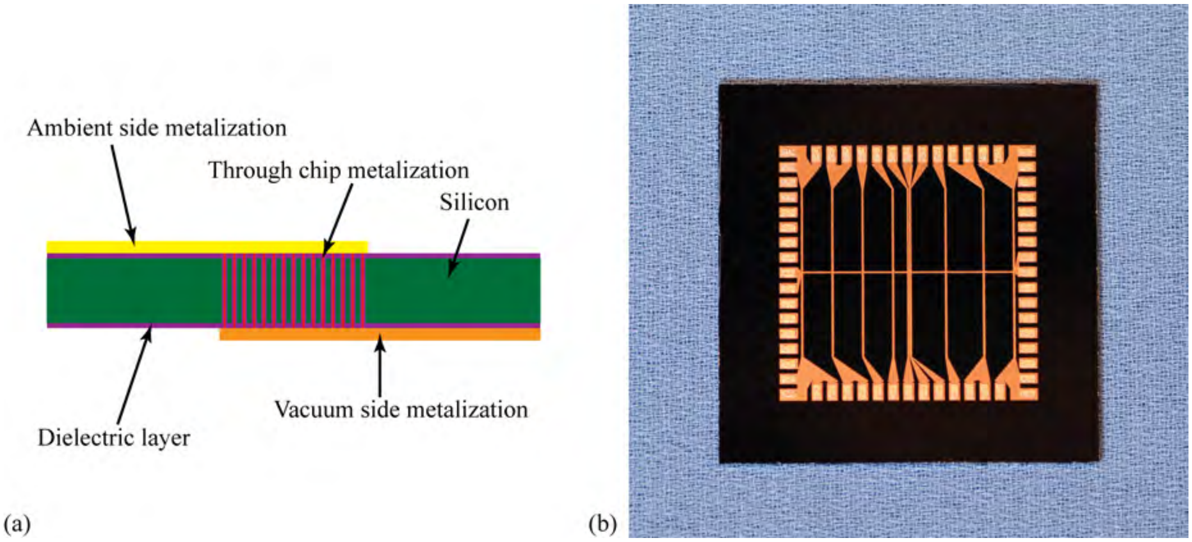

Figure 4.11: (Color). (a) Schematic of the DRIE vias fabricated at Teledyne Scientific. (b) Atom chip with DRIE vias.

We were able to successfully use atom chips made with the DRIE vias, but the yield in the process was very low due to problems with the electroplating process, and the chips fabricated with that technology were prone to leaks through the vias.

4.5.3 Compound substrate vias

The third technology explored employed a compound substrate, where the wafer was made of co-planer regions of highly doped silicon and glass. The via in this technology is the silicon itself, and the electrical connection to the vias is made by ohmic contact to the silicon from both sides. This is shown schematically in fig. 4.12a. To prevent shorting to the silicon it is necessary to cover the silicon wafer with a dielectric insulating layer, but in regions where it is desirable to have the metallization make electrical contact to the silicon the dielectric is removed. The glass layer serves as an isolation ring around the silicon via to prevent electrical connection to other vias or to the rest of the substrate. The compound substrate wafer is fabricated by a external vendor to our specifications then it goes through an intensive metallization process before it is diced into atom chips. An example of such a wafer is shown in fig. 4.12b, and a chip produced with this technology is shown in fig. 4.12c.

This technology solved many of the issues involved with the other two via approaches: the wafers rarely have leaks in them, and the process allows for high density vias, such as the ones necessary for the gyroscope chip. This technology was completely compatible with our existing techniques, and was significantly more robust, resulting in less expensive atom chips with dramatically improved yield. The use of glass regions of these wafers as through-chip optical windows will be described in the next chapter.

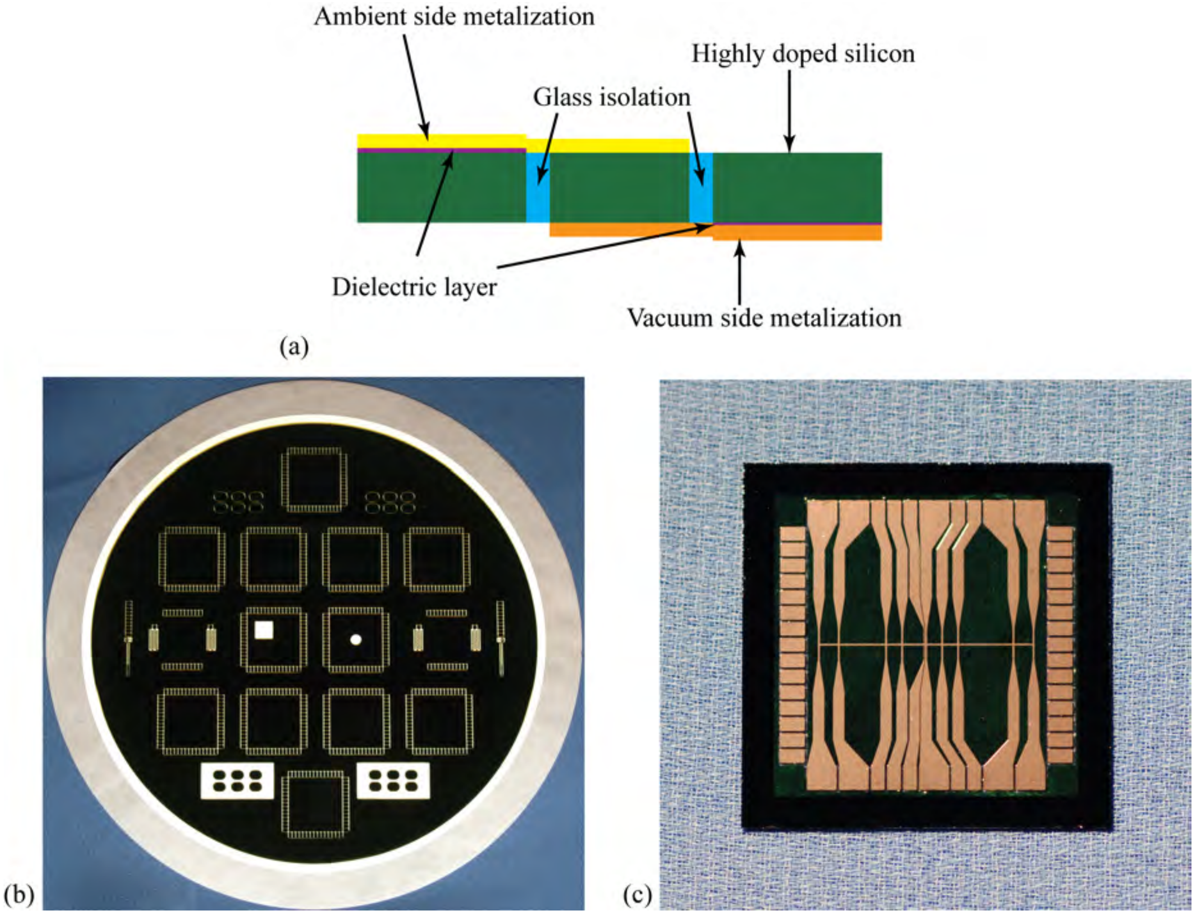

Figure 4.12: (Color). (a) Schematic diagram of compound substrate via. (b) Full compound substrate via. Areas that appear as white inside of the perimeter of the wafer are glass. (c) Atom chip with compound substrate vias.

Chapter 5

Atom chips for atomtronics

In the previous chapter we laid the framework for our atom chip technology. The specific design of the wire patterns on the chip depends on the intended experiments. So far we have only considered chip structures that are limited to magnetic fields from wire traces with roughly uniform feature sizes across the chip in a single plane. This chapter will cover our work on two approaches to making atom chips that would make it possible to generate potentials appropriate for atomtronics experiments. First we will present the design and fabrication of chips with sub micrometer features to enable control over purely magnetic potentials at short range, and describe the technical challenges presented by those chips. Second we will present window chips that will make it possible to generate atomtronics potentials with a hybrid trap of optical and magnetic fields.

5.1 Nano-chips for tunneling experiments

As discussed in chapter 2 the potential needed to realize a transistor is technically demanding. To achieve experimentally realistic tunneling rates it is necessary to generate potentials with feature sizes of about 1 μm. With a static magnetic field this requires that the size of the field producing element also be about 1 μm or less and that the atoms be within that same distance of the wire. Most atom chip experiments employ wire patterns with characteristic feature sizes of $\sim 100\,\mu$m, and pattern sizes of ~ 1 mm. These features are typically appropriate for production of a Bose-Einstein Condensate, but limits the physics that may be studied with that chip. If one wishes to produce a potential where the field from separate multiple conductors can be resolved the atom-chip distance must be on the same order of the spacing of the wires. This can be seen clearly in figure 5.1. Far from the chip surface, as shown in fig. 5.1(a), the magnetic fields from the wires combine in a such a way that they appear to be generated from a single conductor. As the atoms are moved closer to the atom chip by decreasing the current in the wires or increasing the external bias field, as shown in fig. 5.1(b), in becomes possible to distinguish the field from individual wires and to generate multiple traps.

At these small atom-wire spacings one must consider the effects of the finite width of the wire. If the atoms are too close to the wire the trap bottom will spread out over the width of the wire. This can be understood by considering the magnetic field from a wire of finite width w carrying current I [18]:

$$Bz = \frac{\mu_0 I}{\pi w} \cot^{-1}\left(\frac{2z}{w}\right). \tag{5.1}$$

in the limit of $z \ll w$ the field is roughly unform with

$$B = \frac{\mu_0 I}{2w}. \tag{5.2}$$

Away from the position directly above the center of the trace the field will fall away roughly as the expected $1/r$, but this wire width will limit how tight the confinement of the trap can be.

It is important to mention that this assessment is only valid for the case of static magnetic fields. It is possible to generate potentials for the atoms that have smaller features using RF dressed potentials [36]. The RF potential couples the atom to the anti-trapped state, which provides a convenient way to make a two well potential from a single well [55, 85]. This approach does not help much for making an atom transistor potential. The resulting traps in the dressed state will never be tighter than the original potential, and it is difficult to make the asymmetric trap geometries that are desirable for the atom transistor.

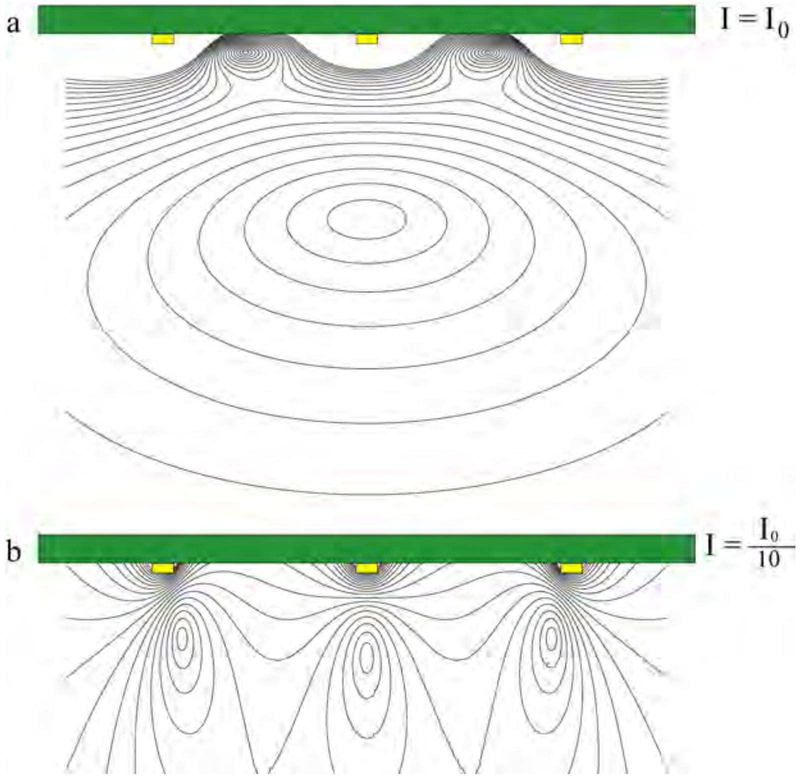

Figure 5.1: (Color). Chip traps generated by multiple guide wires. (a) Far from the atom chip the magnetic fields from the wires adds constructively, and the field to appears to be from a single conductor. (b) Close to the chip surface ($z_0 < d$) the individual conductors are visible and the trap splits into multiple traps. and the substrate shown in green.

5.1.1 Surface effects: Casimir-Polder forces on neutral atoms

With a multiple well potential generated from DC currents on a chip the atoms must be on the order of $1\mu m$ from the chip surface to achieve realistic tunneling rates. At that range the effects of the surface on the atoms cannot be ignored. Specifically we must take into account the attractive Casimir-Polder force on the atoms [86, 87, 88, 89]. The Casimir-Polder potential on an atom near a surface is given by

$$U_{cp} = -\phi(\varepsilon)\frac{3\hbar c\alpha}{32\pi^2\epsilon_0}\frac{1}{d^4} = -\frac{C_4}{d^4}, \tag{5.3}$$

where α is the polarizability of the atom (5.25×10^{-39} F m^2 for Rubidium), and $\phi(\varepsilon)$ is a dimensionless retardation constant of order 1 that is calculated for the surface of interest [90] ($\phi = 0.77$ for SiO_2). At very short ranges this potential will dominate the field from the wire, as shown in fig. 5.2. It is interesting to note that even at atom-surface distances as small as 500 nm the Casimir force will not eliminate the trap, and naively we might think that the surface interaction will not be a problem for the experiment. However, the barrier height reduction between the trap and the surface can be enough that there will be significant tunneling of atoms into the surface. Lin et. al. [89] showed significant losses from a condensate to the surface at distances as large as 2μm.

This is not necessarily a show stopper for the experiment. The atoms need to be close to the wires, but not close to the surface. One can remove the surface from underneath the wire leaving a bridge, as shown in fig. 5.3. This relief in the substrate should mitigate the effects of the Casimir-Polder force provided that the wire is thin compared to the atom-wire distance [91]. The bridging wires will generate a very tight trap in the axes perpendicular to the current flow, but the atoms must be held in three dimensions. To confine the atoms in the direction parallel to the bridge currents the chip can be made with a second layer of wires embedded in the silicon underneath the bridges. We designed the chip to have three embedded wires, which allows for trapping atoms in either an H trap or a dimple trap as discussed in chapter 4.

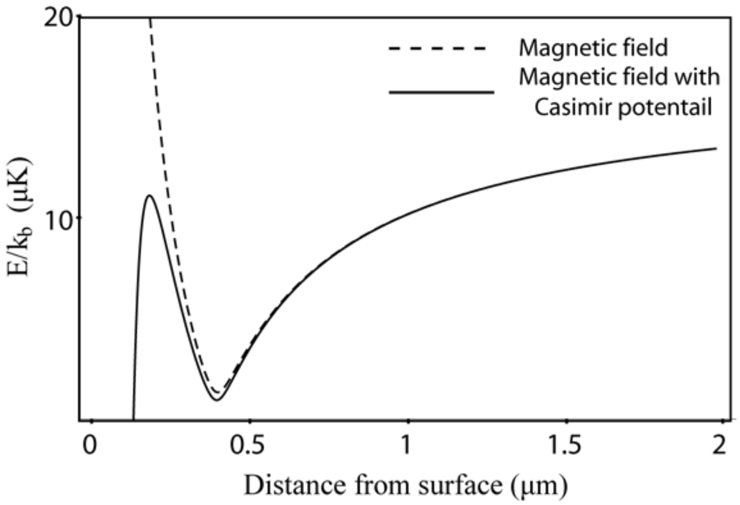

Figure 5.2: Magnetic potential and the combined Casimir-Polder and magnetic potential. Atoms trapped in the magnetic well will tunnel through the barrier separating them from surface and be lost from the trap.

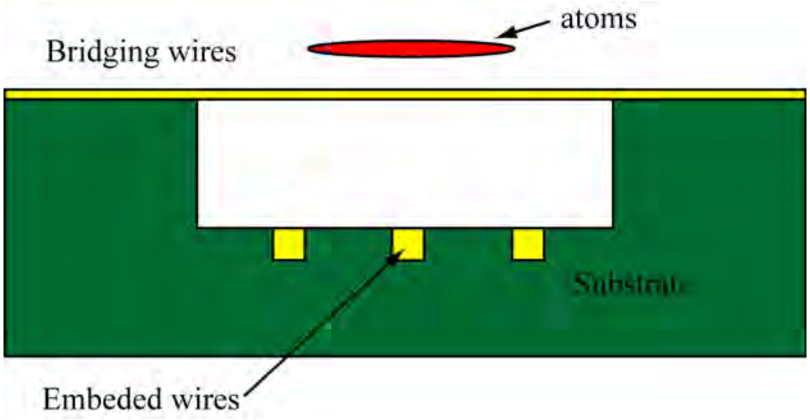

Figure 5.3: (Color). Bridging wires to mitigate the effects of the Casimir-Polder force. By keeping the atoms close to the wire but far from the surface the effects of the Casimir-Polder force on the atoms can be mitigated.

5.1.2 Test chip fabrication

To test the feasibility of the multi-layer transistor chip concept we worked in collaboration with Victor Bright and Ho-Chiao Chuang in the mechanical engineering department at the University of Colorado. The test chip would allow us to generate a two well potential that would be appropriate for tunneling experiments. The focus region of the chip consists of a pair of ~ 100 nm wide wires bridging a gap in the silicon 10 μm wide and 2 μm. At the bottom of the trench are three 3 μm wide and 2 μm deep wires embedded into the silicon. The chip is shown schematically in fig. 5.4(a)

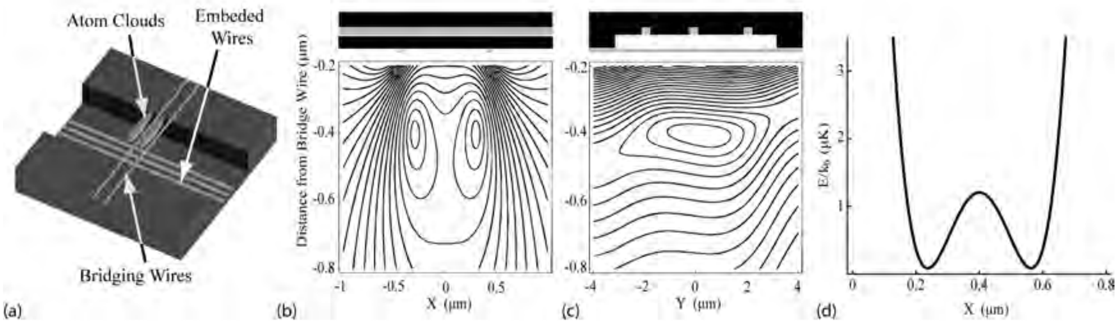

Figure 5.4: (a) Schematic diagram of the proposed atom chip. (b) Double well formed perpendicular to the bridging wires. (c) The shape of one trap parallel to the bridging wires. Shown above the graphs (c) and (d) are cross-section views of the multi-layer chip structure, with conductors shown in gray and insulators shown in black. (d) 1D slice of the potential showing the double well potential.

The chip is made by a multilayer metallization process using a silicon wafer as a substrate. The trenches are micromachined into the silicon using a reactive ion etching process, then filled with 2 μm of copper deposited into the trenches by direct evaporation. A 3 μm thick layer of SiO_2 is sputtered onto the wafer, leaving a thick insulator between the top surface and the embedded wires. We found that the oxide surface is not flat after sputtering, making it necessary to polish the wafer with a chemical mechanical polishing process to prepare the surface for the top wires. After planarization bridging wire pairs are patterned onto the oxide surface using an electron beam lithography process. The oxide layer beneath the wires is removed with a buffered oxide etchant, leaving the bridges intact. Test chips were made with with three wire widths, 500 nm, 300 nm and

200 nm, all 120 nm thick. Fig. 5.5 shows a chip with 300 nm wide wires. The separation between the wires in all cases is 1 μm.

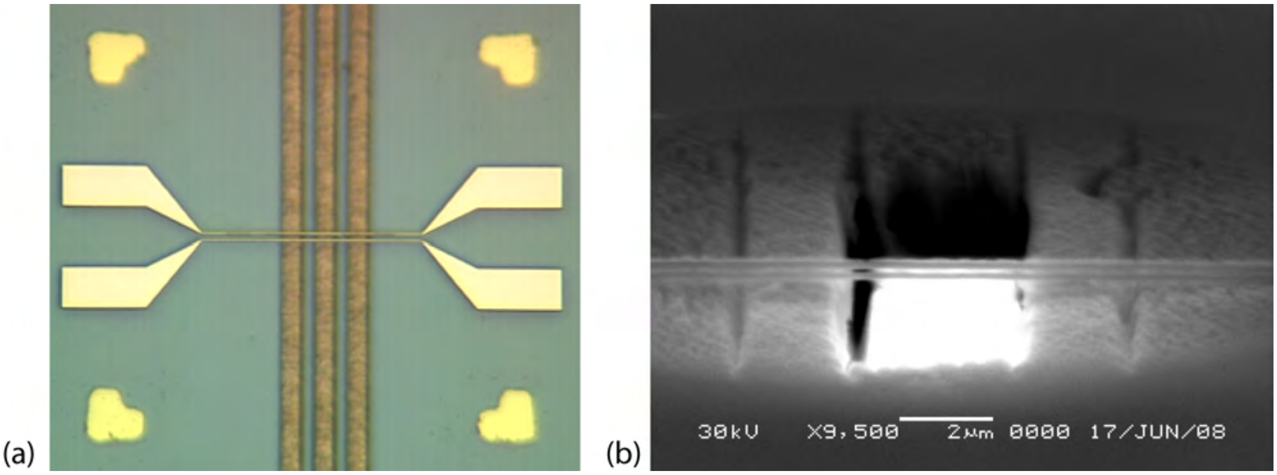

Figure 5.5: (Color). Fabricated double well chip region. (a) Photograph of the double well chip. Thick vertical traces are the embeded wires for confinement along the weak axis. Thin traces are the 300nm wide traces for generating the traps along the tunneling axis. Reference marks in the corners are spaced at $100\mu m$. (b) SEM micrograph of the bridging atom chip wires after they have been released from the substrate. Bright region at the center of the image is the center embedded wire.

With the above described geometry, it is possible to generate a double well trap with a trap separation of less than 1 μm and a barrier height of a few μK with no more than 1-2 mA of current. Destructive tests on the chips in vacuum showed that the 500 nm, 300 nm and 200 nm suspended wires could carry 41 mA, 24 mA and 18 mA, respectively for at least 5 seconds before burning out. In addition, the results show that the burnout currents for each wire width were greater under vacuum than in air, due to a copper oxide layer forming on the wires when heated by current in air. It is worth noting that under similar conditions all of the wires are able to carry roughly the same current density of $\sim 7 \times 10^7$ A/cm^2. This is approximately a factor of 10 less than the expected maximum current density for a copper trace on a silicon substrate [18], which we attribute to the lack of heat dissipation through the substrate. Nevertheless, all of the tested wires were suitable for atom tunneling experiments.

5.1.3 Full magnetostatic transistor chip design

The test chip we fabricated would be potentially useful for some experiments, but it would not allow us to generate the triple well needed for the transistor. To do that more conductors will be needed. The field shown in fig. 5.1(b) is a fairly straightforward triple well potential, but it does not satisfy the potential requirements for the atom transistor: There is no way to make the middle well tight compared to the outer two wells, and there is no good way to bias all three wells relative to each other. These issues may be addressed with an array of wires that would mimic an arbitrary current density across the chip surface. Careful choices of the currents in the traces will produce potentials that are consistent with the transistor requirements. After some exploration of the problem we settled on a ten wire design. Nine of the wires comprise the bridging region of the trap and would be directly above the atoms. The wires are designed to be equally spaced at 1 μm intervals, and with a width of 200 nm, and 100-150 nm thick. The width choice is base on the current capacity results of the experiments described in the previous section, and the thickness is based on the limits of what is practical to fabricate given the process that we had developed.

The outer two wells are each generated by three wires run in the same direction. The three wire potential mimics a wide wire, artificially loosening those two traps relative to the the middle trap. The middle well is made with the three wires in the middle of the array. To make the trap as tight as possible the outer two wires in that set are run in reverse, which compresses the trap along the tunneling axis. A tenth wire, parallel to the other nine, sits a few mircons to the side of the array and is present to apply a field gradient to the potential. An example of the magnetic field calculated for the nine wire potential without the bias wire is shown in fig. 5.6, and a close up artistic view of the designed wire geometry in shown in fig. 5.7(a). As with the test chip, the weak axis of the trap is generated with wires embedded in the atom chip below the surface.

In our systems the atoms are trapped on the chip before RF evaporation to degeneracy. The transistor geometry would not be able to support the currents necessary to capture and hold the enough thermal atoms to produce BEC. To produce the larger evaporation trap we chose to

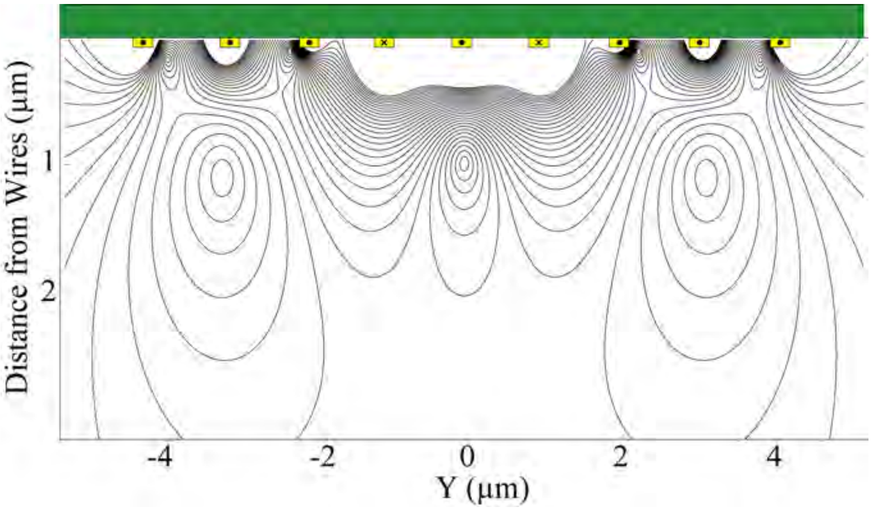

Figure 5.6: (Color). Magnetic field from a nine wire array of nano-bridges for generating a transistor potential. Current directions in the wires are indicated by • for current flowing out of the page and × for current flowing into the page.

pursue a carrier chip approach, where the field for capturing and producing the BEC would be generated by normal sized $(100 \times 10\,\mu)$m wires, and the transistor region of the chip would be on a separate "science" substrate bonded to the carrier chip. This approach is similar to the combined chips demonstrated by [92]. The focus of the science chip is two transistor sites, each occupying a $100 \times 100\,\mu$m region at the center of the science chip surface. The science and carrier chips are shown artistically in fig. 5.7(b), where the top and bottom edges of the science chip have been cut away to show the wire trace on the carrier chip. The connections to the science chip are made through wire bonds to the carrier chip. The carrier chip consists of a simplified version of the chip shown in fig. 4.11(b), which would allow production of BEC in a dimple trap. On either side of the main, 100 μm wide dimple wire are two smaller, 25 μm wide dimples to locate the atoms over the transistor sites on the science chip. The carrier chip also has electrical vias and wire bond pads for each of the traces on the science chip. The science chip is designed to be 50 μm thick, a width thick enough to make it possible to fabricate and handle the chip, but thin enough to enable magnetic transfer of the atoms between the carrier and science chips.

This chip design was extremely ambitious, as it incorporated multi-layer structures, bridging nano-wires, a carrier-science chip assembly, and UHV compatible vias all in one atom chip. Significant progress was made towards fabricating these chips, but in the spring of 2009 we were forced to temporally shelve the design. Although any one of the above mentioned challenges was achievable on its own, it became prohibitively expensive and difficult to produce an atom chip which incorporated all of the required features.

5.2 Window chips

The compound substrate technology discussed in chapter 4 opened up some new opportunities in atom chips. In addition to being a reliable technology for electrical vias, the compound substrate also provided a new way to make through-chip optical vias. We had explored on chip optics and optical feedthroughs already at some length with a collaboration with the Sarnoff corporation, where windows and optics were attached to a silicon substrate with andodic bonding. Examples

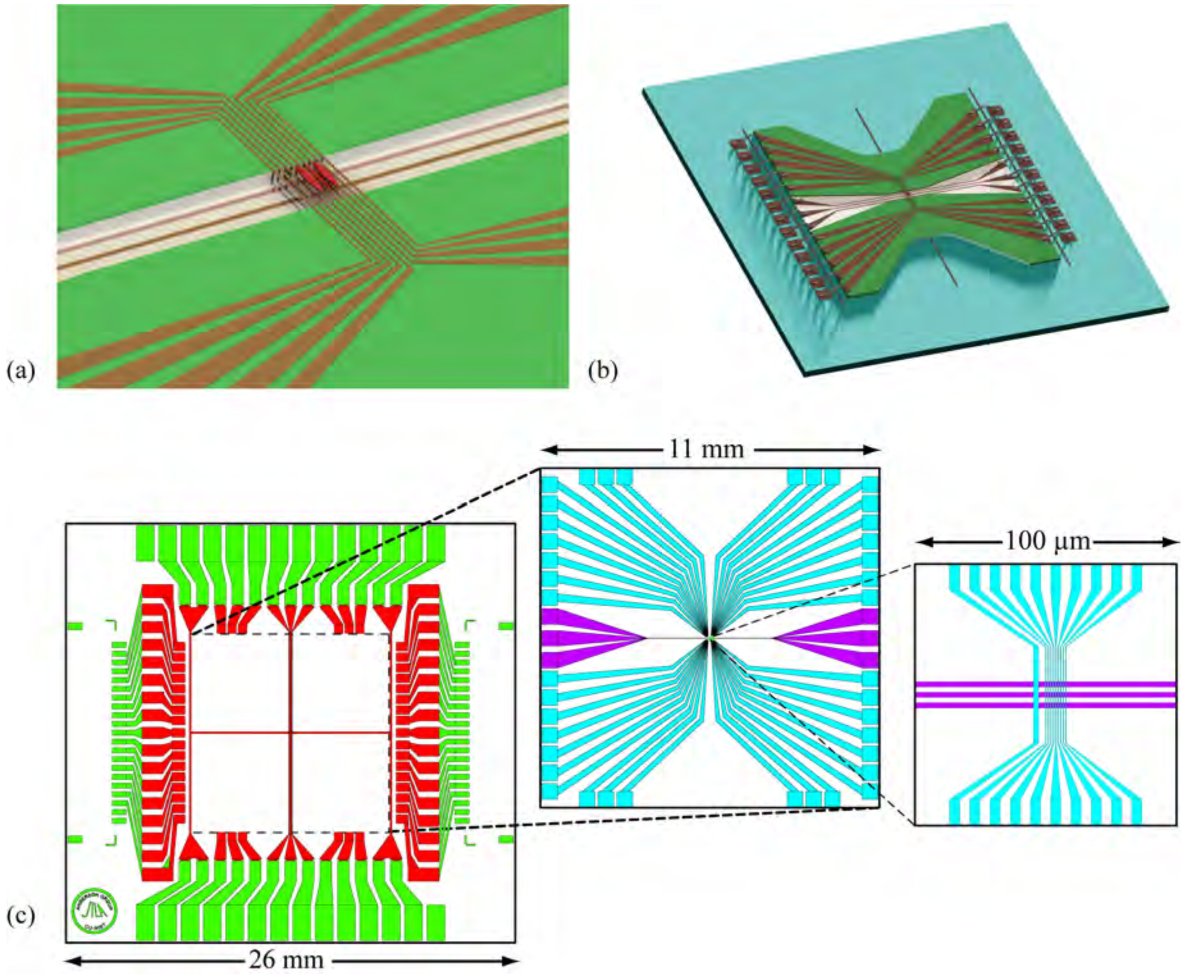

Figure 5.7: (Color). The full transistor chip design. (a) Close up view of the transistor region of the chip. Atom clouds are shown in red. (b) Artistic rendering of the full transistor chip with the science chip cut away to show the underlying dimple wires. (c) left: The carrier chip design with ambient side metallization shown in green and vacuum side metallization shown in red. Middle: The science chip full view Embedded wires are shown in purple, and the top wire layer is shown in blue. Right: 1 of two central regions of the science chip.

of such devices are shown in fig. 5.8(a) and (b). The goal of that work was primarily focused on on-chip optics, as might be useful for atom interferometry [93]. We had also developed some similar technology for through chip imaging with the channel cell technology discussed in chapter 3. The channel cell geometry would not allow for imaging of atoms with a probe beam parallel to the atom chip, as the silicon frame of the cell would block the beam. To mitigate this problem we fabricated a window chip, shown in fig. 5.8(c). This chip would allow absorption imaging through the chip after the cloud had been allowed to drop far enough to be observed with a probe beam, as shown in fig. 5.8 (d). This approach to imaging atoms through the chip was not thoroughly explored because the channel cell has not yet been used for on-chip experiments.

The compound substrate technology took the window chip concept a big step forward because the optical surface is co-planer with the silicon substrate. This makes it possible to fabricate atom chips with metal traces directly over the glass, and therefore trap atoms arbitrarily close to the center of an easily accessible optical surface. The first chip that we fabricated with this new technology is shown in fig. 5.9. Heat dissipation of the wires directly on the glass is a major concern with window chips. When the wires are patterned onto the silicon surface, which has nearly one hundred times the thermal conductivity of glass, the heat is spread over the entire chip volume. Over a window the trace can dump almost no heat, and the wire will heat up dramatically. The problem can be reduced significantly by limiting the size of the glass region on the chip, provided the window is not so small that it limits the aperture of the optical system.

Taking a cue from the excellent work being done in Markus Greiner's lab at Harvard [94], and the work being done in Immanuel Bloch's lab at LMU [95], we decided to use the window chip technology to implement a hybrid magnetic-optical approach to making an atom transistor. The basic idea behind the hybrid transistor trap is straightforward: The atoms are held in a tight magnetic trap below a window where they can be optically accessed from above. An optical pattern is projected on the cloud through a microscope objective to modify the potential and generate barriers and offsets appropriate for tunneling experiments. The projection system is shown schematically in figure 5.10

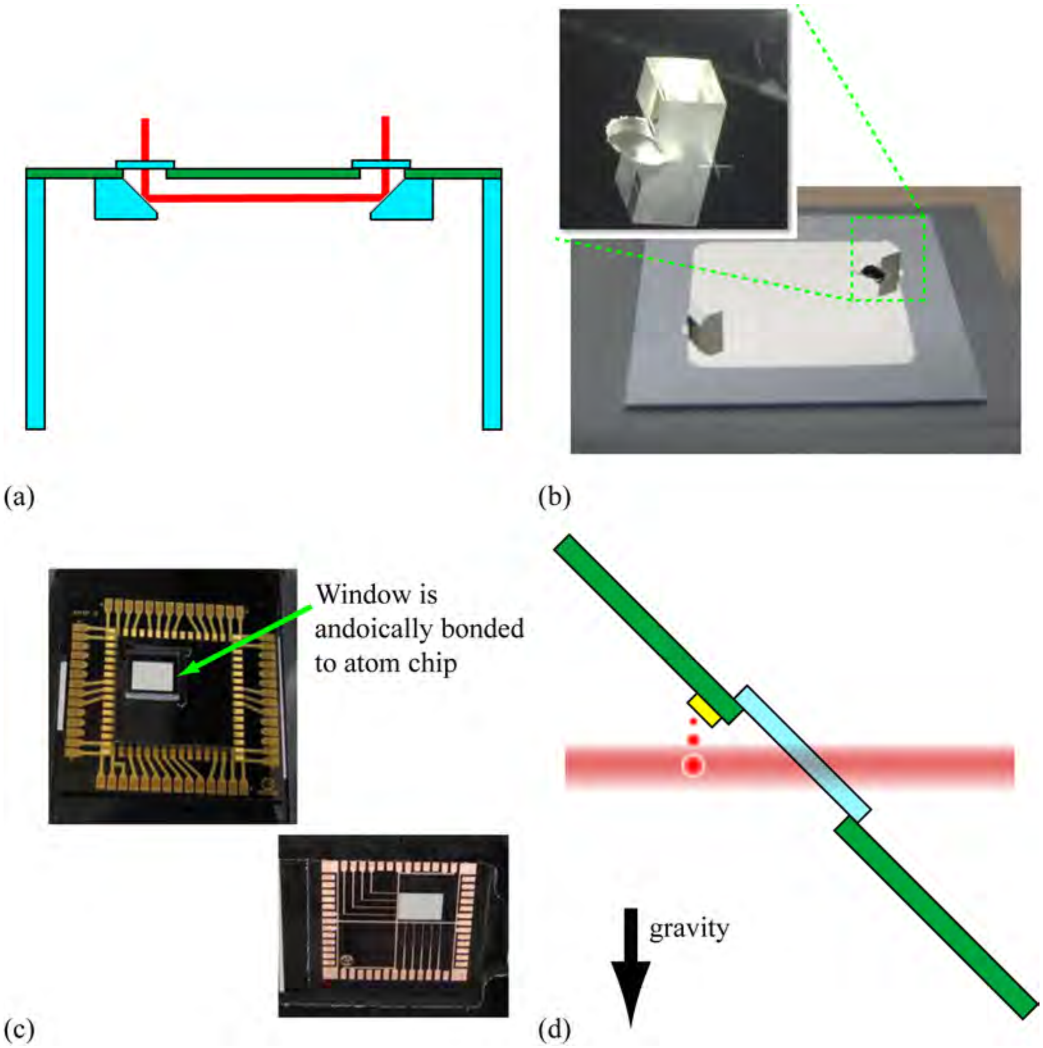

Figure 5.8: (Color). Early generation optical vias. (a) Schematic of the Sarnoff through chip optical vias with prisms for atom interferometry. (b) Sarnoff optical vias. (c) First generation window chip for through-chip imaging of atoms in the channel cell. (d) Schematic of intended imaging configuration.

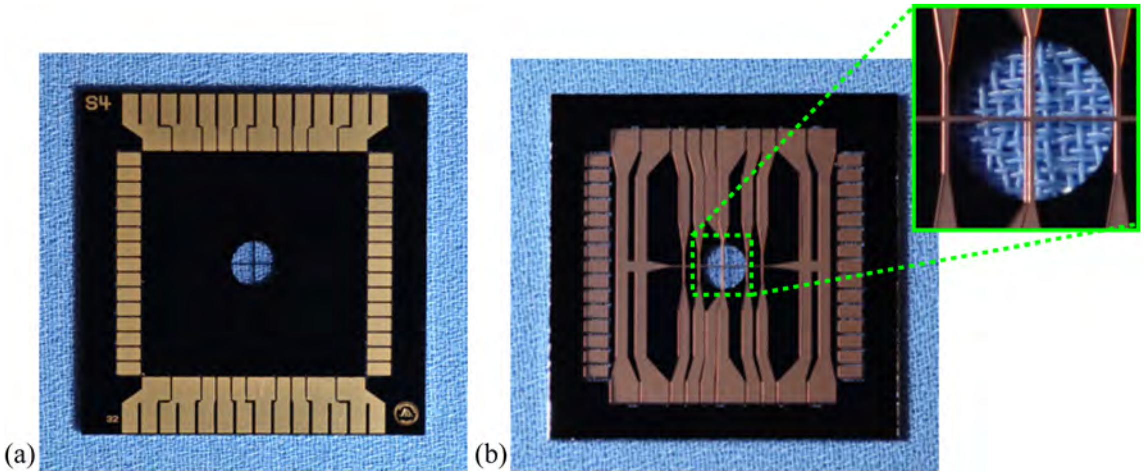

Figure 5.9: (Color). Version 1.0 window chip. (a) Ambient side metallization. Atom chip is 23mm on each side. (b) Vacuum side metallization showing dimple wires crossing over the window. Window diameter is 3mm, and wire traces over the window are $100\mu m$ wide and $10\mu m$ thick. Second wire next to the dimple wire is $50\mu m$ wide.

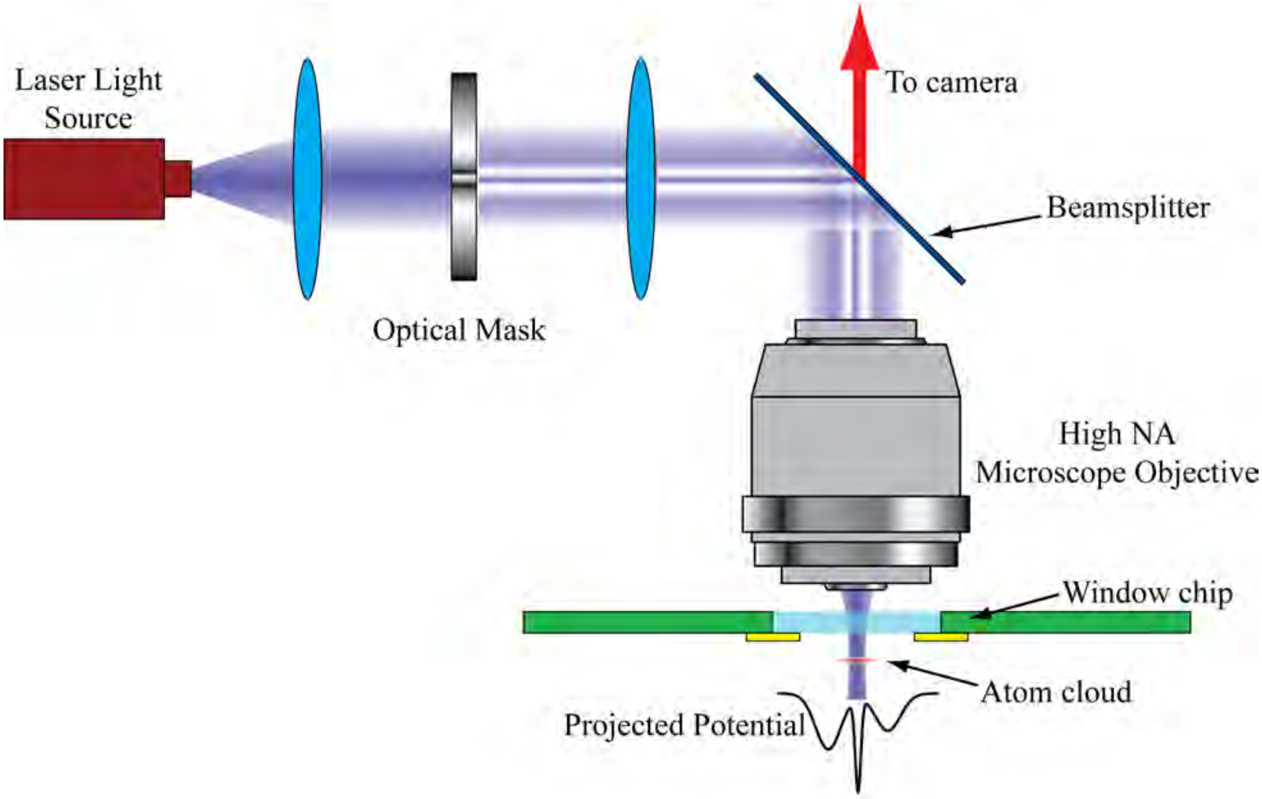

Figure 5.10: (Color). Schematic diagram of the window chip optical projection system. The image of the mask is projected onto the atom cloud, modulating the magnetic potential which holds the atoms. The beamsplitter is in place to allow for the microscope objective to also be used for imaging.

An additional feature of this projection system is that it can double as an imaging system with equally high resolution. This is done by putting a beamsplitter in the path of the projection system and imaging the atoms with either absorption or fluorescence imaging. The details of the imaging system are discussed in greater length in chapter 6.

5.2.1 Atom transistor potentials with optical projection

It is, in principle, possible to generate nearly any optical pattern in the projection plane, provided that the feature size of the projected image is within the resolution limits of the system. As discussed in chapter 2, it is preferable to use a blue-detuned optical trap since the atoms will spend the majority of their time in the darkest region of the trap. This allows the light source to operate closer to resonance with lower power and fewer scattered photons. As demonstrated in [94], a white light source for the projection system would be preferable to mitigate the effects of interference between reflections off the many optical surfaces in the projection system. The maximum coherence length should be less than the width of the thinnest optic in the system. In our case this would be the chip window itself, which is 420 μm, corresponding to an optical linewidth of ~ 0.4 nm.

Consider as an example the optical pattern shown in Fig. 5.11. Fig. 5.11(a) shows a candidate optical pattern that would result in the 1 dimensional potential shown in 5.11(b). To generate this field at 760nm a total optical power of less than 1 mW at the position of the atoms would be needed. The mask for the optical potential could be generated, for example, by a hologram [94], a mechanical block of the light, or a spatial light modulator. In the case of the transistor it would be preferable to us a spatial light modulator, as the potential could be varied in time, which could enable preparation of the system.

As was discussed in chapter 2, not only must there be a way to load a controllable number of atoms into the gate well, the atoms in that well must have a well defined and controlled phase relationship with the atoms in the source. One possible way of loading the trap would require precise control of a time varying potential. Consider the series of images shown in fig. 5.12. The

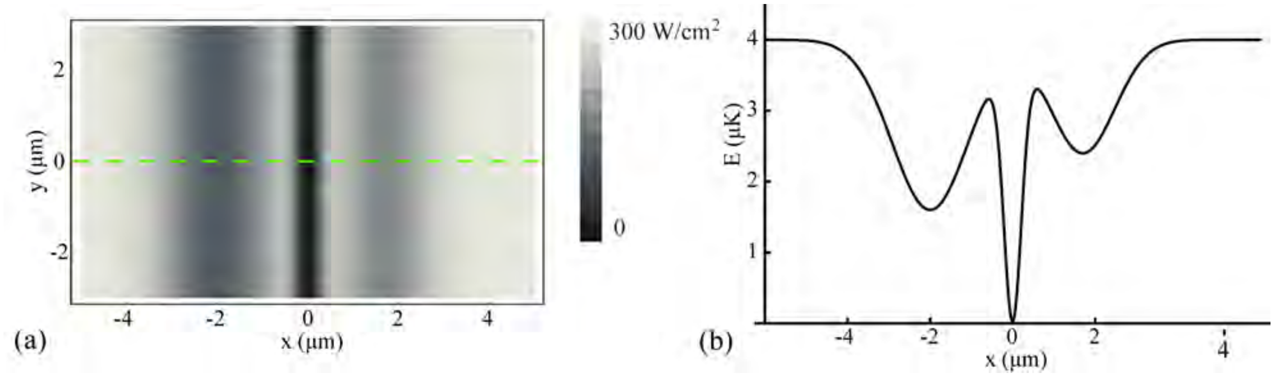

Figure 5.11: (Color). (a) candidate optical intensity profiel at the position of the atom cloud. The potential is assumed to be using blue detuned light at 760 nm. Atoms are trapped in dark regions of the optical field. (b) Slice of the potential landscape across the dashed green line in (a).

first plot of both (a) and (b) show the condensate in a single potential well, which will become the source of the atom transistor. By slowly ramping on the gate well, as shown in first five plots of 5.12(a), atoms are allowed to tunnel across the barrier into the gate, keeping the two-well system in equilibrium. The drain well can then be turned on, as shown in the last graph of (a), and the actual transistor experiment may begin,. Fig. 5.12 (b) shows the system being prepared with a non-resonant gate condition. The gate is turned on slowly at first, as shown in the first two plots of (b), to allow some atoms into the gate, and then quickly ramped all the way on, which freezes the atom number in the source and the gate, as in the macroscopic quantum self-trapping demonstrated by [59]. The drain well is then turned on and the experiment begins, although now nothing will happen. It should be noted that slowly and quickly in this context are both relative to the tunneling rates of atoms across the barriers. This approach is, in function, similar to the recent experiments in Immanuel Bloch's lab where atoms were loaded from a single lattice site into the double well of a "super-lattice" by adiabatically ramping on the second well [96].

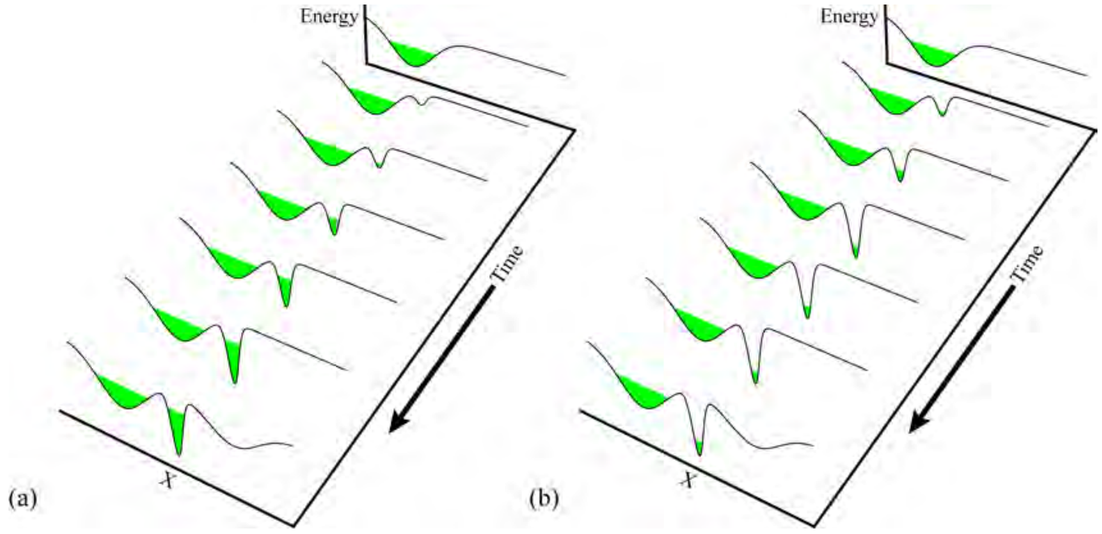

Figure 5.12: (Color). A possible scheme for loading the atom transistor. (a)Resonant loading case: The gate well is lowered adiabatically which keeps the two well system of the source and gate in equilibrium, shown as a time sequence of the first five graphs. The drain well is then turned on quickly and the transistor action commences. (b)Non-resonant loading case: the gate well is partially loaded, the quickly turned all the way on, creating a chemical potential miss-match between the source and the gate. The drain is then turned on quickly to begin the experiment.

To demonstrate the above loading sequence it will be necessary to have precise control of the potentials. This could be done by using a high quality spatial light modulator in a manner similar to what is described in [97, 98]. A series of pre-determined images would be sent to the SLM with each one being only slightly different from the last. Provided that the image shift is quiet and that the step size in the changes is small this will appear to the atoms to be adiabatic.

5.3 Atom chip designs for window chips

As discussed previously, to make a successful transistor it is necessary to generate potentials with feature sizes of about one micron. In the case of magnetic trapping the minimum feature size was dictated by the size of the wires on the chip. In the case of optical projection the limit is dictated by the resolution of the projection system. The minimum feature size that can be resolved by a diffraction limited optical system is determined by the numerical aperture (NA) of the system. The Rayleigh criteria for this is [99]

$$\Delta r = 0.61 \frac{\lambda}{NA}. \tag{5.4}$$

At a wavelength of 780 nm we need a numerical aperture of at least 0.5 to project and to resolve a 1 μm feature. It is worth noting that the aperture limit may not actually be the microscope objective. In our case the limiting aperture may be the wires on the atom chip, or the edges of the window in the chip itself, as shown in figure 5.13.

The atom chip shown in figure 5.9 was meant to be proof of concept chip to show that it was possible to both fabricate a chip with wires over a window and that the wires could support the intended current. The chip was not designed with optical trapping and through chip imaging in mind, and as such is not particularly well suited to those goals. Copper is opaque at 780 nm, making it necessary to move the atoms out from underneath the traces. The wire patterns on the V1 window chip make it possible to produce a BEC in one of the four basic chip traps described in chapter 4, all of which in their simplest form will trap the atoms directly under the wires. By

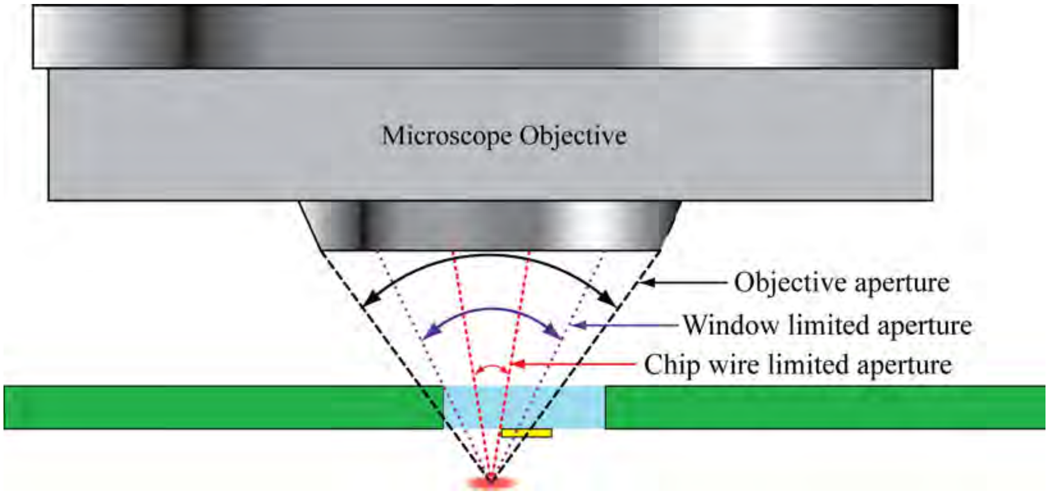

Figure 5.13: (Color). Limiting apertures for the window chip: The wire traces or the edges of the atom chip window can limit the numerical aperture of the microscope system, resulting in a lower resolution system.

applying an additional bias field perpendicular to the atom chip the trap can be rotated out from underneath the wires, but this comes at a cost: Atoms in a tight trap will be relatively close to the wire, and applying a bias field perpendicular to the chip will only move them to a position where they still cannot be seen. To get the atoms directly under the window the trap must be moved away from the wire, which decompresses the chip trap. This is shown schematically in fig. 5.14. Fig. 5.14 is somewhat misleading, as it only shows the rotation of a trap around a single guide wire. Adding the dimple wire complicates the problem quite a bit, as the trap will rotate about both the main wire and the dimple wire. This can push the magnetic field through a zero, which will cause the trap to split.

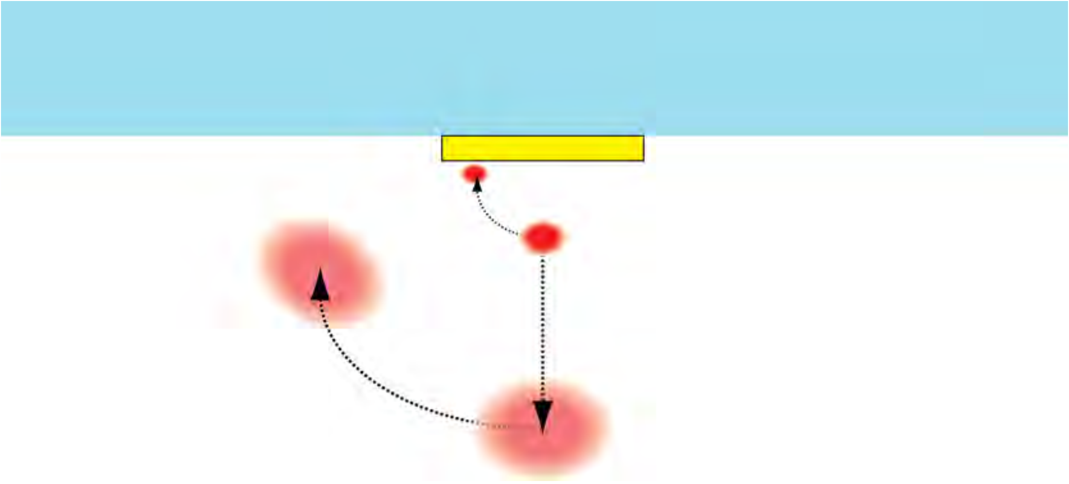

Figure 5.14: (Color). Moving the atom out from underneath a guide wire requires that the trap be loosened to get the atoms far enough from the wire to be in view of the microscope system. This causes the atom cloud to be larger and more diffuse, making high resolution projection and imaging impossible.

A more window-friendly design is one where the atoms are trapped above the substrate rather than the wire. One example of such a trap is shown in figure 5.15. The chip field consists of two wires separated by a distance d each carrying current I_s in opposite directions. Along the symmetry axis the horizontal components of the field cancel, leaving only a field perpendicular to the chip surface. This magnetic field is given by

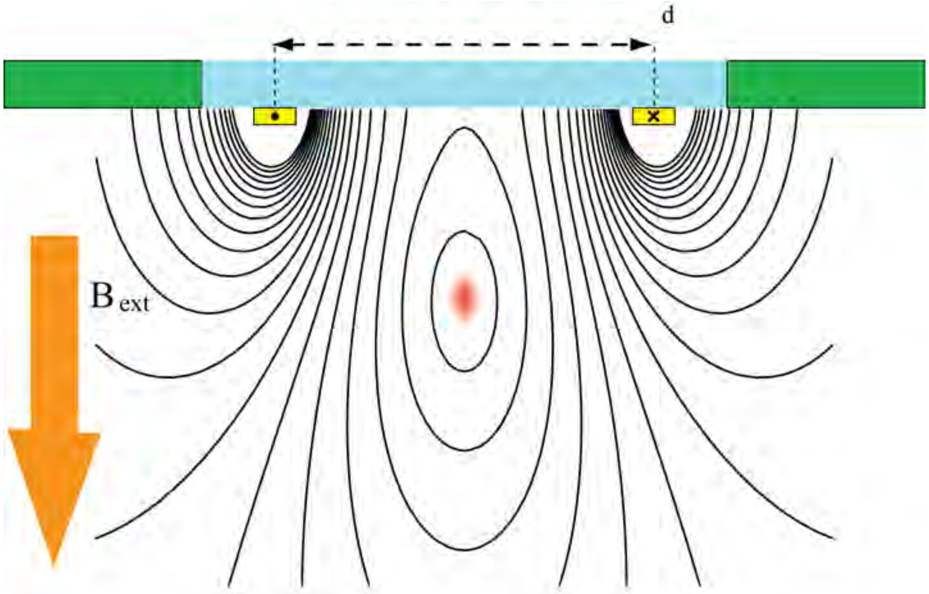

Figure 5.15: (Color). Schematic of split wire window chip design. Atoms are trapped between the two guide wires at any experimentally chosen position relative to the window. This configuration allows for tight traps in full view of the cloud, and allows for an objective limited aperture.

$$B_z = \frac{\mu_0 I}{2\pi} \frac{d}{\left(\frac{d}{2}\right)^2 + z^2}. \tag{5.5}$$

Applying an external bias field B_{ext} in the vertical direction cancels the trap field at a position

$$z_0 = \sqrt{\frac{dI_z\mu_0}{2\pi B_{ext}} - \frac{d^2}{4}} \tag{5.6}$$

As with the side guide described in chapter 4 the split wire guide may be made harmonic by applying a bias field B_x along the axis of the trap. The expanding field about z_0 gives

$$B \approx B_x + \frac{2B_z^3\pi\left(y^2 + (z - z_0)^2\right)}{B_x dI_z\mu_0} = B_x + \frac{2B_z^3\pi}{B_x dI_z\mu_0}\rho^2, \tag{5.7}$$

where we have again defined $\rho = \sqrt{y^2 + (z - z_0)^2}$. The trap frequencies in the guide can be calculated as in eq. 4.7, which gives

$$\omega_\rho = \sqrt{\frac{4\pi\mu_a}{m\mu_0}\frac{B_z^3}{dI_z}} \propto \frac{B_z^{3/2}}{\sqrt{dI_z}} \tag{5.8}$$

It is important to note that in case of the split wire trap it is possible to move the trap arbitrarily close to the atom chip surface by simply increasing the strength of the bias field. If one decreases the current as the bias is increased the trap may be moved without significantly changing the trap parameters. This allows the experimenter to form a trap close enough to the window that the chip wires will not be the limiting aperture of the optical system.

The split wire guide does not confine the atoms along the axis of the guide. Since we wish to keep the center space of the window clear of any wires that would obstruct optical access we cannot use a dimple type trap. However, the H traps and the T traps described in chapter 4 are reasonable choices. The T trap comes with the advantage of having tighter confinement along the guide axis than an H or Z trap, but the T trap still works best when the atoms are directly below the cross point of the wires. The H trap can locate the atoms exactly where they are needed over the wires, but the split wire configuration gives rise to a current management problem, as four wires crossing will mean that there is no control of the current closest to the atoms. This can be dealt with by placing the wires on the opposite side of the substrate, which in our case is 420 μm further from the atoms. To compensate for the difference in wire distance the H wires require significantly more current. Fortunately, since the wires are further away the traces can also be much thicker, which reduces the current density in the wire. To compromise between a tight trap for RF evaporation and a looser trap to hold atoms near the window the chip was designed to allow for both H and T traps. The chip design is shown in fig. 5.16, and the final atom chip is shown in fig. 5.17.

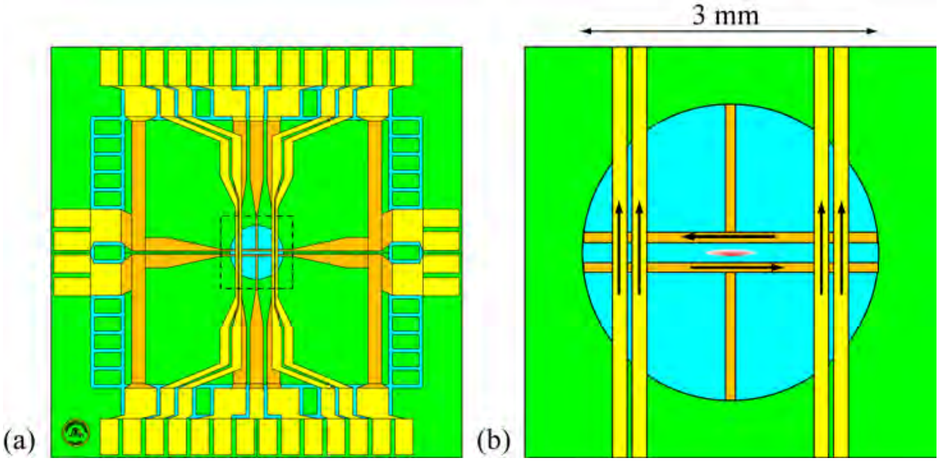

Figure 5.16: (Color). (a) X-ray view of the V2 window chip. Ambient side metallization is shown as yellow, while vacuum side metallization is shown as orange. (b) Zoomed in image of the window region indicated in (a) by the dashed line. Current directions for a modified H-wire trap are shown.

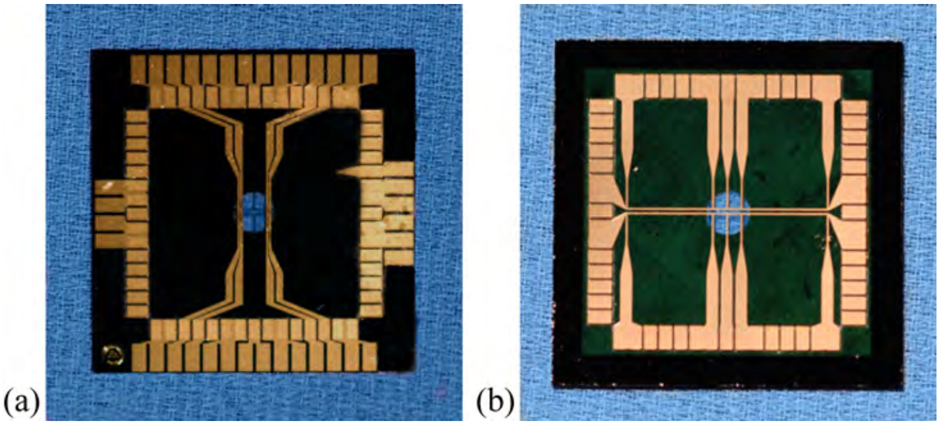

Figure 5.17: (Color). V2 window chip. (a) Ambient side of the chip. (b) Vacuum side of the chip. Chip is 23mm on each side.

Chapter 6

Table top BEC apparatus

This chapter describes the apparatus that we have built for atom transistor experiments. In contrast to the portable system, this machine is built to be flexible rather than compact. The laser system is a much more conventional approach to BEC laser systems, which allows for changes and modifications to be made quickly. The electronic system is primarily made from commercial equipment wherever possible. The opto-mechanical system is built to optimize optical access and to give future experimenters as much space to work with as possible. In this chapter we will describe all of the subsystems of the experiment in detail.

6.1 Laser system

Our BEC production process employs 4 basic laser frequencies, all near the ^{87}Rb D2 line:

(1) Cooling light tuned approximately 2Γ to the red of the $|F=2\rangle \rightarrow |F=3\rangle$ transition.
(2) Repump light tuned on resonance with the $|F=1\rangle \rightarrow |F=2\rangle$ transition.
(3) Optical pumping light tuned about 2Γ to the blue of the $|F=2\rangle \rightarrow |F=2\rangle$ transition.
(4) Probe light tuned either on or near the resonance of the $|F=2\rangle \rightarrow |F=3\rangle$ transition.

The cooling light must be reasonably frequency agile and allow for detunings as large as 12Γ for the compressed MOT and polarization gradient cooling. The repump laser must have dynamic control of the power into the system for both of the above mentioned stages. The pump and probe lasers do not need any dynamic control of frequency or power, but it is useful for it to be possible to set those laser frequencies at an arbitrary detuning from their respective transitions. We typically require 30-50 mW of cooling power for the 3D MOT and 60-200 mW for the 2D. The repump must supply 6-10 mW of power to each MOT, preferably more to the 2D. The pump and probe must each have a few (2-3) mW of power. All of the power requirements are after single mode optical fiber that couples the laser system to the experiment.

To achieve these requirements our apparatus uses a laser system that consists of 5 lasers and a tapered amplifier. A layout of the laser system is shown in figure 6.1. The master, cooling, repump, and pump/probe lasers are home-made external cavity diode lasers built by the JILA shop, and designed by Scott Papp [100]. The slave laser is a simple injection-locked laser diode that is used to amplify the repump light. All of the home built lasers are powered by JILA-built current and temperature drivers. Each laser is frequency stabilized by feeding back a signal to both a piezo that drives the external cavity and to the current of the laser diode.

The master laser is locked to the ^{85}Rb $|F = 3\rangle \rightarrow |F = 2 - 4\rangle$ crossover resonance using a standard saturated, or “doppler free,” absorption spectrometer. This laser is used as a frequency reference for the cooling laser, which is in turn stabilized to the beat note frequency by means of a phase locked loop. This added complexity of stabilizing two lasers relative to one another is used to allow for nearly arbitrary control of the cooling laser frequency over eight times the range of the reference VCO, which corresponds in our case to a frequency range of about 400 MHz. The phase locked loop is in many ways preferable to the alternative methods of achieving frequency agility, such as double pass acousto-optic modulators or unlocking and pushing the laser, because it gives the experimenter greater control of the laser output frequency over a larger range without needing to worry about power fluctuations or frequency drifts. Additionally, the phase locked loop can avoid the carrier frequency modulation added to the laser frequency in most peak locking schemes, provided that the servo bandwith of the phase locked loop is less than the modulation frequency.

40 mW of cooling laser light is used to seed the tapered amplifier. For the TA we use a Toptica BoosTA that provides about 14 dB of optical gain, and allows for a maximum output power of 1W at 780 nm. The output of the TA is split into two beam paths that each contain a

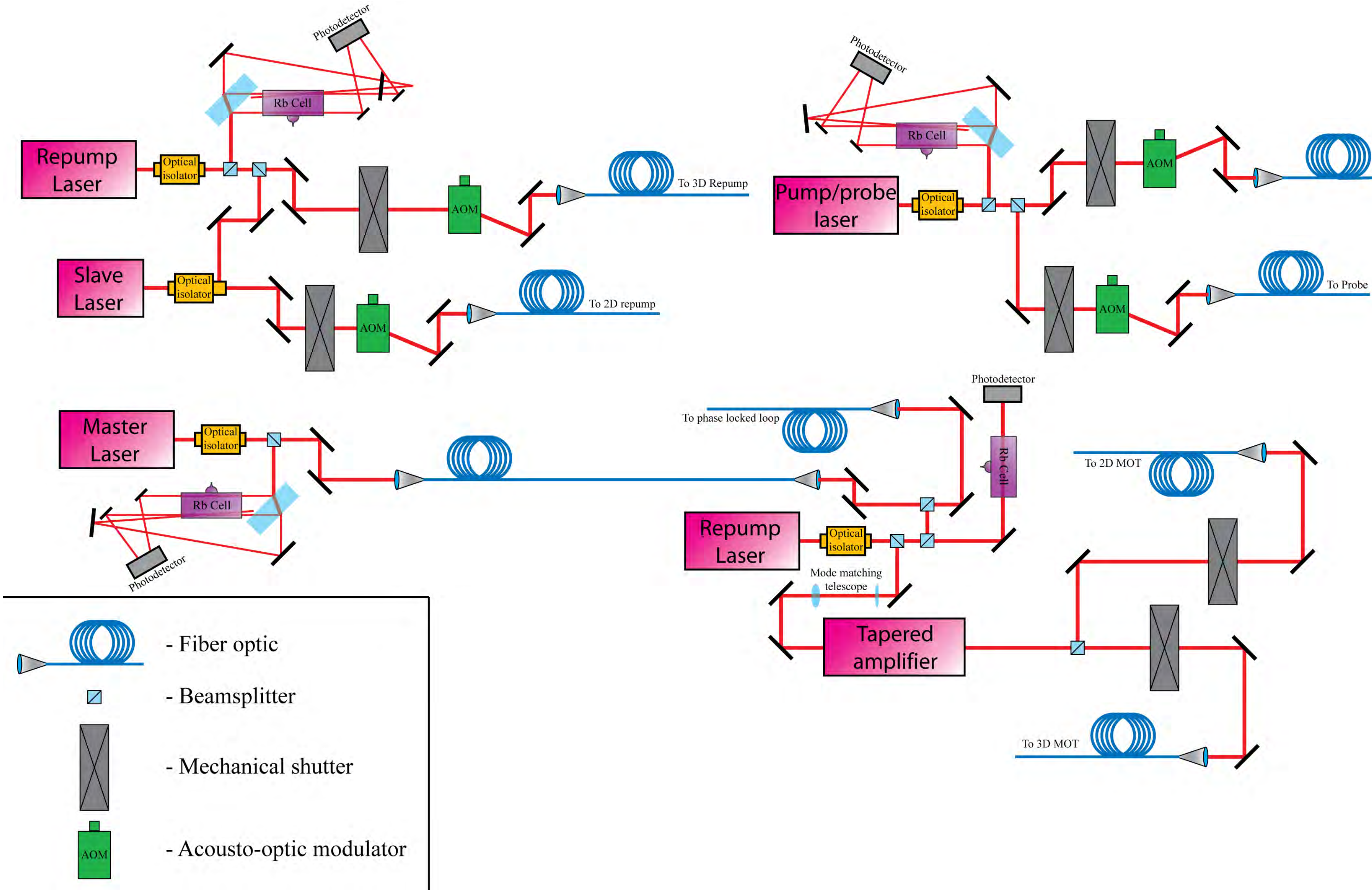

Figure 6.1: (Color). Laser system diagram. Diagram is schematic and many optics, such as waveplates, have been left out for clarity.

mechanical shutter and a fiber coupling setup. For fiber coupling we use single mode polarization maintaining fiber (Corning Panda 850), which requires a quarter waveplate and a half waveplate to correctly set the polarization before each fiber input. The beam path for the 3D MOT includes a polarization rotator (Boulder Nonlinear Systems XT Series) and a polarizing beamsplitter which makes it possible to dynamically control the total power to the 3D MOT; a feature we use during polarization gradient cooling. After fiber coupling there is 350 mW of cooling light available for the 2D MOT and 50 mW for the 3D MOT.

The repump laser is locked to the $|F=1\rangle \rightarrow |F=1-2\rangle$ crossover resonance with a doppler free spectrometer. A small amount of that light is split off and used to seed a slave laser. The light for each repump beam passes through a mechanical shutter and an acousto-optic modulator which detunes the light 87 MHz to the blue. The 3D repump AOM is used to decrease the repump output power during the compressed MOT and polarization gradient cooling. After fiber coupling there is 8 mW of repump into the 3D MOT and 18 mW into the 2D MOT.

The pump/probe laser is locked to the $|F=2\rangle \rightarrow |F=2-3\rangle$ crossover resonance with a doppler free spectrometer. The light is split into two paths, one for the pump and one for the probe. Both beams pass through mechanical shutters and acousto-optic modulators, but the pump light is red detuned by 121 MHz to be 12.5 MHz blue of the $|F=2\rangle \rightarrow |F'=2\rangle$ transition, and the probe light is blue detuned by 133.5 MHz to be resonant with the cooling transition. In the case of the pump and the probe we use the AOMs as shutters as well as frequency shifters. Both pump and probe stages require short light pulses ($\Delta t < 1$ms), which is diffficult to achieve with a mechanical shutter. Instead, by turning off the RF power to the AOM the beam can be shuttered in the time it takes for the acoustic wave to traverse the crystal, which can be as fast as tens of nanoseconds. Both beams are coupled into fibers, and about 3mW of power is available in each, although the power is typically less during operation.

6.2 Coils

In order to generate the external magnetic fields needed in the experiments we use sets of coil pairs in helmholtz or antihelmholtz configurations. There have been two generations of coils designed and built for this experiment. The original coils shown in figure 6.2(a) were developed with the intent of being used with the atom chip described in the beginning of chapter 5. The assembly consists of 4 pairs of coils: three helmholtz pairs to provide bias fields in three orthogonal directions, and one antihelmholtz pair to generate the MOT field. This coil assembly was designed to be used in conjunction with an external Z wire, shown in fig. 6.2(b) to magnetically capture the atoms after laser cooling and transfer the atoms to the chip [23, 24]. These coils worked very well for their intended purpose, and we were successful in producing BEC using them. This coil design is not appropriate for use with window atom chips, as the presence of the external Z wire obstructs the back side of the chip, making it impossible to get the microscope in place.

The second generation coil set employed a quadrupole coil ladder to move the atoms from the MOT to the atom chip [101], shown schematically is figure 6.3. This transfer scheme has many drawbacks for atom chip work. First, the transfer scheme is fairly power hungry compared to the external Z wire. While the external Z typically employs a very large peak power, the power dissipation is reduced as the atoms are brought closer to the atom chip. In the quadrupole coil case the total power dissipated is roughly constant throughout the transfer process. Also, the external Z wire trap can be adiabatically merged with the Z wire trap on the atom chip, which would allow transfer into the chip trap without a decrease in phase space density. In practice the mismatch in the geometries between the chip Z and the external Z prevent this from being a completely smooth transition, but the atoms remain trapped for the entire process. In the case of the quadrupole transfer the atoms must be moved from a linear trap to a harmonic one, which requires a "toss and catch" approach for the transfer. This approach has been shown by many groups to be effective [20, 74], but it typically comes at a cost of significant heating and loss of atoms number.

The major design considerations for the coil geometry are as follows:

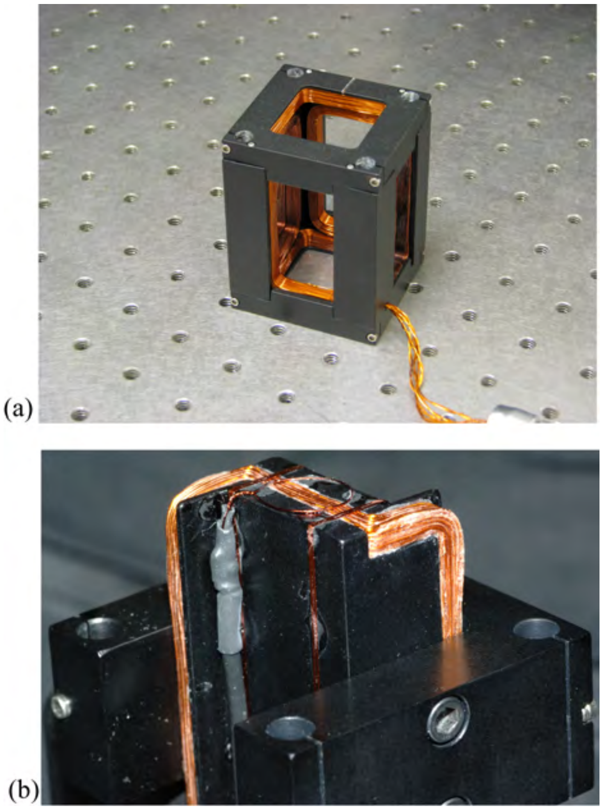

Figure 6.2: (Color). (a) V1 coil assembly, consisting of four pairs of coils for producing quadrupole fields and bias fields in three directions. (b) External Z-wire used in conjunction with the coils shown in (a).

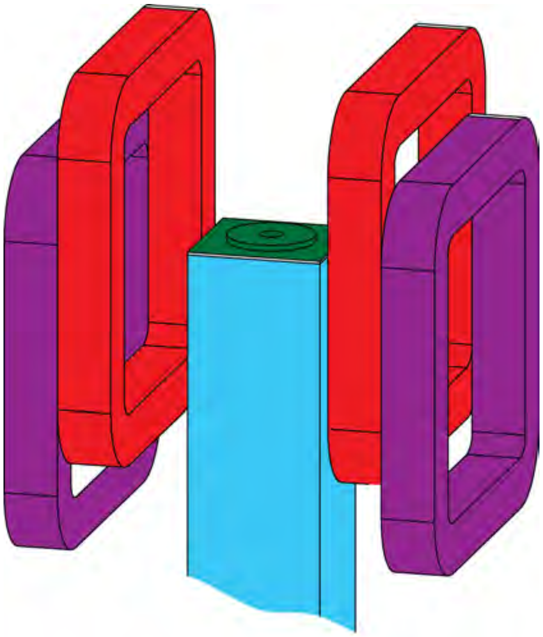

Figure 6.3: (Color). Quadrupole transfer coils used to transport atoms from the MOT position to the atom chip. MOT coils are shown in purple, and transfer coils are shown in red.

(1) The coils must have a clear aperture large enough to accommodate all of the laser beams necessary for laser cooling and imaging, and also enough to allow for the largest microscope objective we are likely to use. The objective we use is a 40x Zeiss LD Plan Neofluar, which has a maximum diameter of 38 mm.

(2) The coils must be able to hold the atoms against gravity at the level of the MOT, and achieve a field gradient of at least 150 Gauss/cm along the strong axis at the level of the atom chip. This requirement is consistent with the transfer scheme employed by Horikoshi et al [22].

(3) Total power dissipation should be kept to a minimum.

(4) The coil assembly must be designed in such a way that it can be held rigidly. The holding structure, if made of metal, must minimize the available paths for eddy current flow.

(5) The coils must be well matched to the available power supplies in the lab. This means that the resistance of the coils must be close to the maximum load that can be driven at full current from the supply. For example, we drive our MOT coils with a Kepco BOP 20V 10A supply. An ideal coil for that driver would have an impedance of about $2\,\Omega$. This specification must be consistent with the needed speed of the coil, as a high inductance will slow down the maximum switching speed of the coils

(6) The coils shape and spacing should be reasonably well optimized for their intended purpose, be it for applying a bias or for a gradient.

The most demanding requirement is the field gradient needed during the transfer process, so that is a reasonable place to start the design. The aperture requirement defined by the microscope objective sets the coils spacing of the closest coil pair. We chose a 40 mm edge to edge spacing to allow for some clearance around the objective. Picking this spacing defines the ideal coil geometry: The magnetic field from a pair of circular coils with radius r separated by a distance d in anti-helmholtz configuration is given by

$$B_{cir} = \frac{\mu_0}{2r}\left(\left(1+\frac{(x-d/2)^2}{r^2}\right)^{-3/2} - \left(1+\frac{(x+d/2)^2}{r^2}\right)^{-3/2}\right). \tag{6.1}$$

Taking a first derivative with respect to R gives the field gradient

$$B' = 48\mu_0 \frac{d}{r^3\left(\frac{d^2+4r^2}{r^2}\right)^{5/2}}, \tag{6.2}$$

which is maximized for

$$d = r. \tag{6.3}$$

Similarly, it is easy to show that the maximum gradient from a square anti-helmholtz coil with sides of length L and separated by d is achieved when:

$$d \approx 0.54L, \tag{6.4}$$

which is a nearly identical condition. The choice of round or rectangular coils is dictated based of the rest of the geometry of the system. We use rectangular coils to maximize optical access and to simplify how they are held.

Located just below the transfer coil is the MOT coil. For convenience of fabrication the MOT coil is the same geometry used for the transfer coil. As the MOT in our system is only 15-17 mm below the chip surface, we can design the offset between the two coils to be the same. As this is relatively small compared to the coil size it makes it simple to transfer atoms between coil pairs. The MOT coils are hooked up to independent bipolar power supplies, so they can double as bias coils by simply reversing the current flow in one of the coils. This approach moves the problem of needing a bias field and a field gradient to the computer control, reducing the total number of coils in the system. The output from the computer control is typically of the form

$$\begin{aligned} MOT_1 &= B + B' \\ MOT_2 &= B - B'. \end{aligned} \tag{6.5}$$

where B and B' are the command voltages needed to generate the desired field and field gradient respectively.

In the final design it was necessary to reduce the size of the MOT and transfer coil from the optimal geometry to make it possible to fit all of the coils into the assembly. Also, we needed to leave room for the horizontal MOT beam to pass through the center of the MOT coil pair. Having chosen a coil spacing and geometry, the only design parameter left is the volume of the coils. The maximum allowable current density in a coil is more or less constant, and for a given coil geometry the field generated by the coil will be directly proportional to the amount of power dissipated by the coil. If the design requires a stronger field than the cross section of coil will need to be made large enough to handle the power. This is balanced by the space available and the above mentioned requirement of impedance matching the coils to the intended power supply.

The coils for MOT, X bias and transfer are $\sim 60 \times 60$ mm center to center with a 9 mm square cross section. They are wound using 144 turns of 22 AWG square wire with polyimide insulation and an epoxy-bond coating (MWS Wire Company p/n 69286), which gives a final resistance of $\sim 1.4\,\Omega$ per coil, and a field gradient of 10.3 G/cm-A for the transfer coils and 8.2 G/cm-A for the MOT coil pair. The square cross section of the wire makes it much easier to wind tight coils, which we have found is particularly difficult with rectangular coil geometries, and also increases the total amount of metal in the volume. The epoxy-bond coating makes it possible to seal all of the turns in the coil together by heating.

The Y and Z bias coils are wound from 121 and 81 turns respectively of 24 AWG square cross section wire (MWS Wire Company p/n 69287). The Y Bias coils are 25 × 50 mm center to center size and have a 6 mm square cross section, which gives a resistance of about 1.25 Ω per coil. The Z bias coils are $66 \times 72mm$ center to center and have a 5 mm square cross section, with about 1.4 Ω per coil. In the case of bias coils we are less concerned with the geometry, as the maximum field required from either coil is about 60 Gauss at the position of the atom chip. Slight curvature to the field may be ignored, provided that curvature is small compared to the size of the trapping region of the atom chip. We required a total field variation from the coils of less that 0.5 G/cm at the chip. Also, since the Y and Z bias coils are meant to be driven in series with a single power supply the target resistance per coil is slightly lower.

The holding frame of the coil is made from 6061-T6 aluminium, which has been anodized black to minimize optical reflection and to mitigate electrical shorting between different parts of the assembly. As can be seen in the exploded view of the coil assembly, figure 6.4(a), the top and bottom coil frames meant to hold the Z bias coils are made with a small slit on one side to prevent eddy currents around that part. The coils are epoxied to the frame with Epotek OD2002, a high temperature epoxy with good adhesion qualities to both the anodized aluminium and the polyimide on the outside of the coils. The coil frame is made to slide over a set of 4 stainless steel rails that are mounted to the base of the cell as shown in figure 6.4(b), making it a trivial matter to remove and replace the coils.

6.3 Chip connectors

A surprising headache in the development of the compact multi chamber system was the electrical connection to the atom chip. While this seems like it should be a trivial problem, given the sheer volume of connectors that are made for conventional electronics, the atom chip presents some new challenges. Specifically, the connectors must be compact, low profile, able to support the current loads required for experiments, and must gentle enough to insert that the experimenter will not damage the atoms chip plugging it in. In our early efforts with single sided atom chips connectors were soldered onto the chip before vacuum processing. However, as the chambers matured and we were able to bake at higher temperatures neither the connectors or the solder joints could survive bakeout. Soldering to the chip after bakeout is rather risky, as stress from local heating can cause the anodic bond or the chip itself to crack. Also, having switched to a gold backside metalization makes soldering even more difficult since standard tin based solder tends to form an brittle intermetallic joint when used with gold [102]. The alternative approach we took was to use a silver based electrically conductive epoxy (Epotek E2101) with a surface mount connector header (MilMax p/n 399-10-014-00-310-000). For mechanical stability this connector is potted to

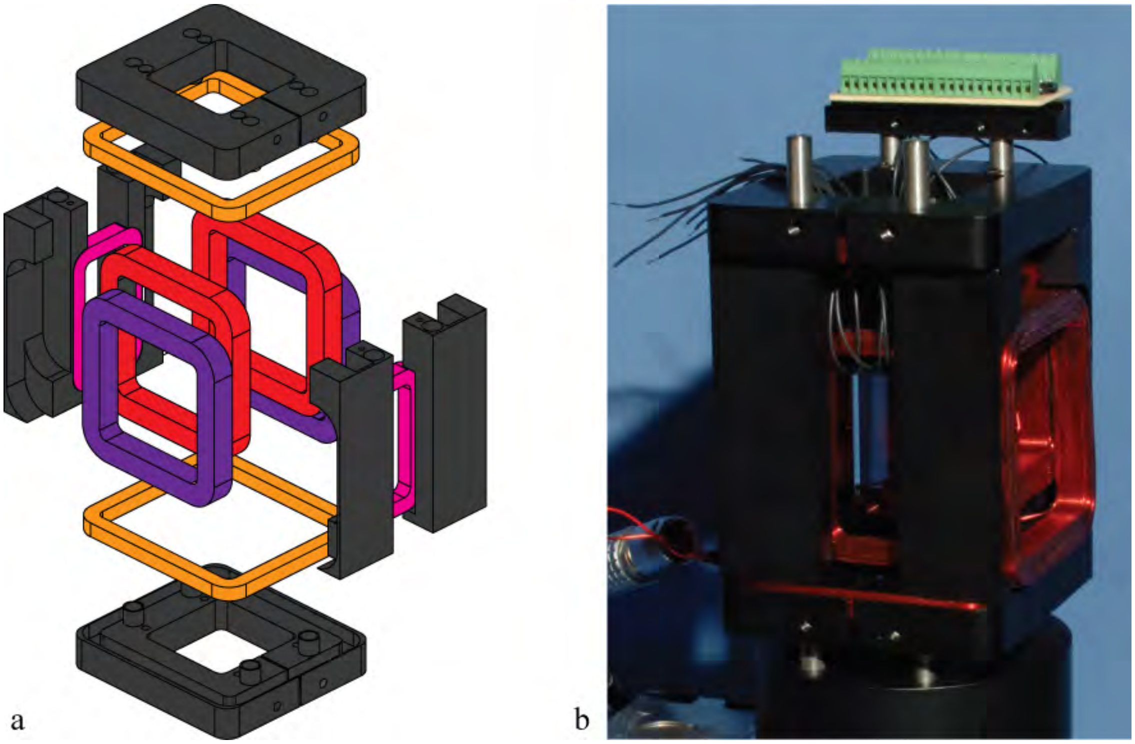

Figure 6.4: (Color). V2 coil assembly. (a) exploded view of the assembly showing all four coil pairs. (b) Coil assembly shown in place around a cell. The green connector header shown at the top of the page is the break-out assembly for connecting to the atom chip.

the chip surface with a very compliant epoxy (Epotek OD1001). The atom chip with connectors is show in figure 6.5.

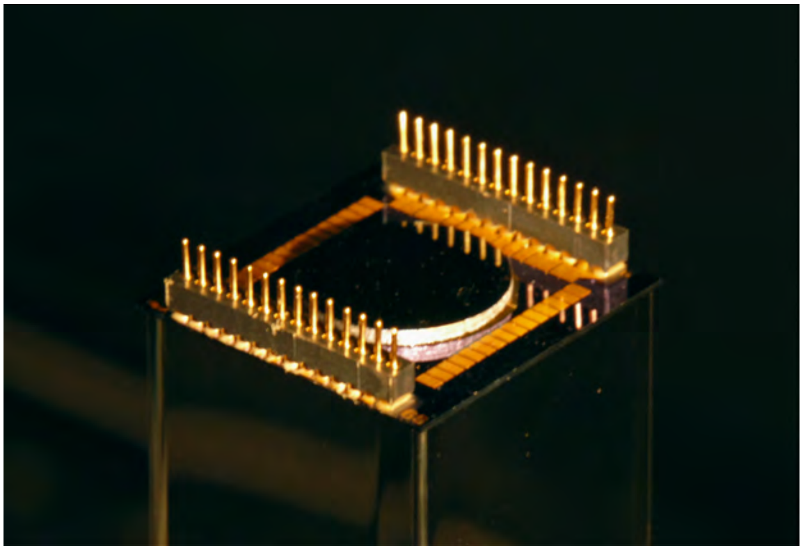

Figure 6.5: (Color). Standard atom chip connector used with the atom chip shown in fig. 4.12(c).

The cells used in the atomtronics experiments to date are nearly identical to our standard BEC cell, with the primary exception being the atom chip. Unfortunately, the connector scheme utilized on the standard atom chips sits several millimeters proud of the atom chip surface, which will interfere with most off the shelf microscope objectives. Rather than compromise our objective options we decided to develop a low profile connector alternative which would allow us to connect to the chip without interfering with the microscope system.

The chip connectors are glass frames, shown as a mechanical drawing in fig. 6.6(a), that are attached to the ambient side of the atom chip with epoxy. Wires can then be connected to the atom chip using conductive epoxy or colloidal silver, then potted in place. The frames needed to be made from an insulating material, otherwise the wires would short at the connector. Pyrex was chosen as the material of choice because it is thermally matched to the silicon and the glass cell, which will minimize stress due to differential thermal expansion on the chip. The frames are epoxied to the chip with a thin layer of Tra-Con 2115 Epoxy, which is an optical epoxy that is designed for very low shrinkage and will cure at room temperature. The wires used to make the connection are

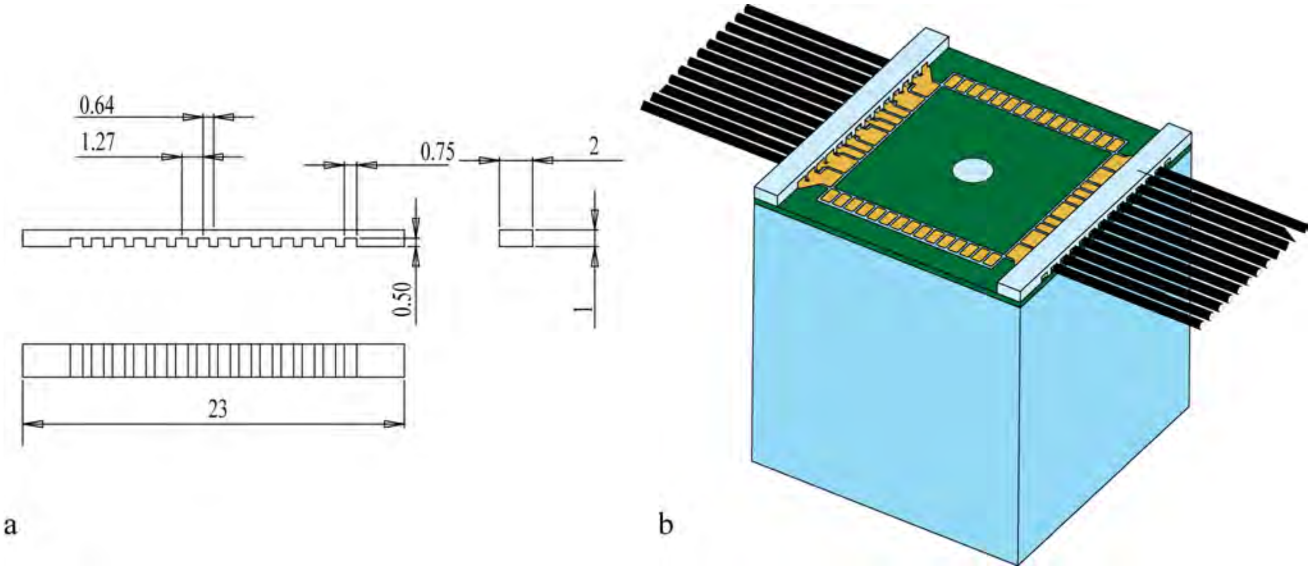

Figure 6.6: (Color). (a) V1 Window atom chip, image taken on the vacuum side of the chip. (b) V1 atom chip layout, shown in x-ray view. Ambient side metallization is shown in green, vacuum side metallization is shown in red. The location of glass regions on the chip is indicated in light blue.

28 AWG ultra-flexible silver plated wire from Cooner Wire Company(Cooner p/n: 155-28 BLK). This wire was chosen to minimize stress placed on the chip due to handling of the wires and to minimize vibration coupled to the atom chip through the leads. Each wire is cut to length then stripped at both ends. The chip side of the wire is coated in colloidal silver than inserted into the groove in the connector frame. Once electrical contact is assured the wire is potted with Tra-Con 2115 epoxy and left to cure. While this approach is somewhat inelegant, it is simple and effective for this purpose. The complete assembly is shown schematically in fig. 6.6(b).

6.4 Power supplies

The atomtronics system requires a large number of programmable current sources. These can be broken down into two categories: supplies to drive the coil assembly, and supplies to drive the atom chip. Although the chip trap experiments require excellent stability in both the chip currents and the bias fields, the coil drivers are the less demanding of the two supplies. This is not entirely obvious, given that it was shown in equation 4.8 that the trap frequency was proportional to the square of the bias field, but linearly proportional to the current in the chip ($\omega \sim B_0^2/I$). However, the coils have the advantage of being inductive loads, which acts as a filter for high frequency noise in the coils, and thus reduces the required servo bandwidth for the current supply. Additionally, the coils are much less fragile than the atom chip, which reduces the safety requirements for the supply. We have found that off the shelf linear bipolar supplies from Kepco (BOP20-10, BOP36-12) are a good choice for coil drivers. Unfortunately, the inductive nature of the coils is not without its drawbacks: the BOP supplies are unstable when used to drive inductive loads, so it is necessary to slow down the servo to prevent the supply from ringing. We do this by adding a Zobel network in parallel with the coil as described in [24].

We have found that off the shelf supplies are not well matched to the problem of driving the atom chip currents. For this we have built current servo loops that supply chip currents with power op-amps. A schematic circuit layout is shown in figure 6.7. The supplies are powered with sealed lead-acid batteries, which minimize noise introduced to the servo from dirty power lines.

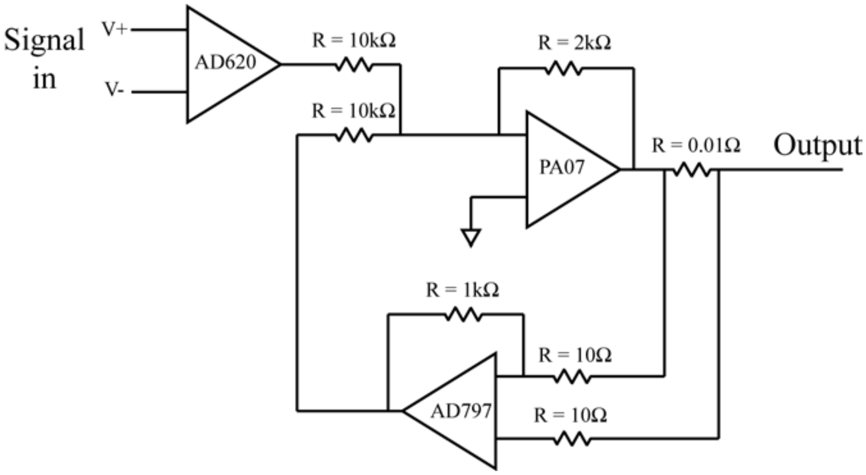

Figure 6.7: Chip driver schematic

A major concern with the atom chip drivers is protecting the chip. Although the chips are quite robust, it is possible to overheat the chip and burn out wire traces. To protect the atom chips Daniel Farkas and the JILA electronic shop have developed an electronic fuse system, which is effectively a leaky integrator circuit that triggers a relay switch when too much power has been dissipated by the chip. The electronic fuse mimics the behavior of the atom chip heating and cooling as current is run through the chip wire: As current is run through the chip the electronic fuse charges, and when the current stops the fuse slowly discharges. The heating and cooling rates are experimentally determined by setting rise and decay constants of the electronic fuse circuit. This approach is preferable to a conventional fuse that can cool down much faster than the atom chip, which will make it possible to burn out the chip with modest currents run at a high duty cycle.

6.5 Control system

The experiment is run from a series of digital to analog converters (DAC) and digital input/output (DIO) modules, which are controlled from a computer. Direct control of the experiment from a desktop computer is certainly possible, but it is desirable to decouple the control interface from the instrument running the experiment since desktop computers tend to be unreliable for precision timing applications. The architecture for our control system is shown in figure 6.8.

The timing file is programmed by the user at a desktop computer in a National Instruments Labview environment developed in our group by Farhad Majdeteimouri. The computer outputs a timing file which is then read into an embedded controller using Labview Realtime. The controller in turn programs and triggers an 3M Gate field programmable gate array (FPGA) (National Instruments PXI-7813R). The FPGA has the advantage of being able to synchronize all of the control signals relative to a single clock on the FPGA. The output signals that require analog signals, such as the magnetic fields and RF frequencies, are controlled from DACs (National Instruments 9263 and 9264) which receive their digital signals from the FPGA. Digital signals (shutters, camera triggers, etc.) are controlled from a DIO module (National Instruments 9403).

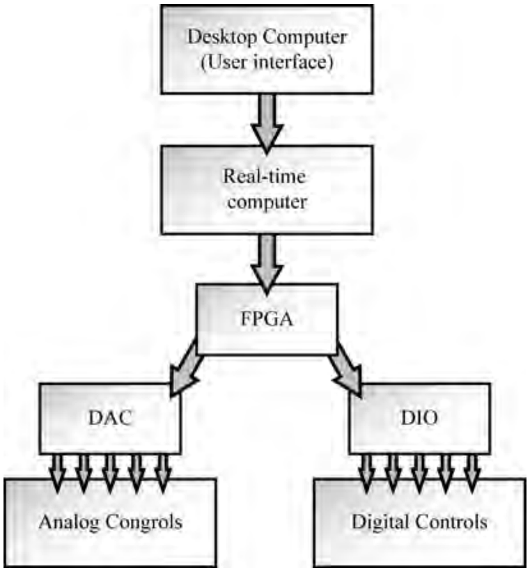

Figure 6.8: Control system schematic

As was shown in [24], careful choices of grounding connections to the control system can substantially reduce the total amount of signal noise that the instruments receive. All of the DAC channel outputs are differential voltages that are electronically floating relative to earth ground and relative to the FPGA signal. We ground the chassis of the control system output and that serves as a central grounding point for the entire experiment. To mitigate problems with ground loops the instruments controlled by the DACs are all floating and receive their ground connection through the DAC control lines. In cases where it is impractical to float the instrument we isolate the DAC from that device by using an instrumentation amplifier (Analog Devices AD620), which keeps the noise from that device from affecting the other channels. To minimize pickup all of the analog connections are made with shielded, twisted pairs of 26 AWG wire with shielded connectors wherever possible.

6.6 RF system

The RF system used for evaporative cooling of atoms consists of a commercial RF synthesizer (Agilent p/n 33250A) which is frequency modulated with an analog input from the DAC. The output from the synthesizer is passed through an RF switch (Mini-Circuits p/n ZYSW-2-500R), a voltage controlled attenuator (Mini-Circuits p/n ZX73-2500+) and a 2 watt amplifier (Mini-Circuits p/n ZHL-1-2W-SMA). The amplified RF signal is fed into a 1 cm diameter loop of wire which is held behind the atom chip. We attempt to impedance match the RF loop to the amplifier by placing a 50 Ω resistor in series with the loop. This significantly decreases the RF power reflected back into the amplifier and couples a larger percentage of the available power to the atoms.

6.7 Opto-mechanical system

All of the BEC systems we have built use a secondary optical platform to support the optics for the MOT in the BEC chamber. Originally, in the single chamber system, this was done because the chamber was fairly tall. Having a platform eliminated the need for optics on extremely tall posts, and allowed for removal and insertion of vacuum chambers without needing to remove and re-align all of the optics in the experiment. When we switched to a double MOT chamber it became necessary to have two sets of MOT optics, one for the 2D MOT and one for the 3D MOT. Here again it was useful to have a platform which now allowed for two separate sets of optics. The integrated physics package that was central to the portable BEC system [71] followed the same basic architecture, but as there was no optics table for that system it employed four levels: a base, a 2D MOT level, a cell holding level, and a level for the 3D MOT and imaging. The portable system is very elegant, but there is not a lot of room for additions of optics to the system. This is fine if the only goal is to produce BEC and do experiments that only employ the atom chip, but is not ideal if more flexibility is required. Also, it was extremely expensive to produce. A sampling of the earlier designs is shown in figure 6.9

The platform designed for the transistor system incorporates many of the best features of the previous generations. Most notably is the lack of optics on the top surface, as can be seen in figure 6.10(a). The table was designed to maximize flexibility, which meant leaving as much free space available as possible. This allows the experimenter to focus on the science and ignore the troubles associated with production of coherent matter. Fig. 6.10(b) shows the atomtronics system with the microscope assembly for through-chip imaging and projection in place.

The heart of the atomtronics opto-mechanical system is our standard two chamber BEC cell described in chapter 3, and all of the optics are designed around that form factor. It should be noted that standardizing in this way dramatically reduces the down time for experimental changes, such as switching out vacuum cells. In our most recent chamber swap less than a week elapsed from when a new cell went into the apparatus to the time when we were producing BEC on the chip and were ready to start experiments.

6.7.1 2D(+) MOT optics and magnets

The 2D(+) MOT is completely separate from the rest of the optics in the system. The 2D(+) MOT optics are much simpler than the 3D MOT, as there are fewer beams and all but one are in the same plane. The layout for the 2D(+) MOT optics is shown in figure 6.11. This layout

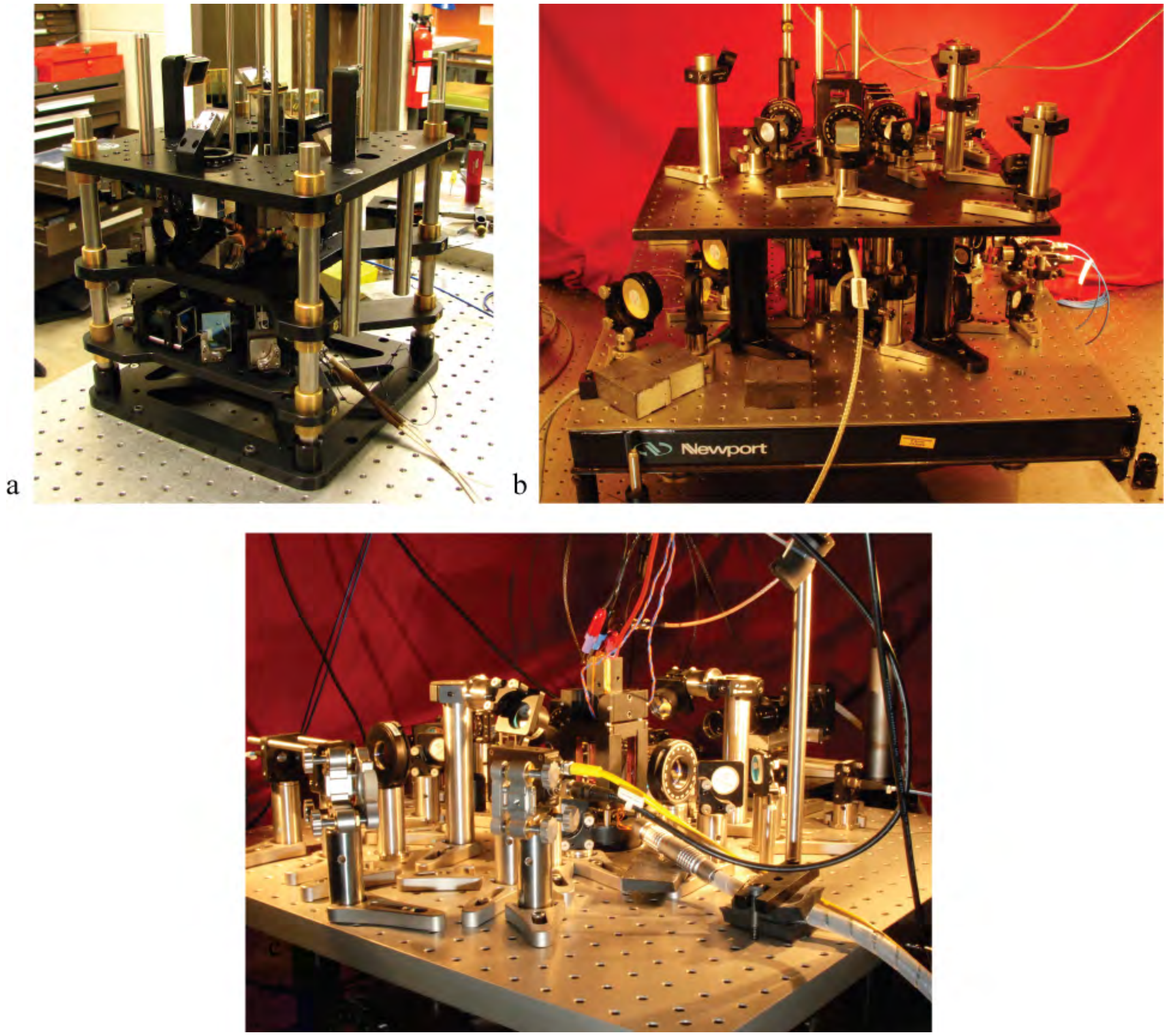

Figure 6.9: (Color). Optics packages for double MOT BEC cells. (a) Compact optics package for portable applications, described in chapter 3. (b) Optics assembly for the gyroscope system. The system is designed to sit on an air bearing for rotation measurments. See [24] for details. (c) V1 atomtronics optics package for use with the nano-chips described in the first half of chapter 5.

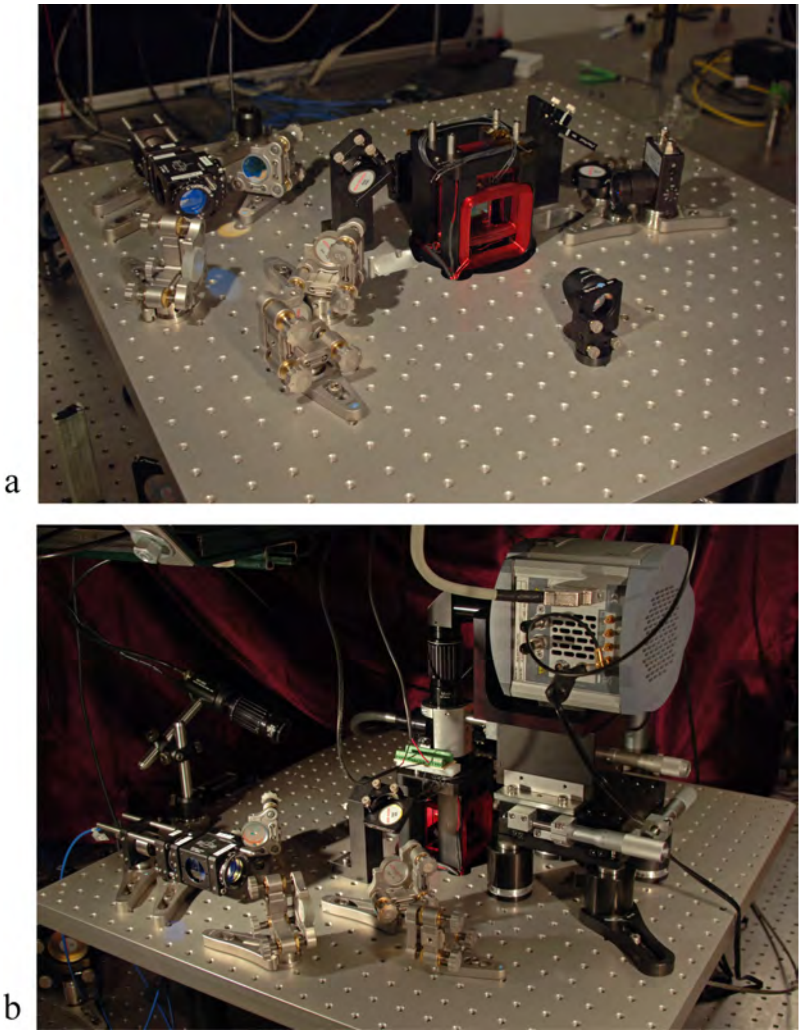

Figure 6.10: (Color). (a) Final version atomtronics opto-mechanical setup. All of the optics needed to produce and image BEC in the cell are present in photograph, including some optics in place for an additional experiment. (b) Atomtronics opto-mechanical setup shown with microscope in the system

is done directly on the main optics table. The 2D(+) MOT requires cooling and repump light, both of which may be at the same frequencies as the 3D MOT. We have found, as have other groups [64], that the highest output flux from the 2D(+) MOT is achieved when the cooling light in the 2D(+) MOT is detuned approximately 3Γ red of the cooling transition. However, leaving the cooling laser detuned at 2Γ to the red of the transition for both MOTs significantly reduces the complexity of the laser system and is not a dramatic sacrifice in the 2D(+) MOT flux. In our experiment we have 250 mW of cooling light and 20 mW of repump light out of the optical fiber. The cooling and repump are launched from two separate fibers and collimated with two $f = 75$ mm achromatic lenses, and are then overlapped with a 1" polarizing beamsplitter cube. The bulk of the light passes through a cylindrical telescope, which expands the beam to an overall size of about 15×35 mm. This light is split with a larger PBS and aligned through the MOT cell at right angles. The beam polarizations are circularized with 2 quarter-wave retarders and then each beam retro-reflected with a quarter waveplate/mirror combination optic. Some of the light is split off from the overlap PBS and aligned through a periscope, half wave plate, 2 mirrors and a PBS. The last PBS is in place to make it possible to adjust the power to the push beam without changing the power in the 2D MOT. The push beam is critical to achieving a high output flux from the 2D(+) MOT, and will typically increase the flux of the pure 2D MOT by at least a factor of 10.

The magnetic fields for the 2D(+) MOT are generated with a set of 4 permanent magnet groups held in the configuration shown in figure 6.12(a). The magnet strengths and spacing are chosen so the field gradient at the center of the assembly is approximately 20 G/cm, which gives the optimal output flux. To optimize the coupling between the 2D(+) MOT and the 3D MOT in the BEC chamber it is necessary to align the MOT with the silicon Pinhole separating the two halves of the vacuum chamber. This is achieved by mounting the 2D MOT magnets on a custom made, low profile translation stage shown in figure 6.12(b).

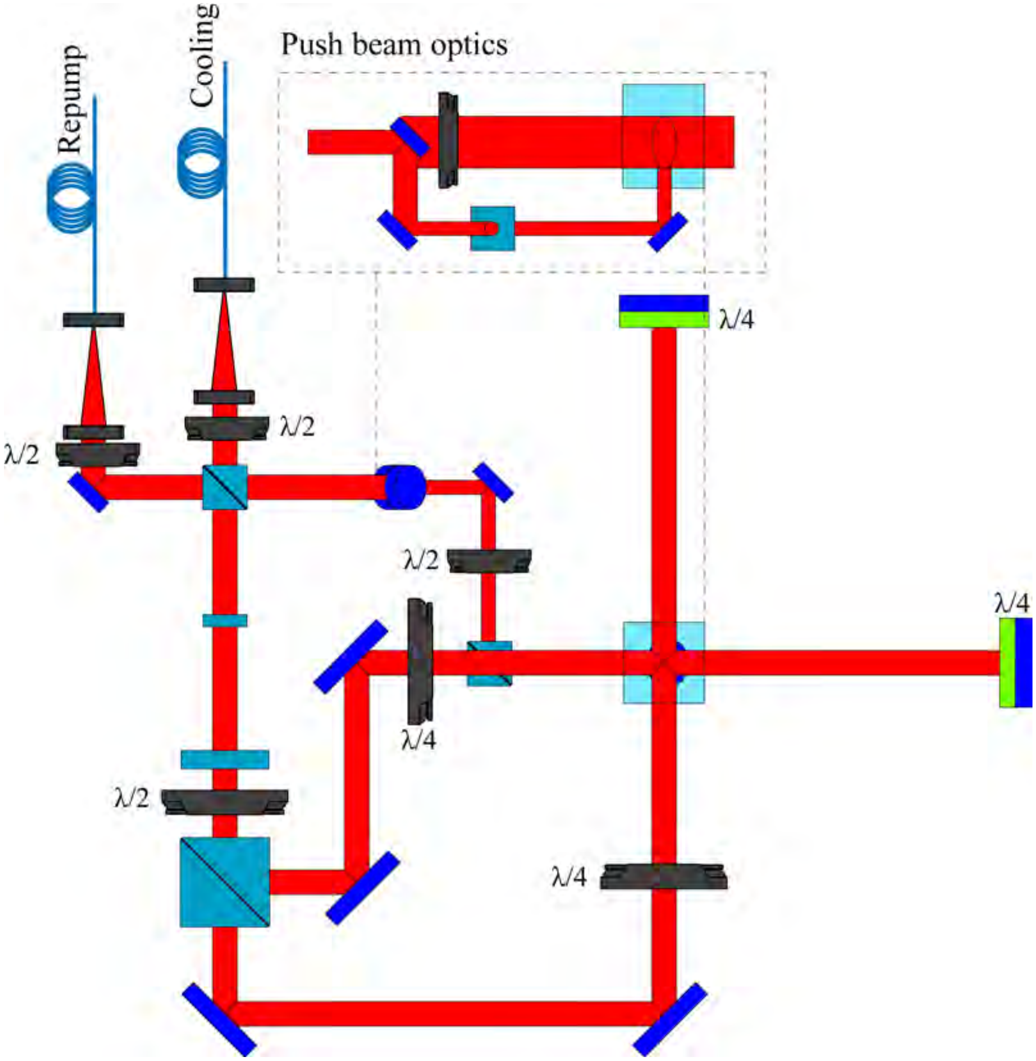

Figure 6.11: (Color). Layout drawing for the 2D(+) MOT optics

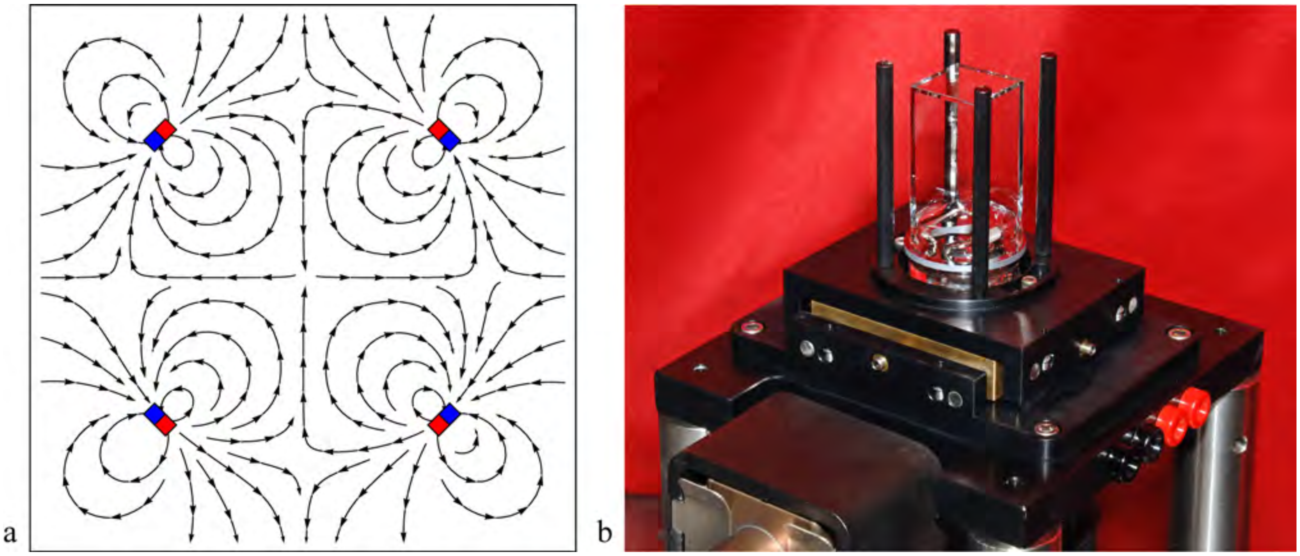

Figure 6.12: (Color). (a) Magnetic field from a set of four magnets in the 2D MOT configuration. (b) Magnet assembly for the 2D(+) MOT shown in place over the 2D MOT cell.

6.7.2 3D MOT optics and experiment platform

The clean tabletop shown in figure 6.10(a) is achieved by moving optics underneath the table whenever possible. The underside layout for the six beam MOT and optical pumping is shown in figure 6.13. Light from the laser system is brought to the table with three fiber optic patch cords: one for the cooling, one for the repump and one for the pump. The beams are collimated with $f = 75$ mm achromatic lenses, and then overlapped with polarizing beam splitting cubes. The beam path for the cooling light is split into four paths before being sent vertically through the table into the MOT. Each beam passes through a half wave plate and a quarter wave plate before it is sent through the cell. This is not crucial, but since the mirrors in the system are made with dielectric coatings it can be assumed that the reflections will introduce some elipticity to the beam polarization, which can be compensated for with the wave plate pair.

The vertical beam paths are shown in fig 6.14. Fig 6.14a shows the angled beam path through the cell. The beam angle is chosen to be 22.5 degrees above the horizontal plane rather than the usual 45 degrees. This shallow angle allows the MOT to be produced closer to the atom chip without a significant sacrifice to the atom number [23]. The angled beams are retro-reflected with a quarter wave plate and a mirror held in a mirror mount underneath the table. In contrast to the 2D(+) MOT, the 3D MOT has a significant optical thickness, which results in a hole in the beam. This makes the retro-reflected beam path a less than ideal choice as it results in a differential pressure on the atoms in the MOT, but it significantly reduces the complexity of the optical setup. The horizontal beam path, shown in 6.14(b) is split into two separate beams. This allows the optical pumping light, shown in dark red arrows, to be overlapped with one of the MOT beams and to pass through the cell in only one direction, which is necessary for optical pumping to work correctly. The MOT and optical pumping require only four optics on the top side of the table, leaving a tremendous amount of space to set up other optics.

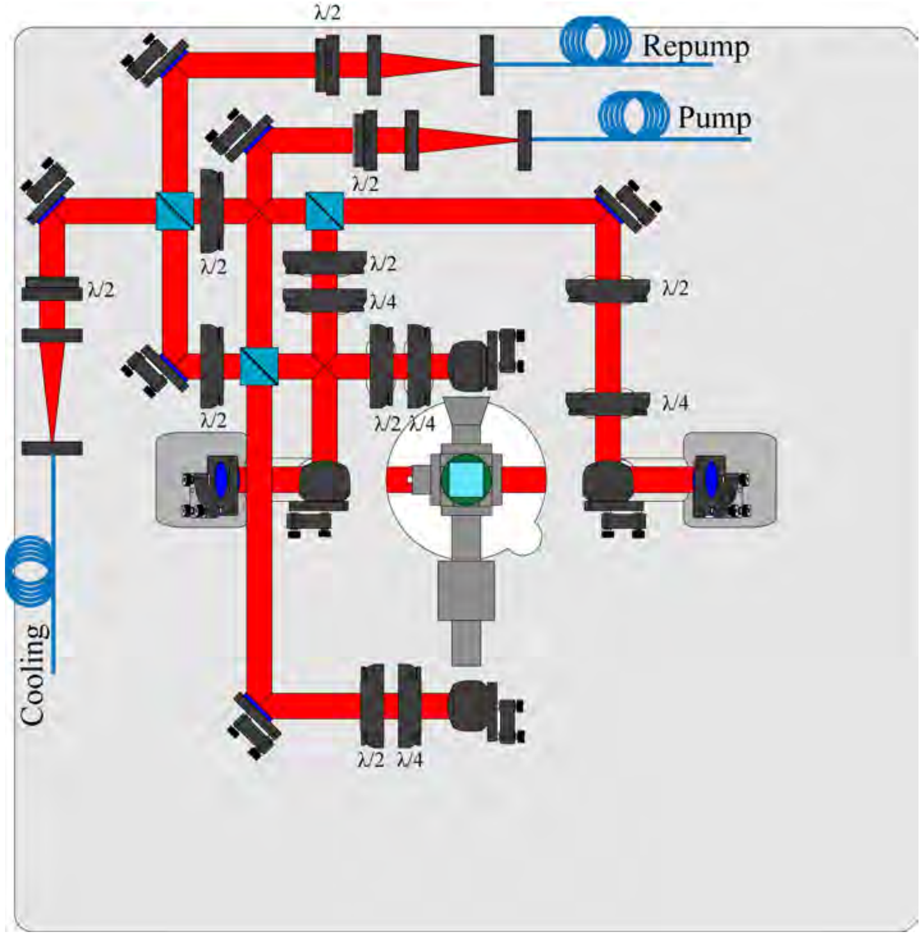

Figure 6.13: (Color). Bottom view of atomronics opto-mechanical setup.

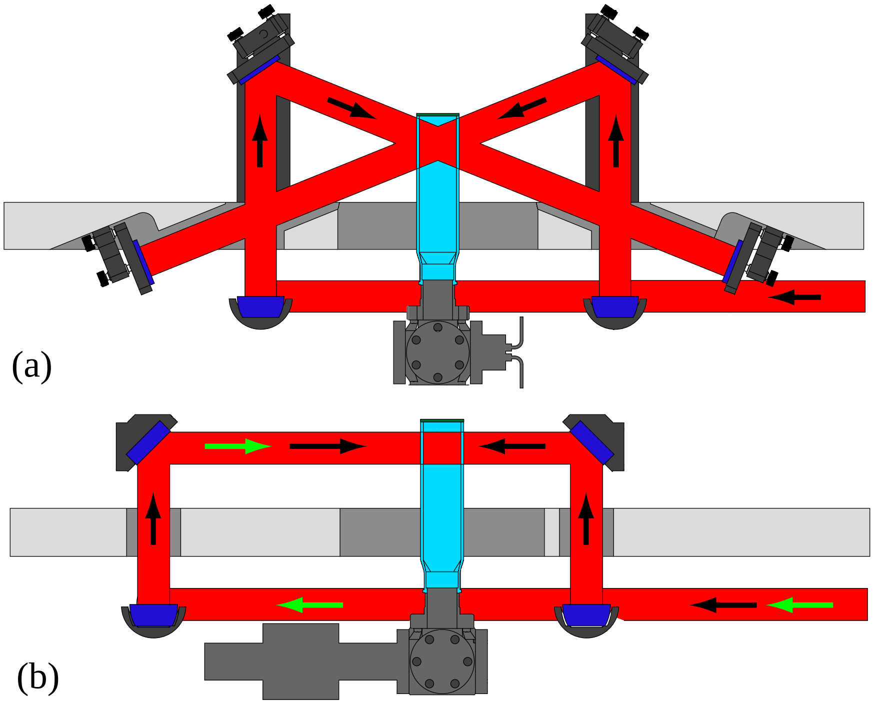

Figure 6.14: (Color). Vertical beams in atomtronics opto-mechanical setup. (a) Angled beams path through the cell. (b) Horizontal beam path through the cell. Overlapped probe beam path is shown in green.

6.8 Imaging systems

There are two imaging systems in the atomtronics apparatus. The first is the absorption imaging system, which uses the conventional approach to imaging of Bose-Einstein Condensates. The second is the microscope fluorescence imaging and projection system, which was introduced in chapter 5.

6.8.1 Conventional absorption imaging

In most BEC machines the only means of detecting the condensate is with absorption imaging of atoms. The imaging procedure is fairly simple: the atoms are released from the trap, allowed to freely expand for some finite amount of time, and then pulsed with laser light resonant with the cycling transition. The atoms leave a hole in the beam and the light is imaged onto a detector. It is difficult to extract information directly from the single absorption image, as the image also contains all of the other information in the laser beam, such as structure from an imperfect mode or scattered light. The image may be normalized by taking a second picture without the atoms and subtracting the two images. Optical density of the atomic sample is calculated as

$$\mathrm{OD} = \ln\left(\frac{I_{background}}{I_{atoms}}\right). \tag{6.6}$$

To collect the light and focus the image onto the camera we use a Infinity Photooptical KC series long working distance microscope with a IF-3 objective that gives a resolution of about 3-4 μm at a working distance of 150 mm. Used with a doubling tube we work at a magnification of 2.5 μm per pixel, which is slightly below the resolution limit of the lens.

The absorption imaging camera is a Basler A102f. We have found that this compact firewire camera works extremely well for absorption imaging. Contrary to popular belief, the top of the line scientific cameras with high quantum efficiencies and extremely low noise backgrounds are not necessarily the right choice for absorption imaging. Most of the high class cameras available have been manufactured for biological and astronomical applications, where the goal is typically to detect as few photons as possible with the highest fidelity possible. This sort of camera is optimal for fluorescence imaging, as we will discuss in the next section, but in the case of absorption imaging one is typically trying to detect a reasonably large change out of a large number of photons. Our experience has shown that a far bigger source of noise is shot to shot variations in the optical field, caused by small motion of scattering objects during the imaging pulse. This is a particularly bad problem in our atom chip systems, as the heating of the atom chip causes the chamber to expand slightly which results in fringe noise in the OD image. Fig. 6.15(a) shows OD noise of about 0.4 on an absorption imaging sequence without atoms present. The best way we have found to reduce that noise is to decrease the time between the image of the atoms and the image without. To achieve this a fast camera is preferable to a slow, low noise one. As can be seen in figure 6.15b, decreasing the time between shots from 3 ms to 300 μs dramatically reduces the fringe noise to less that 0.1 OD.

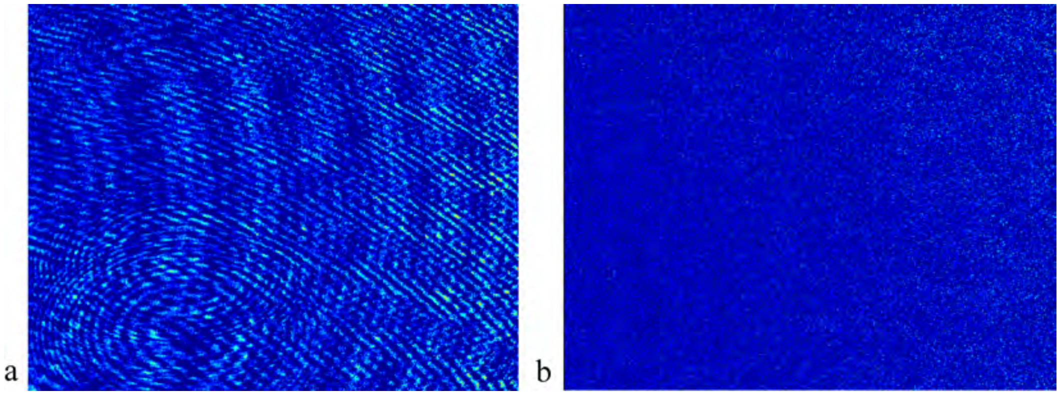

Figure 6.15: (Color). Fringe reduction due to increased camera speed. (a) OD plot from 3 ms between the absorption and background images. (b) OD plot with 300 μs between the absorption and background images.

Taking those two images so close can lead to problems with detecting the atoms, because in such a short time the atoms have not had time to fall out of the picture. We attempted to solve this problem by unlocking the laser and pushing it off resonance between shots, but the change in laser frequency also changed the fringe pattern between shots, making the image even more noisy. Instead we apply a bias field of about 30 G along the imaging axis which Zeeman shifts the atoms about 7 linewidths off of resonance, making the atoms transparent to the second pulse.

6.8.2 Microscope imaging system

Because of the geometry of the chamber absorption imaging of the atoms through the atom chip was not a readily available option. We have considered adding optics to the chip surface, similar to the mirrors in fig. 5.8, to allow a beam from the side to be aligned into the microscope. However, a simpler option is to use fluorescence imaging. Fluorescence imaging is a less common than absorption imaging for detection of Bose-Einstein Condensates primarily because of photon collection. With absorption imaging nearly all of the photons scattered out of the beam are measured as part of the signal. In the case of fluorescence imaging the only photons detected are the photons scattered into the principle lens of the imaging system. For an imaging system with a numerical aperture of 0.1 only about 0.2% of the photons will be collected in the system. For a rubidium atom scattering as many photons as possible in a 20 μs pulse of light this corresponds to only 0.3 photons per atom that even reach the first lens. However, the number of photons collected will increase as the square of the numerical aperture, so at an N.A. of 0.6 it would be possible to collect 12 photons per atom in a 20 μs pulse. Also, if a large enough signal is possible fluorescence imaging is preferable to absorption imaging for detecting small atom numbers. This is because the background noise level is determined only by technical noise and stray light, where the background noise of absorption imaging is dominated by photon shot noise [103].

The microscope system is, by design, made almost entirely from commercial components. This is in contrast to the work done in the labs of Markus Greiner, Imanuell Bloch, David Weiss, and Jorg Schmedmayer [94, 95, 6, 103]. One of the drawbacks of those experiments is that they rely on objectives that are custom tailored to their experiments. While this is a great approach for achieving optimal performance, it drives up the cost and significantly limits the flexibility of the system. The window chip apparatus, on the other hand, allows the experimenter to use commercially available optics. In our experiments the glass separating the atoms from the outside world is only 420 μm thick, which is consistent with standard cover glass correction thicknesses for microscope objectives targeted at the biological microscopy community. Also, all of the optics except for the window are out of vacuum. If we wish to change out the microscope objective in our system it can be done in just a few hours.

There are, however, certain drawbacks to the window chip system. Thus far we have not applied anti-reflection coatings to any of our window chips, which will reduce the transmission of light through the system, and will leave the system more susceptible to etalon effects between the faces of the window. Also, the window itself is not very flat: The polishing process used to fabricate the compound substrate wafers polishes the glass and the silicon at slightly different rates, leaving a surface ridge between the two materials and a residual curvature on the glass surface. This can be seen clearly in an interferometrically obtained surface profile of a 3 mm window shown in fig. 6.16. The curvature of the surface will cause the window to act as a lens with a focal length of about $f \sim 850$ mm. Finally, as the chip is under vacuum, it can be assumed that that pressure will cause the window to deform and will introduce stress in the glass, which can cause other optical problems, such as an induced birefringence in the glass. We do not know how much of an issue this is, as we have not yet done any careful measurements of the atom chip's optical performance when the system is under vacuum.

The heart of the imaging system is the camera. We use an Andor Ixon DU897 Electron Multiplying CCD (EMCCD) camera. The camera is extremely well optimized for low light imaging: The quantum efficiency at our wavelength is 72%, something achieved by using a back illuminated CCD. The detector can be cooled to temperatures as low as $-100°$C, which eliminates almost all dark counts. The readout noise, which is the dominant noise factor on most conventional CCD cameras, is overcome by the electron multiplying feature of the CCD. The EMCCD works by moving the charge on each pixel through a multiplication register before it passes through the readout amplifier. This process amplifies the signal from the detector in a way that introduces only stochastic multiplication noise [103]. The electron charge is then converted to a readout voltage, but the charge signal is now large compared to the readout noise, improving the overall signal to noise of the device. The limiting noise factor of the camera is clock induced charge (CIC) which is

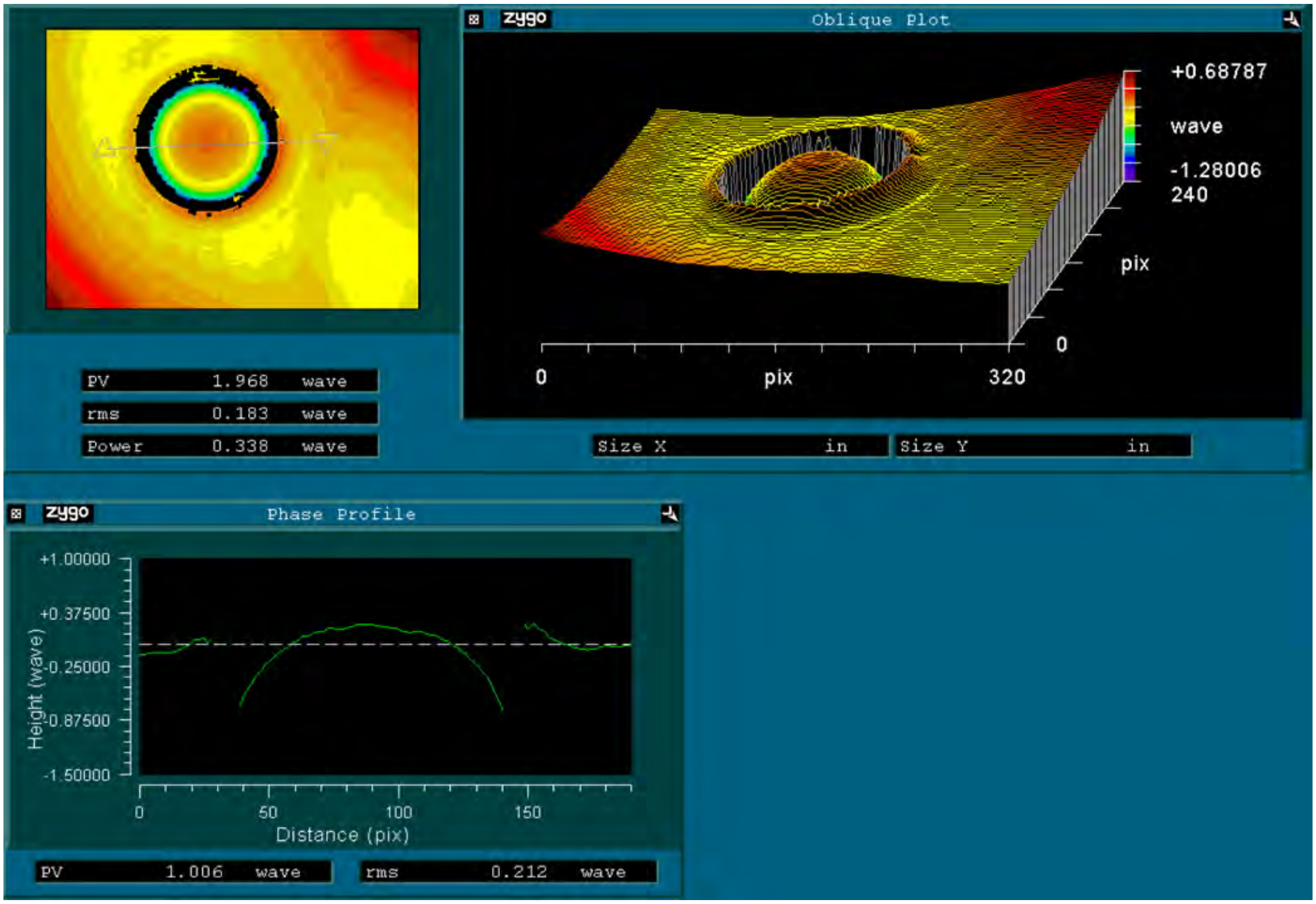

PV 1.968 wave

rms 0.183 wave

Power 0.338 wave

Size X in

Size Y in

PV 1.006 wave

rms 0.212 wave

Figure 6.16: (Color). Surface profile of the atom chip window. Units are standard optical length units of 1 wave = 632 nm.

charge build up that accumulates as the signal charge is moved to the EM register. If used correctly it is possible to detect a florescence signal from a single atom [94, 103].

We have so far used 2 microscope objectives in this system. The first was a Nikon M Plan 40x objective with an NA of 0.55. This objective was chosen because it was close to what we had in mind, and we had one in the lab. This was not an ideal choice for several reasons. The objective is not corrected for a cover glass, which makes it non-ideal for our imaging situation, and it was not well optimized for fluorescence measurements. That objective was replaced with a Zeiss LD Plan Neofluar, which is a 40x objective with an NA of 0.6. This objective is designed to correct for cover glass of thicknesses from 0-1.5 mm. Additionally, the objective is designed for long working distance operation and is optimized for florescence imaging, with a transmission of more than 80% at 780 nm. The importance of the cover glass correction can be easily seen in figure 6.17, which shows pictures of a memory chip with a $3\mu\text{m} \times 8\mu\text{m}$ rectangular grid with glass in place but no correction (a) and with cover glass and correction correctly aligned (b).

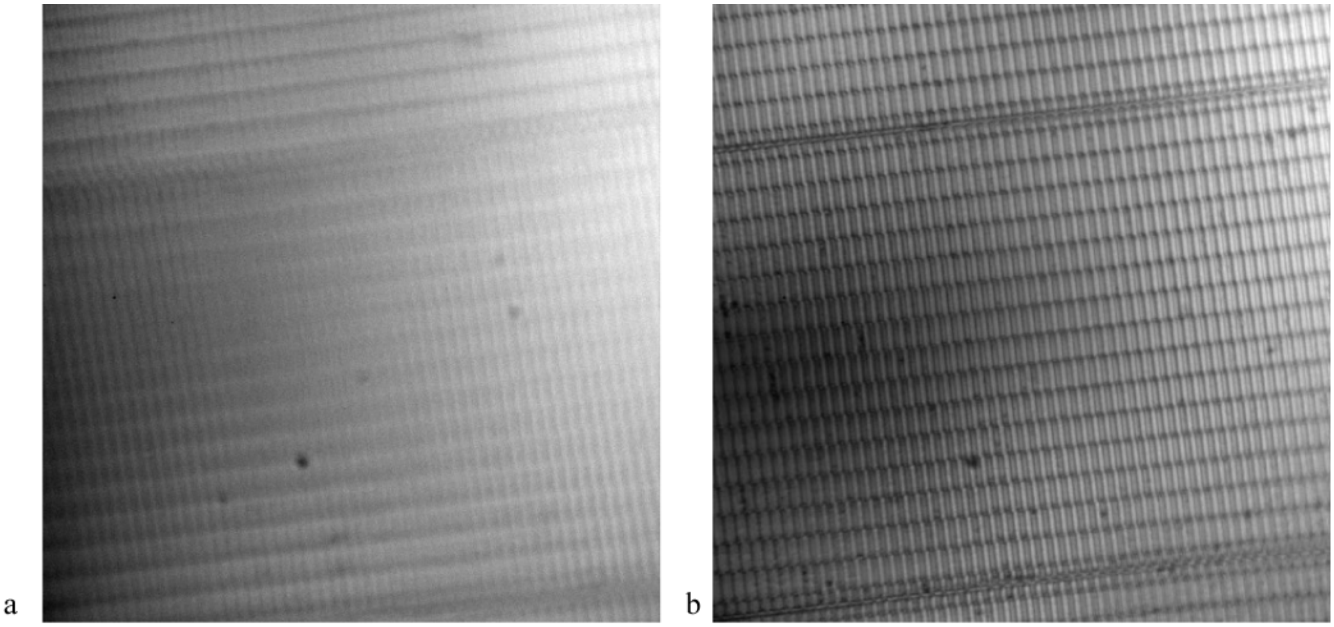

Figure 6.17: (Color). Effects of microscope objective cover glass correction. (a) Image of a memory chip with $3 \times 8\,\mu\text{m}$ features. Image is taken through a 420 μm thick window without any cover glass correction on the microscope objective. (b) The same object shown in (a), but with the cover glass correction correctly aligned.

The microscope objective is connected to the camera using an Infinity PhotoOptical KC series lens tube with a coaxial illuminator port. The lens assembly is a simple condenser to project the microscope image onto the CCD detector. The illuminator port assembly includes a plate beam splitter, where the projection optics will ultimately be aligned into the system.

In most optical microscopes the target is moved relative to the objective to align and focus the image. In our case this would be difficult, as it would involve moving the cell and all of the optics, so we chose to make our microscope moveable. The microscope assembly sits on a 3 axis stage, built from commercially available translation stages. The horizontal motion is given by a Optosigma 123-0400 crossed roller bearing XY stage, which gives us 40 mm of travel in each direction, with about 5 μm precision. The vertical motion is provided by a Newport MVN80 precision ball bearing vertical linear stage with a standard micrometer, which gives 12.5 mm of travel and precision of 1-2 μm. The assembly is shown in fig. 6.18. The microscope assembly is held together with a few custom made brackets. The bracket design over constrains the lens assembly, which pulls the long microscope tube into traction keeping it stable during operation. We fill the space between the bottom of the camera and the L bracket with a layer or sorbothane to help damp out vibrations.

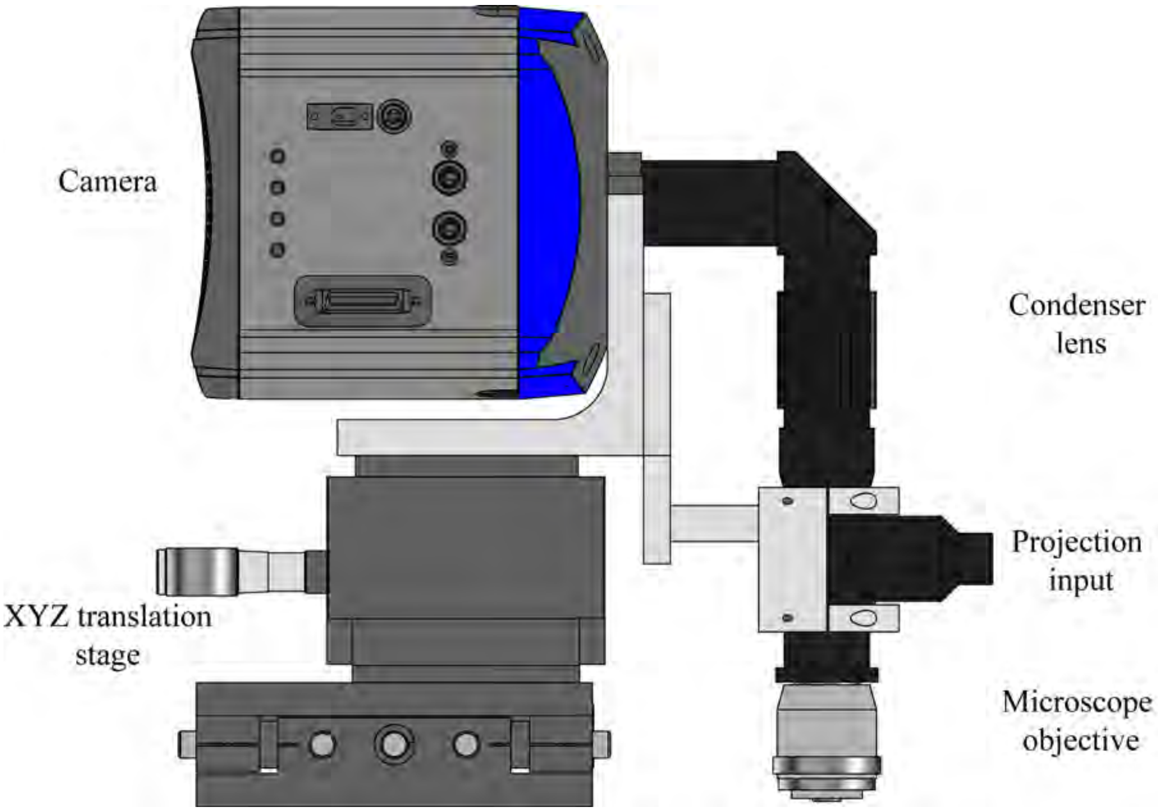

Figure 6.18: (Color). Microscope system for atomtroncis experiments.

Chapter 7

Experimental procedures and results

In this chapter we will present the details of the BEC production process, and the results from the first two window chip cells. The first cell was built with the V1 window chip shown in fig. 5.9. The purpose of this chip was to demonstrate that it would be possible to do BEC experiments on a chip with wire traces over a window. The chip traces were to carry a current density as high as 5×10^9 A/m^2, which is common practice for our lab, but usually the wires are in close thermal contact with silicon, which has a thermal conductivity of ~ 100 W m^{-1}K^{-1}. Over the window the traces are in thermal contact with glass, which has a thermal conductivity of ~ 1 W m^{-1}K^{-1}. We could expect the wires to get much hotter than they had in previous chips, and it was important to show that this technology would be robust enough for cold atom experiments.

The second cell was built with the V2 window chip shown in fig. 5.17. This chip is designed to be used for tunneling and transistor experiments. We will present the preliminary imaging results with both chips and discuss our efforts to characterize the resolution of the imaging system.

7.1 BEC production process

The BEC production process we use has been developed over the past few years in our group and is described in the PhD thesis of Matthew Squires [23]. This section reviews the details of the process, including the specific parameters used in our experiments.

The production of BEC starts by loading a 6 beam MOT 15mm below the atom chip from a 2D(+) MOT. We typically load 7×10^8 atoms into the 6 beam MOT in about 3 seconds. The

2D(+) MOT has as much as 300 mW of cooling laser power available. 150 mW of the cooling power goes into two transverse cooling beams which are then retro-reflected, effectively doubling the cooling power in the MOT. 2.5 mW goes into the push beam. The remaining power is dumped out of the system. The 2D MOT employs 18 mW of repump laser power, which is overlapped with the cooling light using a polarizing beam splitter. The 6 beam MOT uses 50 mW of cooling power, equally split into four beams, two of which are retro-reflected to give a total power 75 mW into the MOT. The 6 beam MOT uses 10 mW of repump power. We have not made careful measurements of the characteristics of our MOT, but we expect that the cloud temperature is about 300 μK.

Once the MOT is loaded the 2D MOT is turned off and the atoms are compressed in a compressed MOT (CMOT) [104] by detuning the cooling laser 4-5 linewidths from the atomic resonance, and by decreasing the repump power to less than 100 μW. The field gradient is also adjusted to match the frequency detuning of the cooling laser. We obtain the best results with a gradient of 5.4 G/cm. The CMOT stage typically takes 15 ms. We do not loose a significant number of atoms between the MOT and the CMOT, and have usually increased the density of the cloud substantially and decreased the temperature to about 150 μK.

Next the atoms are further cooled with a 5 ms stage of polarization gradient cooling. In this step the laser is detuned 12 linewidths to the red of atomic resonance and all of the magnetic fields are shimmed to zero. The cooling power is also reduced during this stage to further decrease the photon scattering rate. We have seen temperatures as low as 8 μK after polarization gradient cooling, but we typically are satisfied with temperatures near or below 20 μK.

After the sub-doppler cooling the atoms are optically pumped using a laser tuned two linewidths blue of the $|F = 2\rangle \rightarrow |F' = 2\rangle$ transition. The laser is overlapped with one of the horizonal MOT beams, which is aligned to the $\hat{x}$ axis of the system. A bias field of 4.5 gauss is applied in the same direction, Zemann shifting the m_f sublevels of the two states. The optical pumping stage lasts for about 0.5 ms, and uses about 1 mW of light, plus light from the repump laser.

The atoms are then trapped in a quadrupole field generated by the MOT coils. The atoms are initially trapped in a field gradient of 62 G/cm. The current in the MOT coils is linearly ramped to zero while the current in the transfer coils is linearly increased to move the minimum of the magnetic field from the position of the MOT up to the level of the atom chip. Because the coils are highly overlapped this can be done without decompressing the trap which minimizes heating during transfer. At the level of the atom chip the atoms are in a linear trap with field gradient of 110 G/cm. We have transferred as many as 3×10^8 atoms to the chip level, although we typically transfer only about 1×10^8 atoms.

It is not possible to transfer adiabatically from a quadrupole trap to the harmonic IP trap on the atom chip. The best that can be done is to compress the trap to a gradient similar to the initial chip trap, and then snap the coils off immediately before turning on the chip trap. We increase the field gradient of the chip trap to 120 G/cm, then turn the coils off. It takes about $130\mu s$ for the coils to turn off. This speed is limited by the fact that the coils have an inductance of about 0.5 mH and the power supply can only source ±36 V. Once the coils are turned off the current in a Z wire on the chip and the Y bias are snapped on to 4.25A and 17 Gauss. The atoms are then compressed into the dimple trap for evaporative cooling. This is done by ramping the Z wire down to 2.6A and ramping the dimple wire, X bias and Y bias up to 1A, 17.5 Gauss and 40 Gauss respectively. This gives a trap with calculated trap frequencies of $\omega = 2\pi\times$(2.6 kHz, 2.5 kHz, 460 Hz), at a distance of 120 μm below the atom chip surface. We generally load 30×10^6 atoms into the dimple trap on the chip. The evaporative cooling process is performed with linear ramps of an RF frequency coupled to the atoms through an antenna located behind the atom chip. The RF frequency is ramped from 50 MHz down to a few hundred kHz above the trap bottom at 2.6 MHz. Because the trap is very tight the evaporative cooling can be performed in 800-1200 μs. After RF evaporation we achieve a BEC of 30×10^3 atoms.

It is difficult to image the atoms with absorption imaging in the tight evaporation trap as it is only 120 μm from the atom chip surface. To facilitate imaging we typically will move the atoms away from the chip and simultaneously loosen the trap by ramping the current in the X and Y bias fields to 20% of their original values while leaving the chip currents constant. This leaves the atoms in a trap of $\omega = 2\pi \times (400, 400, 76)$ Hz at a distance of 400 μm from the atom chip. Fig. 7.1 shows a characteristic set of images showing the onset of condensation.

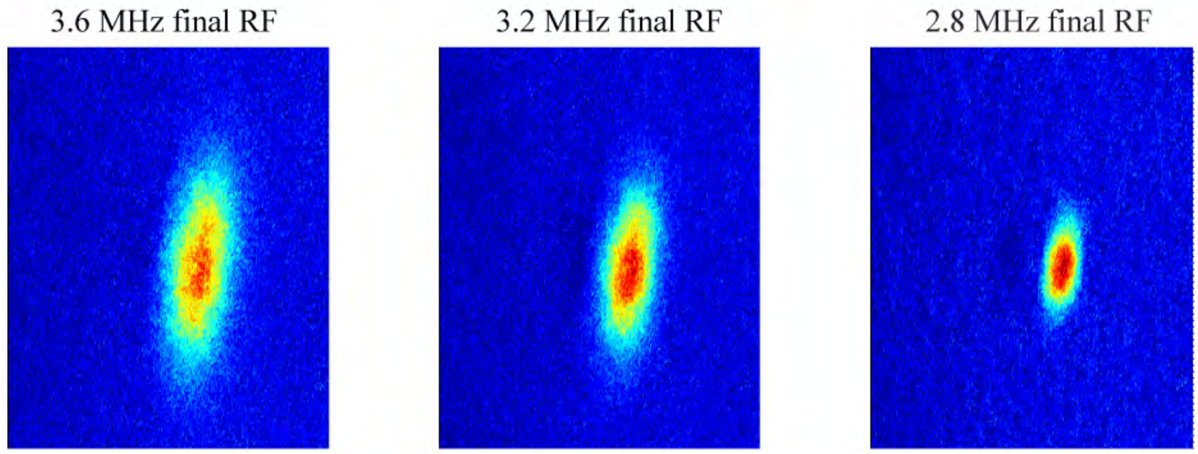

Figure 7.1: (Color). False color density profiles of atoms at the transition to BEC on the window chip.

7.2 Experiments with the version 1 window chip.

This section describes the experiments performed with the first generation window chip, shown in fig. 5.9. The chip was not designed with the optical projection system in mind, and as such was not optimal for through chip imaging experiments. The chip was valuable as a way of confirming that window chip technology would be good enough for BEC experiments, and for doing the firs through-chip imaging experiments.

7.2.1 Through chip imaging of a BEC

The condensed atoms are trapped directly beneath the wire in on the chip, and before the atoms are imaged they must be moved out from underneath the wire. As we discussed in chapter 4, this is simple to do in a two dimensional waveguide by applying a bias field perpendicular to the chip surface. However, this is not as straightforward with a dimple trap because the trap rotates about the two axes of the dimple at different rates, as shown by eq. 4.10. Numerical modeling of rotating the trap shows that an applied vertical bias will often drive the magnetic field through a zero point, which will both cause the trap to split and allow the atoms to fall out the bottom of the trap. As can be seen in fig. 7.2 (a) and (b), the trap clearly splits as it is moved towards a position where it could be imaged. By a stroke of luck the atom chip was accidentally connected to the wrong leg of the Z wire, making the Z trap slightly asymmetric. Because of this asymmetry when the trap was rotated to the other side by reversing the Z bias field the cloud moved into the imaging position cleanly without splitting. As was mentioned in chapter 5 the cloud must be decompressed substantially to position it below the window. The final imaging trap for the version 1 cell is located at a position 250 μm below the chip surface and offset from the center by approximately 200 μ. The imaging trap frequencies are approximately $\omega = 2\pi \times (500, 500, 100)Hz$. With a cloud of 15×10^3 atoms this corresponds to a BEC with Thomas-Fermi size of about $(2 \times 2 \times 10)\,\mu$m along the eigenaxes of the trap.

Once the atoms are positioned beneath the window the camera is triggered to collect light a few tens of microseconds before the probe light is pulsed across the cloud. A number of the photons scattered from the cloud will go into the microscope objective, which are imaged onto the detector. The first fluorescence image of a Bose-Einstein Condensate we obtained through an atom chip is shown in fig. 7.3. The image is taken after a 1ms free expansion of the cloud, and is an accumulation of four images taken under identical experimental preparations. After the accumulation was taken the image was been binned into 4x4 pixels blocks. Each condensate consists of 20×10^3 atoms.

A nice feature of this system is that it allows us to simultaneously image the cloud in two directions: with absorption imaging using the conventional system and the other with fluorescence imaging through the microscope. This provides information about the cloud that would not otherwise be available. As a simple example of this fig. 7.4 shows a sequence of images taken through the microscope with varying probe pulse lengths. The images show that the probe pulse applies a force on the atoms, and that as the pulse length is increased the atoms are pushed further and further from their initial positions. The absorption images taken with these pictures show no significant

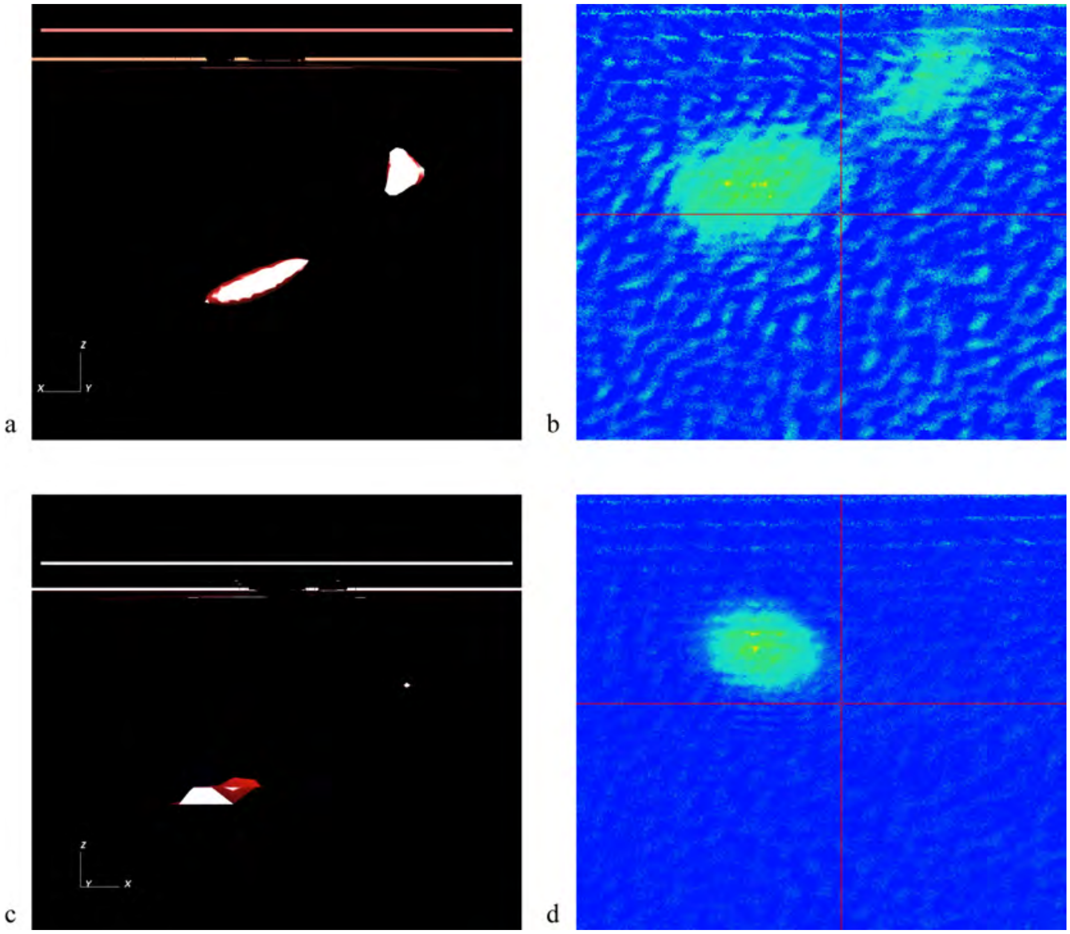

Figure 7.2: (Color). Splitting of the dimple trap due to trap rotation. (a) Numerical simulation of the trap behavior when a vertical bias field is applied. (b) Experimental image of atoms under the conditions calculated in (a). (c) numerical simulation of trap rotated in the opposite direction of (a) and (b) by reversing the bias field in the Z direction. Atoms do not split in this case because of the asymmetric way that the atom chip is connected. (d) Experimental image of atoms under the conditions calculated in (c). Numerical simulations were performed using LiveAtom magnetic field imaging software developed by Boulder Labs, Inc.

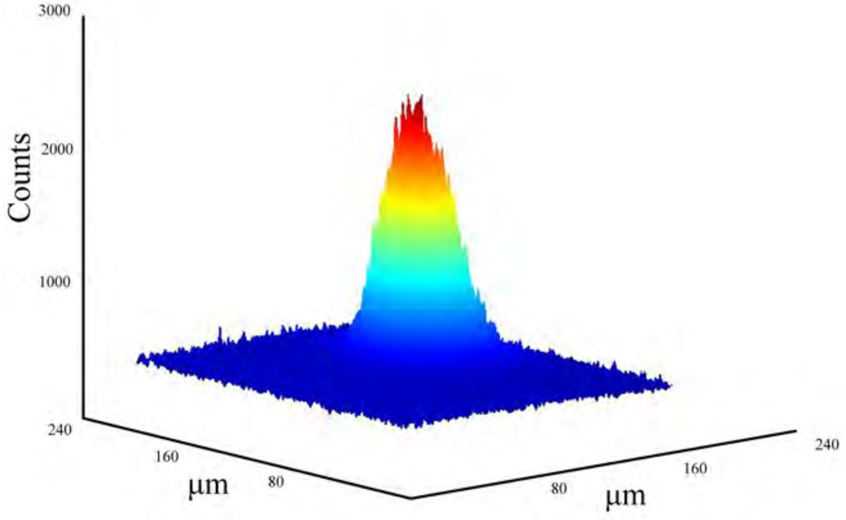

Figure 7.3: (Color). The first through-chip image of a BEC of 3×10^4 atoms.

difference in the clouds as the pulse length is changed.

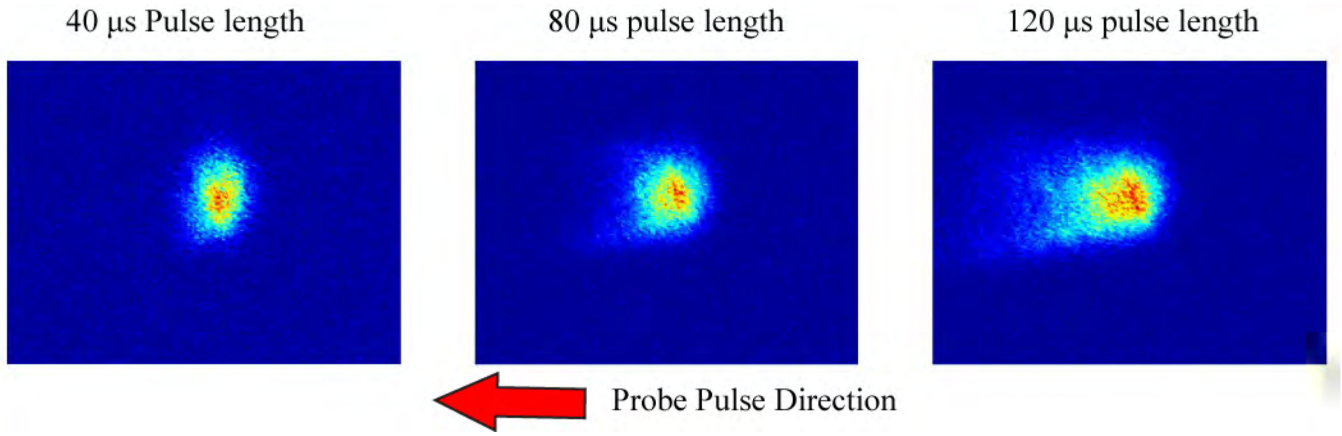

Figure 7.4: (Color). Flouresence images of BEC clouds showing movement and spreading of the cloud due to different length probe pulses.

7.2.2 Image characterization with interfering laser beams

The principle quantity of interest in the microscope system is the resolution, as this will ultimately dictate the limit of what potentials can be formed. To characterize the resolution of the imaging system the condensate is illuminated with two S-polarized probe beams. The beams are aligned parallel to the atom chip and separated in that plane by an angle θ. The configuration is shown in fig. 7.5.

The two probe beams will interfere, resulting in a fringe pattern in the overlap region with fringe spacing given by

$$\Delta x = \frac{\lambda}{2\sin(\theta/2)}. \tag{7.1}$$

By adjusting the interference angle one can easily set the fringe spacing to any width desired and generate fringe patterns as large as the cloud or as small as $\lambda/2$. The results of interfering the beams at $\theta = 9^\circ$ and $\theta = 18^\circ$, resulting in fringe spacings of 5 μm and 2.5μm respectively, are shown in fig. 7.6. Both images shown are taken by collecting 10 individual images of the cloud, performing a 2D Fourier transform on the image, binning the pixels in to 4x4 blocks, the summing

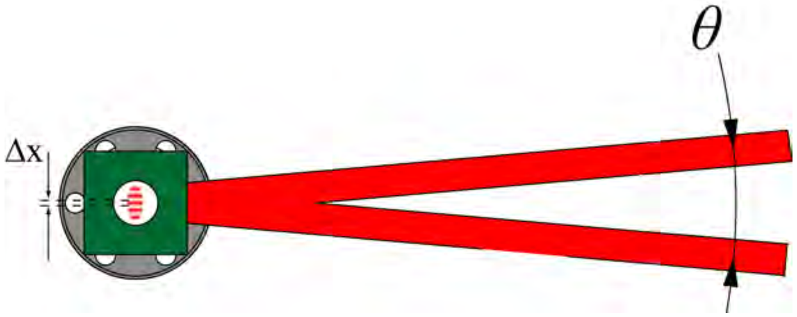

Figure 7.5: (Color). Configuration for interfering laser beams showing the view of the chamber and chip from the perspective of the microscope with atoms in center of the window.

the 10 Fourier transformed images and then reverse transforming the sum. This approach helps to filter out noise in the image and to mitigate the effects of any slight movement in the experiment that may cause the fringe pattern to shift between shots. The image processing comes at a sacrifice to resolution, since information is lost during the binning, and is only appropriate because the feature size we are trying to distinguish is much larger than the pixel magnification. The 5 μm fringes are reasonably evident in fig. 7.6(a), and can be seen very clearly in the fourier transform summation as two spikes above and below the central DC component in fig. 7.6(b). The 2.5 μm fringes in fig. 7.6(c) are not particularly clear, although they can be seen slightly in the Fourier transformed image, fig. 7.6. All of the Fourier transformed images shown are plotted on a logarithmic color scale.

The images shown in fig. 7.6 are taken with a Zeiss LD Plan-neofluar objective with a numerical aperture of 0.6, which should have a resolution limit of about 800 nm. The apparent loss of resolution can be mostly attributed to the large size of the cloud and the small depth of field of the objective. The depth of field of an imaging system is given by

$$d_{field} = \frac{\lambda}{\mathrm{NA}^2}. \tag{7.2}$$

For the 0.6 NA objective we expect a depth of field of 2.2 μm, which is far less than the size of the cloud measured with the absorption image. This problem is illustrated schematically in fig. 7.7.

There are several ways to address this issue. The Thomas-Fermi size of the cloud (equation

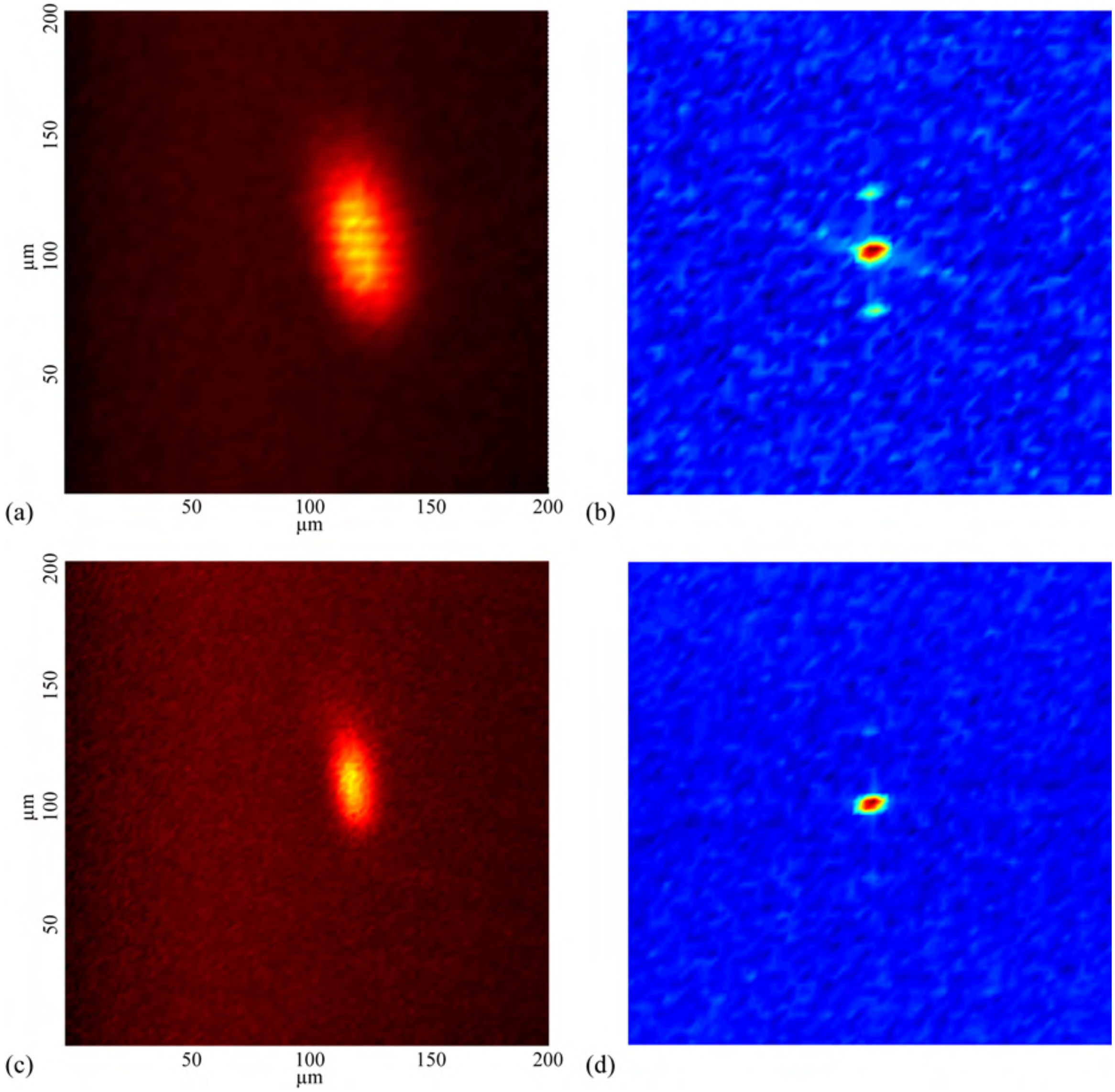

Figure 7.6: (Color). Resolution fringes from V1 window chip. (a) 5 μm fringes across a BEC cloud. (b) Fourier transform of (a) showing fringes as spikes above and below the DC component in the center of the image. (c) 2.5 μm fringes across a BEC of $\sim 10^4$ atoms. Fringes are not readily visible in the image. (d) Fourier transform if (c), showing very weak 2.5 μm spikes above and below the DC component. Both (a) and (c) are sets of 10 BEC images fourier transformed, summed and reverse transformed.

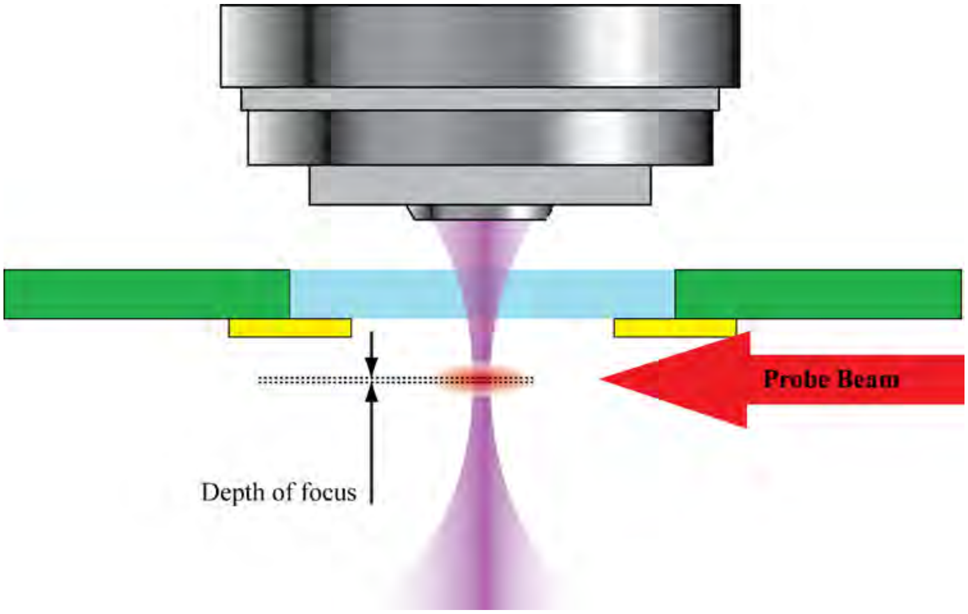

Figure 7.7: (Color). Depth of field resolution limits in the microscope system. The atom cloud, shown as red, is larger than the depth of field of the mircoscope objective but smaller than the probe beams. This results in photons scattering off objects that are out of focus with the imaging system, and reduced effective resolution.

2.23) may be reduced by decreasing the number of atoms in the trap or by tightening the trap in an anisotropic manner. Also, the images take here are taken after some free expansion of the cloud, which results in a larger object. For the purposes of both microscope characterization and for the atom transistor experiments it would be preferable to have the atoms in a cigar shaped trap. By the time we had gotten this far with the first generation chip the new cell was prepared for experiments, so it was a natural time to switch out the chambers. In most experimental setups this would be a daunting task that would be avoided while the working system was milked for every possible bit of data before breaking vacuum and replacing a central component. In our system the vacuum tube approach has proven to be an effective one, as it took less than 1 week to switch from the V1 chip cell to the V2 chip cell.

7.3 Experiments with the version 2 window chip

The BEC production procedure described earlier in this chapter is appropriate for one of our standard utility chips, such as the one shown in fig. 4.12(c) or for the V1 window chip in fig. 5.9. For the V2 window chip shown in figs. 5.16 and 5.17 a slightly different procedure is required. Because of the clear aperture at the center of the window and the symmetry of the design it is not possible to create a Z trap or a dimple trap. However, both H and T traps are possible with the available wire patterns. The atoms are loaded into the chip trap from the external quadrupole trap by simultaneously switching off the transfer coils and turning on a weak chip trap far from the surface, with 3.3 A in the main guide and 4 A through each of the H wires. The external bias fields are $(B_x, B_y, B_z) = (16, 0, 0)$ gauss, and the current directions are shown in fig. 7.8(a). The atoms are compressed into a T wire trap in two stages: First the chip currents and bias fields are ramped to $I_G = 2.2$vA, $I_H = 2.75$vA, $I_T = 0.3$vA and $(B_x, B_y, B_z) = (25, 37, 0)$ gauss over 20 ms. Second the trap is ramped to $I_G = 2.3$A, $I_H = 2.75$A, $I_T = 0.3$A and $(B_x, B_y, B_z) = (2.3, 39, 0)$ Gauss over 250 ms a trap with calculated trap frequencies of $\omega = 2\pi\times$(1.5 kHz, 1.5 kHz, 250 Hz) at a position of 150 μm from the chip surface. The atoms are evaporated in this trap to BEC over 1.7 seconds through a series of 4 linear RF frequency sweeps. Once BEC is produced the cloud is transferred into the trap directly below the center of the window by ramping off I_T and ramping up a current $I_{G\prime}$ in the other guide wire, as shown in fig. 7.8(c). The imaging trap parameters are $I_G = -I_{G\prime} = 2.75$ A, $I_H = 3.13$ A, $I_T = 0$ A and $(B_x, B_y, B_z) = (1, 0, 27)$ Gauss.

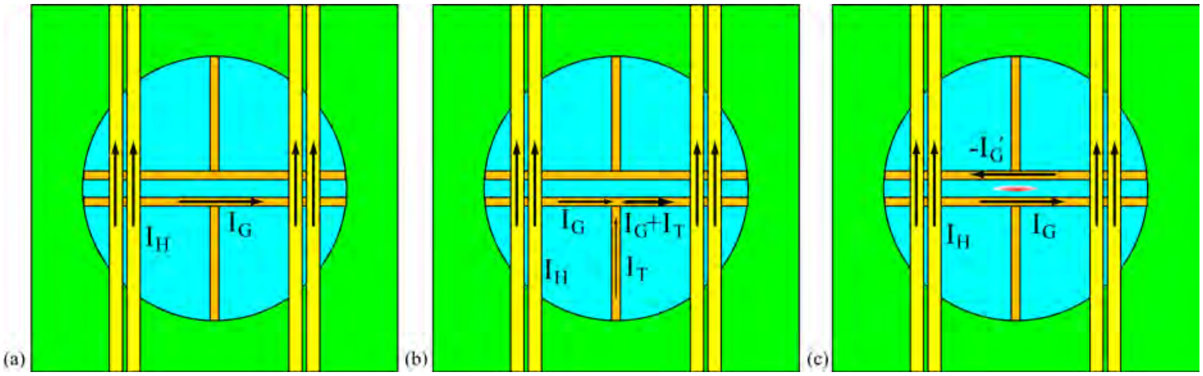

Figure 7.8: (Color). Current patterns used to trap atoms for the V2 window chip. (a) H configuration used to initially capture the atoms. (b) T-wire trap with H wires used for evaporative cooling. (c) Double guide wire configuration used for the imaging trap. T and Guide wires (orange) are on the vacuum side of the atom chip, while the H wires (yellow) are on the abient side.

As mentioned in chapter 5 the imaging trap can be moved arbitrarily close to the window surface by increasing the bias field in the $\hat{z}$ direction. We move the atoms to a position 100 μm from the window surface with trap frequencies of $\omega = 2\pi\times$(15 kHz, 1.5 kHz, 100 Hz). With 20×10^3 atoms in the condensate this trap results in a cloud with a Thomas-Fermi size of $1 \times 1 \times 15$ μm, which is ideal for the planned transistor experiments.

Using this trap we repeated the resolution experiments described in the previous section. In this configuration it is possible to image the atoms in-trap, which reduces the overall size of the cloud dramatically. Because the in-trap cloud is quite optically thick it is helpful to detune the probe laser from the atomic resonance. While this decreases the scattering rate and subsequently decreases the overall signal it also allows the probe light to access a larger fraction of the atoms in the cloud, and decrease the amount that the probe beam moves the atoms during the imaging pulse. We obtained the best results at a probe laser detuning of 3-4Γ red of the $|F = 2 \rightarrow F = 3\rangle$ cycling transition. Fig. 7.9(a) shows the results from interfering the probe beams at $\theta = 9°$ to generate 5 μm fringes. The image in this case is a direct summation of five images taken after no free expansion. It is interesting to note the slight angular tilt of the fringes relative to the cloud, which is very obvious in the fourier transform image, fig. 7.9(b). This tilt is due to the fact that one of the probe beams is square to the cell while the other is tilted 9° away. The results of probing the cloud with an interference angle of $\theta = 18^\circ$ and the resulting Fourier transform are shown in fig. 7.9(c) and (d). Here we have demonstrated a dramatic improvement with 2.5 μm fringes.

Although we believe that we are still far above the resolution limits of the imaging system we have not yet demonstrated small features with this imaging system. Because of the obstruction of the magnetic coils it is not possible to interfere the laser beams at an angle that would generate fringes between 1 μm and 2.5 μm, and we have not yet been able to resolve features as small as 1 μm.

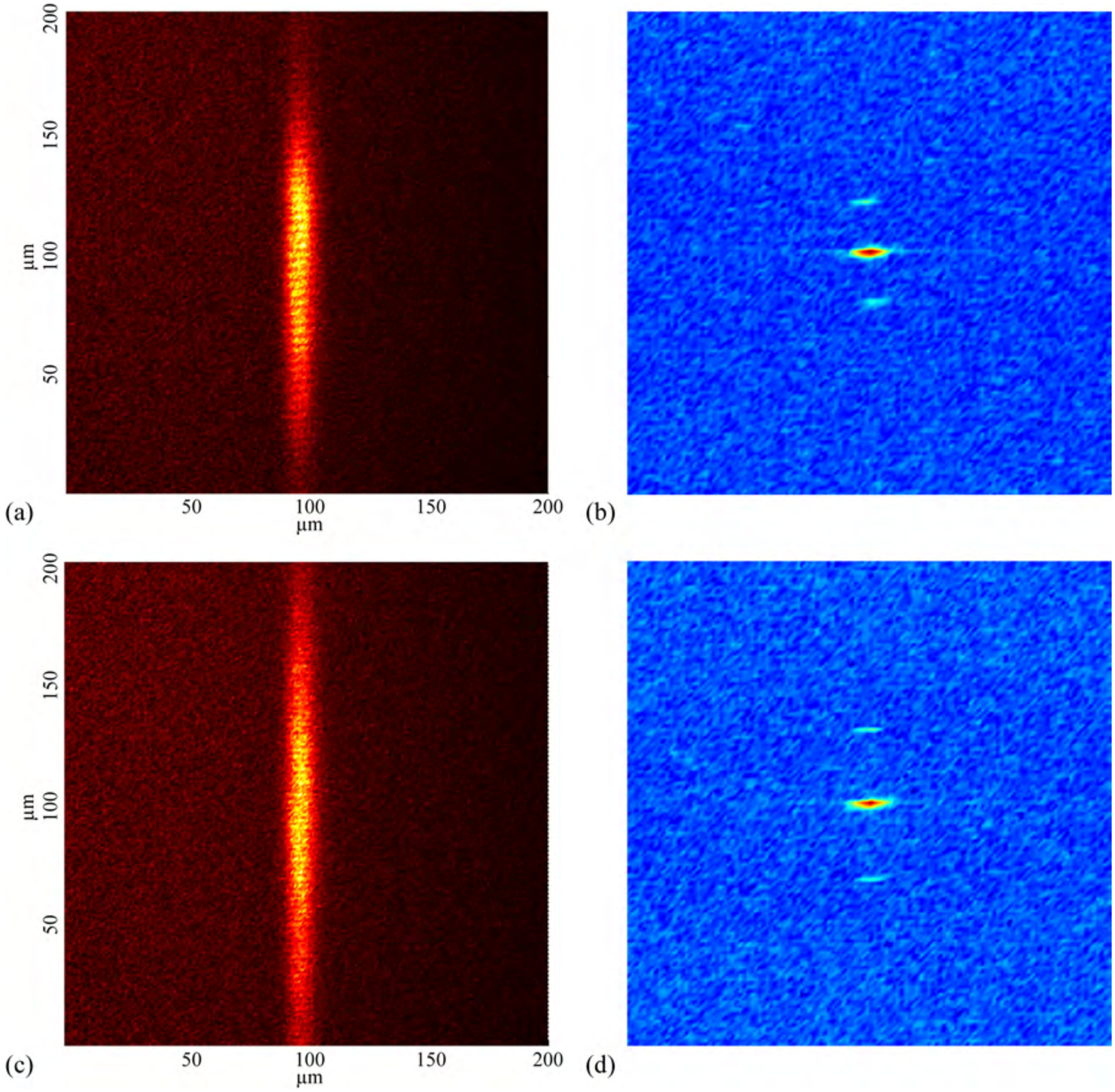

Figure 7.9: (Color). Resolution fringes from V2 window chip. (a) 5 μm fringes across a BEC cloud. (b) Fourier transform of (a) showing fringes as spikes above and below the DC component in the center of the image. (c) 2.5 μm fringes across a BEC of $\sim 10^4$ atoms. Fringes are significantly more visible that those of the same scale demonstrated with the V1 chip. (d) Fourier transform if (c), showing very weak 2.5 μm spikes above and below the DC component. Both (a) and (c) are direct summations of 5 BEC images.

Chapter 8

Outlook

This thesis has detailed the instrumentation development in our lab over the past 7 years. Substantial progress has been made in the miniaturization of both the vacuum chambers and the associated equipment needed to produce Bose-Einstein Condensates. The atom chips have improved dramatically since the beginning of this work, and are now a robust, reliable technology that can serve as the backbone for future applications of BEC. In particular the development of window chip technology marks a major technical accomplishment. Atom chips and the double MOT cell are currently being developed for commercial applications by ColdQuanta, Inc. in Boulder, CO. The channel cell technology is being re-evaluated for use in an information advanced research projects agency (IARPA) program where the techniques we have developed will help to enable a 64 bit quantum computer of neutral atoms. The portable BEC system is still being used in our lab for further atom chip experiments.

The atomtronics experiment is well on its way towards demonstrating an atom transistor. The next step in the development of this apparatus will be to show optical manipulation of the atoms through the microscope system. We are currently building up a laser system using a super luminescent laser diode centered at 760nm for preliminary trapping experiments. Once the projection system is in place it will be possible to start looking for tunneling events in the cloud and to study tunneling in two well systems in a chip trap. Following that we will begin using a spatial light modulator to generate time varying potentials and to generate a transistor potential. Additionally this high resolution imaging and projection will potentially be very versatile, and allow direct experimental study of arbitrary one-dimensional atomic physics problems.

Bibliography

[1] M. H. Anderson, J. R. Ensher, M. R. Matthews, C. E. Wieman, and E. A. Cornell. Observation of bose-einstein condensation in a dilute atomic vapor. Science, 269:198, 1995.

[2] K. B. Davis, M. O. Mewes, M. R. Andrews, N. J. van Druten, D. S. Durfee, D. M. Kurn, and W. Ketterle. Bose-einstein condensation in a gas of sodium atoms. Phys. Rev. Lett., 75: 3969, 1995.

[3] C. C. Bradley, C. A. Sackett, J. J. Tollett, and R. G. Hulet. Evidence of bose-einstein condensation in an atomic gas with attractive interactions. Phys. Rev. Lett., 75:1687, 1995.

[4] M. Greiner, O. Mandel, T. Esslinger, T.W. Hänsch, and I. Bloch. Quantum phase transition from a superfluid to a mott insulator in a gas of ultracold atoms. Nature, 415:39, 2002.

[5] L. Isenhower, E. Urban, X. L. Zhang, A. T. Gill, T. Henage, T. A. Johnson, T. G. Walker, and M. Saffman. Demonstration of a neutral atom controlled-not quantum gate. Phys. Rev. Lett., 104:010503, 2010.

[6] K.D. Nelson, X. Li, and D.S. Weiss. Imaging single atoms in a three-dimensional array. Nature Physics, 3:556, 2007.

[7] J. V. Porto, S. Rolston, B. Laburthe Tolra, C. J. Williams, and W. D. Phillips. Quantum information with neutral atoms as qubits. Phil. Trans. of the Royal Society A, 361:1417, 2003.

[8] T. Rosenband, D. B. Hume, P. O. Schmidt, C. W. Chou, A. Brusch, L. Lorini, W. H. Oskay, R. E. Drullinger, T. M. Fortier, J. E. Stalnaker, S. A. Diddams, W. C. Swann, N. R. Newbury, W. M. Itano, D. J. Wineland, and J. C. Bergquist. Frequency ratio of al$^+$ and hg$^+$ single-ion optical clocks; metrology at the 17th decimal place. Science, 319:1808, 2008.

[9] A. D. Ludlow, T. Zelevinsky, G. K. Campbell, S. Blatt, M. M. Boyd, M. H. G. de Miranda, M. J. Martin, J. W. Thomsen, S. M. Foreman, Jun Ye, T. M. Fortier, J. E. Stalnaker, S. A. Diddams, Y. Le Coq, Z. W. Barber, N. Poli, N. D. Lemke, K. M. Beck, and C. W. Oates. Sr lattice clock at 1×10^{16} fractional uncertainty by remote optical evaluation with a ca clock. Science, 319:1805, 2008.

[10] D. Farkas, A. Zozulya, and D. Anderson. A compact microchip atomic clock based on all-optical interrogation of ultra-cold trapped rb atoms. Appl. Phys. B, 101:705, 2010.

[11] M. Vengalattore, J. M. Higbie, S. R. Leslie, J. Guzman, L. E. Sadler, and D. M. Stamper-Kurn. High-resolution magnetometry with a spinor bose-einstein condensate. Phys. Rev. Lett., 98:200801, 2007.

[12] M. L. Terraciano, M. Bashkansky, and F.K. Fatemi. A single-shot imaging magnetometer using cold atoms. Opt. Express, 16:13062, 2008.

[13] H. Lefèvre. The Fiber-Optic Gyroscope. Artech House, Boston, 1993.

[14] K. Takase. Precision Rotation Rate Measurements with a Mobile Atom Interferometer. PhD thesis, 2008.

[15] X. Wu. Gravity Gradient Survey with a Mobile Atom Interferometer. PhD thesis, 2009.

[16] T. van Zoest, N. Gaaloul, Y. Singh, H. Ahlers, W. Herr, S. T. Seidel, W. Ertmer, E. Rasel, M. Eckart, E. Kajari, S. Arnold, G. Nandi, W. P. Schleich, R. Walser, A. Vogel, K. Sengstock, K. Bongs, W. Lewoczko-Adamczyk, M. Schiemangk, T. Schuldt, A. Peters, T. Knemann, H. Mntinga, C. Lmmerzahl, H. Dittus, T. Steinmetz, T. W. Hänsch, and J. Reichel. Bose-einstein condensation in microgravity. Science, 328:1540, 2010.

[17] W. Hänsel, P. Hommelhoff, T. W. Hänsch, and J. Reichel. Bose-einstein condensation on a microelectronic chip. Nature, 413:498, 2001.

[18] J. Reichel. Microchip traps and bose einstein condensation. Appl.Phys. B, 74:469, 2002.

[19] S. Du, M.B. Squires, Y. Imai, L. Czaia, R. A. Saravanan, V.M. Bright, J. Reichel, T. W. Hänsch, and D.Z. Anderson. Atom-chip bose-einstein condensation in a portable vacuum cell. Phys. Rev. A, 70:053606, 2004.

[20] S. Aubin, M. H. T. Extavour, S. Myrskog, L. J. LeBlanc, J. Estve, S. Singh, P. Scrutton, D. McKay, R. McKenzie, I. D. Leroux, A. Stummer, and J. H. Thywissen. Trapping fermionic ^{40}k and bosonic ^{87}rb on a chip. J. of Low Temp. Phys., 140:377, 2005.

[21] J. Fortágh and C. Zimmermann. Magnetic microtraps for ultracold atoms. Rev. of Mod. Phys., 79:235, 2007.

[22] M. Horikoshi and K. Nakagawa. Atom chip based fast production of boseeinstein condensate. Appl. Phys. B, 82:363, 2006.

[23] M.B. Squires. High repetition rate Bose-Einstein condensate production in a compact, transportable vacuum system. PhD thesis, 2008.

[24] S.R. Segal. Progress Towards an Ultracold Atomic Sagnac Gyroscope. PhD thesis, 2010.

[25] B. T. Seaman, Kr, auml, M. mer, D. Z. Anderson, and M. J. Holland. Atomtronics: Ultracold-atom analogs of electronic devices. Phys. Rev. A, 75:023615, 2007.

[26] R. A. Pepino, J. Cooper, D. Z. Anderson, and M. J. Holland. Atomtronic circuits of diodes and transistors. Phys. Rev. Lett., 103:140405, 2009.

[27] A. Micheli, A. J. Daley, D. Jaksch, and P. Zoller. Single atom transistor in a 1d optical lattice. Phys. Rev. Lett., 93:140408, 2004.

[28] J. Stickney, D. Anderson, and A. Zozulya. Transistorlike behavior of a bose-einstein condensate in a triple-well potential. Phys. Rev. A, 75:013608, 2007.

[29] K. J. Hughes, J. H. T. Burke, and C. A. Sackett. Suspension of atoms using optical pulses, and application to gravimetry. Phys. Rev. Lett., 102:150403, 2009.

[30] T. M. Roach, H. Abele, M. G. Boshier, H. L. Grossman, K. P. Zetie, and E. A. Hinds. Realization of a magnetic mirror for cold atoms. Phys. Rev. Lett., 75:629, 1995.

[31] B. Lev, Y. Lassailly, C. Lee, A. Scherer, and H. Mabuchi. Atom mirror etched from a hard drive. Appl. Phys. Lett., 83:395, 2003.

[32] D.W. Keith, C.R. Ekstrom, Q.A. Turchette, and D.E. Pritchard. An interferometer for atoms. Phys. Rev. Lett., 66:2693, 1991.

[33] S. Wu, Y.J. Wang, Q. Diot, and M. Prentiss. Splitting matter waves using an optimized standing-wave light-pulse sequence. Phys. Rev. A, 71:043602, 2005.

[34] D. Müller, E.A. Cornell, M. Prevedelli, P.D.D. Schwindt, A. Zozulya, and D.Z. Anderson. Waveguide atom beam splitter for laser-cooled neutral atoms. Opt. Lett., 25:1382–1384, 2000.

[35] D. Cassettari, B. Hessmo, R. Folman, T. Maier, and J. Schmiedmayer. Beam splitter for guided atoms. Phys. Rev. Lett., 85:5483, 2000.

[36] S. Hofferberth, I. Lesanovsky, B. Fischer, J. Verdu, and J. Schmiedmayer. Radio frequency dressed state potentials for neutral atoms. Nature Phys., 2:710, 2006.

[37] H. J. Lewandowski, D. M. Harber, D. L. Whitaker, and E. A. Cornell. Simplified system for creating a boseeinstein condensate. J. of Low Temp. Phys., 132:309, 2003.

[38] E.W. Streed, A.P. Chikkatur, T.L. Gustavson, M. Boyd, Y. Torii, D. Schneble, G.K. Campbell, D.E. Pritchard, and W. Ketterle. Large atom number bose-einstein condensate machines. Rev. of Sci. Inst., 77:023106, 2006.

[39] W. Ketterle, D.S. Durfee, and D.M. Stamper-Kurn. Making, probing and understanding Bose-Einstein condensates, pages 67–176. IOS Press, Amsterdam, 1999.

[40] C. J. Pethick and H Smith. Bose-Einstein Condensation in Dilute Gases. Cambridge University Press, 2002.

[41] M. D. Barrett, J. A. Sauer, and M. S. Chapman. All-optical formation of an atomic bose-einstein condensate. Phys. Rev. Lett., 87:010404, 2001.

[42] S. Inouye, M. R. Andrews, J. Stenger, H. J. Miesner, D. M. Stamper-Kurn, and W. Ketterle. Observation of feshbach resonances in a bose-einstein condensate. Nature, 392:151, 1998.

[43] R. Grimm, M. Weidemüller, and Y.B. Ovchinnikov. Optical Dipole Traps for Neutral Atoms, volume 42, page 95. Academic Press, 2000.

[44] F.K. Fatemi and M. Bashkansky. Generation of hollow beams by using a binary spatial light modulator. Opt. Lett., 31:864, 2006.

[45] L. Isenhower, W. Williams, A. Dally, and M. Saffman. Atom trapping in an interferometrically generated bottle beam trap. Opt. Lett., 34:1159, 2009.

[46] J. Gillen, W. Bakr, A. Peng, P. Unterwaditzer, S. Flling, and M. Greiner. Two-dimensional quantum gas in a hybrid surface trap. Phys. Rev. A, 80:021602, 2009.

[47] L. Pitaevskii and S. Stringari. Bose-Einstein Condensation. Oxford Science Publications, 2003.

[48] G. Baym and C. J. Pethick. Ground-state properties of magnetically trapped bose-condensed rubidium gas. Phys. Rev. Lett., 76:6, 1996.

[49] M. Razavy. Quantum Theory of Tunneling. World Scientific, New Jersey, 2003.

[50] G. J. Milburn, J. Corney, E. M. Wright, and D. F. Walls. Quantum dynamics of an atomic bose-einstein condensate in a double-well potential. Phys. Rev. A, 55:4318, 1997.

[51] S. Fantoni S. Raghavan, A. Smerzi and S. R. Shenoy. Coherent oscillations between two weakly coupled bose-einstein condensates: Josephson effects, π oscillations, and macroscopic quantum self-trapping. Phys. Rev. A, 59:620, 1999.

[52] Y. Hao, J. Q. Liang, and Y. Zhang. Numerical simulation on tunnel splitting of bose-einstein condensate in multi-well potentials. Euro. Phys. J. D, 36:33, 2005.

[53] T. G. Tiecke, M. Kemmann, C Buggle, I Shvarchuck, W Klitzing, and J.T.M Walraven. Boseeinstein condensation in a magnetic double-well potential. J. of Optics B, 5:S119, 2003.

[54] Y. Shin, M. Saba, A. Schirotzek, T. A. Pasquini, A. E. Leanhardt, D. E. Pritchard, and W. Ketterle. Distillation of bose-einstein condensates in a double-well potential. Phys. Rev. Lett., 92:150401, 2004.

[55] T. Schumm, S. Hofferberth, L. M. Andersson, S. Wildermuth, S. Groth, I. Bar-Joseph, J. Schmiedmayer, and P. Kruger. Matter-wave interferometry in a double well on an atom chip. Nature Phys., 1:57, 2005.

[56] R. Gati and M. K. Oberthaler. A bosonic josephson junction. J. of Phys. B, 40:R61, 2007.

[57] E. Kierig, U. Schnorrberger, A. Schietinger, J. Tomkovic, and M. Oberthaler. Single-particle tunneling in strongly driven double-well potentials. Phys. Rev. Lett., 100:190405, 2008.

[58] M. Albiez. Observation of nonlinear tunneling of a BEC in a single Josephenson junction. PhD thesis, 2005.

[59] M. Albiez, R. Gati, J. Folling, S. Hunsmann, M. Cristiani, and M.K. Oberthaler. Realization of a single josephson junction for bose-einstein condensates. App. Phys. B, 82:207, 2006.

[60] B. P. Anderson and M. A. Kasevich. Loading a vapor-cell magneto-optic trap using light-induced atom desorption. Phys. Rev. A, 63:023404, 2001.

[61] T.A. Delchar. Vacuum Physics and Techniques. Chapman & Hall, New York, 1993.

[62] S. Du. Atom-Chip Bose-Einstein Condensation in a Porable Vacuum Cell. PhD thesis, 2005.

[63] G.D. Wallis and D.I. Pomerantz. Field assisted glass-metal sealing. J. Appl. Phys., 40:3946, 1969.

[64] K. Dieckmann, R. J. C. Spreeuw, M. Weidemuller, and J. T. M. Walraven. Two-dimensional magneto-optical trap as a source of slow atoms. Physical Review A, 58:3891, 1998.

[65] Z. T. Lu, K. L. Corwin, M. J. Renn, M. H. Anderson, E. A. Cornell, and C. E. Wieman. Low-velocity intense source of atoms from a magneto-optical trap. Phys. Rev. Lett., 77:3331, 1996.

[66] J.M. Kohel, J. Ramirez-Serrano, R.J. Thompson, L. Maleki, J.L. Bliss, and K.G. Libbrecht. Generation of an intense cold-atom beam from a pyramidal magneto-optical trap: experiment and simulation. J. Opt. Soc. Am. B, 20:1161, 2003.

[67] J. Schoser, R. Batar, R. Low, V. Schweikhard, A. Grabowski, Yu B. Ovchinnikov, and T. Pfau. Intense source of cold rb atoms from a pure two-dimensional magneto-optical trap. Phys. Rev. A, 66:023410, 2002.

[68] R. J. Elsey. Outgassing of vacuum materials-ii. Vacuum, 25:347, 1975.

[69] N. F. Raley, J. C. Davidson, and J. W. Balch. Examination of glass-silicon and glass-glass bonding techniques for microfluidic systems. Proc. SPIE 2639, 40:doi:10.1117/12.221298, 1995.

[70] C. G. J. Schabmueller and et al. Design and fabrication of a microfluidic circuitboard. Journal of Micromechanics and Microengineering, 9:176, 1999.

[71] D.M. Farkas, K.M. Hudek, E.A. Salim, S.R. Segal, M.B. Squires, and Dana Z. Anderson. A compact, transportable, microchip-based system for high repetition rate production of bose–einstein condensates. Appl. Phys. Lett., 96:093102–3, 2010.

[72] J. Schmiedmayer. A wire trap for neutral atoms. Appl. Phys. B, 60:169, 1995.

[73] J. Fortágh, A. Grossmann, C. Zimmermann, and T. W. Hänsch. Miniaturized wire trap for neutral atoms. Phys. Rev. Lett., 81:5310, 1998.

[74] H. Ott, J. Fortagh, G. Schlotterbeck, A. Grossmann, and C. Zimmermann. Bose-einstein condensation in a surface microtrap. Phys. Rev. Lett., 87:230401, 2001.

[75] H. Chuang, E.A. Salim, V. Vuletic, D.Z. Anderson, and V.M. Bright. Multi-layer atom chips for atom tunneling experiments near the chip surface. Sensors and Actuators A: Physical, In Press, Corrected Proof, 2010.

[76] Y. Japha, O. Entin-Wohlman, T. David, R. Salem, S. Aigner, J. Schmiedmayer, and R. Folman. Model for organized current patterns in disordered conductors. Phys. Rev. B, 77: 201407, 2008.

[77] J. Reichel, W Hänsel, and T. W. Hänsch. Atomic micromanipulation with magnetic surface traps. Phys. Rev. Lett., 83:3398, 1999.

[78] S. Groth, P. Kruger, S. Wildermuth, R. Folman, T. Fernholz, J. Schmiedmayer, D. Mahalu, and I. Bar-Joseph. Atom chips: Fabrication and thermal properties. Appl. Phys. Lett., 85: 2980, 2004.

[79] M. Trinker, S. Groth, S. Haslinger, S. Manz, T. Betz, S. Schneider, I. Bar-Joseph, T. Schumm, and J. Schmiedmayer. Multilayer atom chips for versatile atom micromanipulation. Appl.Phys. Lett., 92:254102, 2008.

[80] R.J. Sewell, J Dingjan, F Baumgrtner, I Llorente-Garca, S Eriksson, E.A. Hinds, G Lewis, P Srinivasan, Z Moktadir, C.O. Gollasch, and M Kraft. Atom chip for bec interferometry. J. of Phys. B, 43:051003, 2010.

[81] N.T. Nguyen, E. Boellaard, N.P. Pham, V.G. Kutchoukov, G. Craciun, and P.M. Sarro. Through-wafer copper electroplating for three-dimensional interconnects. J. of Micromech. and Microeng., 12:395, 2002.

[82] H.W. van Zeijl, D. Liu, and P.M. Sarro. Through silicon interconnect using grayscale lithography for mems applications. Procedia Chemistry, 1:1543, 2009.

[83] H. Chuang, D.Z. Anderson, and V.M. Bright. The fabrication of through-wafer interconnects in silicon substrates for ultra-high-vacuum atom-optics cells. J. of Micromech. and Microeng., 18:045003, 2008.

[84] Z. Wang, L. Wang, N.T. Nguyen, W.A.H. Wien, H. Schellevis, and P.M. Sarro. Silicon micromachining of high aspect ratio, high density through-wafer electrical interconnects for 3d multichip packaging. IEEE Transactions on Advanced Packaging, 29:615, 2006.

[85] G.B. Jo, Y. Shin, S. Will, T.A. Pasquini, M. Saba, W. Ketterle, D.E. Pritchard, M. Vengalattore, and M. Prentiss. Long phase coherence time and number squeezing of two bose-einstein condensates on an atom chip. Phys. Rev. Lett., 98:030407, 2007.

[86] H.B.G. Casimir and D. Polder. The influence of retardation on the london-van der waals forces. Physical Review, 73:360, 1948.

[87] C. I. Sukenik, M. G. Boshier, D. Cho, V. Sandoghdar, and E. A. Hinds. Measurement of the casimir-polder force. Phys. Rev. Lett., 70:560, 1993.

[88] D. M. Harber, J. M. Obrecht, J. M. McGuirk, and E. A. Cornell. Measurement of the casimir-polder force through center-of-mass oscillations of a bose-einstein condensate. Phys. Rev. A, 72:033610, 2005.

[89] Y. Lin, I. Teper, C. Chin, and V. Vuleti. Impact of the casimir-polder potential and johnson noise on bose-einstein condensate stability near surfaces. Phys. Rev. Lett., 92:050404, 2004.

[90] Z. Yan, A. Dalgarno, and J.F. Babb. Long range interactions of lithium atoms. Phys. Rev. A, 55, 1997.

[91] R. Salem and et al. Nanowire atomchip traps for sub-micron atomsurface distances. New Journal of Physics, 12:023039, 2010.

[92] A. Günther, M. Kemmler, S. Kraft, C. J. Vale, C. Zimmermann, and J. Fortágh. Combined chips for atom optics. Phys. Rev. A, 71:063619, 2005.

[93] Y.J. Wang, D.Z. Anderson, V.M. Bright, E.A. Cornell, Q. Diot, T. Kishimoto, M. Prentiss, R. A. Saravanan, S.R. Segal, and S. Wu. Atom michelson interferometer on a chip using a bose-einstein condensate. Phys. Rev. Lett., 94:090405, 2005.

[94] W.S. Bakr, J.I. Gillen, A. Peng, S. Folling, and M. Greiner. A quantum gas microscope for detecting single atoms in a hubbard-regime optical lattice. Nature, 462:74, 2009.

[95] J.F. Sherson, C. Weitenberg, M. Endres, M. Cheneau, I. Bloch, and S. Kuhr. Single-atom-resolved fluorescence imaging of an atomic mott insulator. Nature, 467:68, 2010.

[96] Y.A. Chen, S.D. Huber, S. Trotzky, I. Bloch, and E. Altman. Many-body landau-zener dynamics in coupled one-dimensional bose liquids. Nat Phys, 7:61, 2011.

[97] D. McGloin, G. Spalding, H. Melville, W. Sibbett, and K. Dholakia. Applications of spatial light modulators in atom optics. Opt. Express, 11:158, 2003.

[98] L. Brandt, C. Muldoon, T. Thiele, J. Dong, E. Brainis, and A. Kuhn. Spatial light modulators for the manipulation of individual atoms. Appl. Phys. B, page in press, 2010.

[99] E. Hecht. Optics. Addison-Wesley, 2002.

[100] S. Papp. Experiments with a two-species Bose-Einstein condensate utilizing widely tunable interparticle interactions. PhD thesis, 2007.

[101] M. Greiner, I. Bloch, T. W. Hänsch, and T. Esslinger. Magnetic transport of trapped cold atoms over a large distance. Phys. Rev. A, 63:1050–2947, 2001.

[102] P.T. Vianco. ASM Handbook, volume 6. 1993.

[103] R. Bucker, A. Perrin, S. Manz, T. Betz, C. Koller, T. Plisson, J. Rottmann, T. Schumm, and J. Schmiedmayer. Single-particle-sensitive imaging of freely propagating ultracold atoms. New Journal of Physics, 11, 2009.

[104] W. Petrich, M.H. Anderson, J.R. Ensher, and E.A. Cornell. Behavior of atoms in a compressed magneto-optical trap. J. Opt. Soc. Am. B, 11:1332, 1994.